Pattern Formation and Organization of Epithelial Tissues

by

Jeremy Hadidjojo

A dissertation submitted in partial fulfillment
of the requirements for the degree of
Doctor of Philosophy
(Physics)
in the University of Michigan
2017

Doctoral Committee:

Associate Professor David K. Lubensky, Chair
Professor Pamela A. Raymond
Assistant Professor Kevin Wood
Professor Michal Zochowski

hjeremy@umich.edu

ORCID iD: 0000-0002-9161-9727

2017

TABLE OF CONTENTS

List of Figures . . . . . **iv**

List of Tables . . . . . **vi**

List of Appendices . . . . . **vii**

Abstract . . . . . **viii**

Chapter

1 Introduction **1**

2 Spontaneous Chiral Symmetry Breaking in Planar Polarized Epithelia **7**

2.1 Abstract 7
2.2 Introduction 8
2.3 General symmetry arguments 10
2.4 Mean-field PCP model 12
2.5 Direct $\mathbf{I} \rightarrow \mathbf{N}^*$ transitions 14
2.6 Discussion 15

3 Quantitative Analysis of Fluorescence Microscopy Images **18**

3.1 Introduction: Cone Mosaic in Zebrafish Retina 19
3.2 Analysis of *tbx2b* Mutant Column Fragments 22
3.2.1 Thresholding-based cell segmentation 24
3.2.2 Cell classification based on marker intensity 24
3.2.3 Two-threshold adjacency determination 25
3.2.4 Results: Most *tbx2b* mutant cones are 2-fold coordinated 27
3.3 Selective Projection of z-stack images 30
3.3.1 Core Algorithms 31
3.3.2 Misc: Pre- and Post-Processing Routines 34
3.3.3 Conclusion 37
3.4 Ridge Analysis of Müller Glia Bands 38
3.4.1 Steerable ridge filter 40
3.4.2 Directional filtering of ridge lines using Fast Fourier Transform . 41
3.4.3 Results 42
3.5 Analysis of Laser Ablation Experiment on Zebrafish Retina 44
3.5.1 Analysis Method 45
3.5.2 Results 50

4 Correlation Analysis of Morphogenetic Noise 56
4.1 Introduction 57
4.2 Model of left-right velocity correlation 60
4.3 Analysis of full-notum movie 62
4.4 Analysis of half-notum movies 64
4.4.1 No data collapse on hemi-notum average velocity 65
4.4.2 Auto-correlation with different window sizes 66
4.4.3 Spatial map shows regions of positive and negative autocorrelations 67
4.5 Conclusion 67
Appendices 70
Bibliography 160

LIST OF FIGURES

2.1 Chiral morphogenesis driven by spontaneous left-right symmetry breaking . . 8
2.2 Cartoons of rreducible representations and mean-field PCP model 10
2.3 Phase diagram of mean-field PCP model on regular hexagon 14
2.4 Phase diagram of mean-field PCP model on stretched hexagon 15
2.5 Phase diagram of mean-field PCP model on regular hexagon with slight asymmetry in A & B interactions 17

3.1 Anatomy of zebrafish retina mosaic 20
3.2 Loss of cone photoreceptor columnar order in tbx2b mutant retina 23
3.3 Analysis of *tbx2b* mutant column fragments 26
3.4 Infrequent 3-fold coordination of *tbx2b* mutant retina cone photoreceptors suggests strongly directional interaction 28
3.5 Selective Projection of z-stack images: example and methods 33
3.6 Selective Projection of z-stack images: intensity profiles 35
3.7 Detection of intercolumn thick Müller ridges. 39
3.8 Ridge detection of Müller glial bands in mature retina 41
3.9 Ridge detection of Müller glial bands at the margin 43
3.10 Change in tilt angle of the OLM with respect to the imaging focal plane 47
3.11 Laser ablation of Müller glial processes 51

4.1 Fly dorsal notum 58
4.2 Scaling of noise in full-notum 63
4.3 Rate of rotation of left and right halves of full notum show that they are in synchrony 64
4.4 Variance of velocity of hemi-notum does not show nice data collapse 65
4.5 Auto-correlation of hemi-notum movies 66
4.6 Spatial map of auto-correlation at 5 minutes time-lag 68
4.7 Spatial map of auto-correlation at 20 minutes time-lag 68

B.1 Comparison between traditional and window-deforming PIV 97
B.2 Correlated velocities remain after archetype subtraction 99

C.1 Emergence of the photoreceptor mosaic in rapidly growing juvenile zebrafish . 146
C.2 Spatial arrangement of cones is already patterned in the differentiating precolumn zone 147
C.3 Spatial patterning of cones precedes planar polarized Crumbs localization . . . 148

C.4 Rod photoreceptors are incorporated into the cone mosaic as it emerges from the proliferating zone . . . 149
C.5 Parallel bands of Müller glial scaffolding appear simultaneously with differentiating cones . . . 150
C.6 N-cadherin is associated with actomyosin mechanical forces in differentiating cones in the pre-column zone and with Müller glia inter-column bands in the mature mosaic . . . 151
C.7 Müller glia mediate anisotropic mechanical forces in the retinal epithelium . . . 152
C.8 A model for how the multiplex photoreceptor mosaic is patterned by anisotropic tension, glial scaffolding, and planar polarized cell adhesion . . . 153
C.9 Figure 1 supplemental figure . . . 154
C.10 Figure 2 supplemental figure . . . 155
C.11 Figure 4 supplemental figure 1 . . . 156
C.12 Figure 4 supplemental figure 2 . . . 157
C.13 Figure 5 supplemental figure . . . 158
C.14 Figure 7 supplemental figure . . . 159

LIST OF TABLES

3.1 Coordination number of *tbx2b* mutant retinas 29
3.2 Müller glia ablation experiment: ablation group data 53
3.3 Müller glia ablation experiment: control group data 55

LIST OF APPENDICES

A MATLAB Codes **70**

B Additional Methods for Chapter 4: Correlation Analysis of Morphogenetic Noise **96**

C 2017 Nature Communications Manuscript: Anisotropic Glial Scaffolding Shapes a Multiplex Photoreceptor Mosaic in Zebrafish Retina **100**

ABSTRACT

Developmental biology is a study of how elaborate patterns, shapes, and functions emerge as an organism grows and develops its body plan. From the physics point of view this is very much a self-organization process. The genetic blueprint contained in the DNA does not explicitly encode shapes and patterns an animal ought to make as it develops from an embryo. Instead, the DNA encodes various proteins which, among other roles, specify how different cells function and interact with each other. Epithelial tissues, from which many organs are sculpted, serve as experimentally- and analytically-tractable systems to study patterning mechanisms in animal development. Despite extensive studies in the past decade, the mechanisms that shape epithelial tissues into functioning organs remain incompletely understood. This thesis summarizes various studies we have done on epithelial organization and patterning, both in abstract theory and in close contact with experiments. A novel mechanism to establish cellular left-right asymmetry based on planar polarity instabilities is discussed. Tissue chirality is often assumed to originate from handedness of biological molecules. Here we propose an alternative where it results from spontaneous symmetry breaking of planar polarity mechanisms. We show that planar cell polarity (PCP), a class of well-studied mechanisms that allows epithelia to spontaneously break rotational symmetry, is also generically capable of spontaneously breaking reflection symmetry. Our results provide a clear interpretation of many mutant phenotypes, especially those that result in incomplete inversion. To bridge theory and experiments, we develop quantitative methods to analyze fluorescence microscopy images. Included in this thesis are algorithms to selectively project intensities from a surface in z-stack images, analysis of cells forming short

chain fragments, analysis of thick fluorescent bands using steerable ridge detector, and analysis of cell recoil in laser ablation experiments. These techniques, though developed in the context of zebrafish retina mosaic, are general and can be adapted to other systems. Finally we explore correlated noise in morphogenesis of fly pupa notum. Here we report unexpected correlation of noise in cell movements between left and right halves of developing notum, suggesting that feedback or other mechanisms might be present to counteract stochastic noise and maintain left-right symmetry.

CHAPTER 1

Introduction

This thesis is born out of my 5 years of PhD research at the University of Michigan, where I joined a computational and theoretical biophysics group led by David K Lubensky. Purely theoretical biophysics research can be dangerous, in the sense that it is too easy to create models that do not correspond to biological reality. Indeed, as physicists, we often underestimate the complexity of biological systems. Traditional physical systems tend to be simple and elegant, and when there are complicating details one usually can work in a regime where they are negligible. The same thing cannot be said in biology. Biological systems are often inherently 'messy' and complicated, often without the clear separation between important and negligible details that we are so used to in physical systems. It thus can be hard (sometimes even impossible) to come up with sensible models without guidance from experimental data.

Being a non-experimental biophysics group, we often rely on collaborations with others to perform experiments and collect data. Hence, the work we do is as varied as the collaborations we have forged over the years. Looking at different biological systems, from insect to vertebrate, is not unusual. The spectrum of analysis we do is also equally broad, ranging from purely mathematical modeling to numerical simulation to microscopy image processing. This variety of topics will be reflected in this thesis, where each chapter is dedicated to a different and independent topic.

Given the wide variety of things we did, I think it is wise to delay giving introduction and background of specific topics to the beginning of the respective chapters. This has the advantage of making each chapter independent of each other, so readers can jump directly to chapters that interest them without having to read the preceding ones. For the rest of this introductory chapter, I will only give broad introduction to a theme that ties the whole thesis together: organization and patterning of epithelial tissues.

Developmental Biology and Self-Organization

Developmental biology studies the growth and formation of various organs. Life of an animal starts from a single, fertilized egg cell. As it develops, the egg divides into multiple cells carrying the same genetic materials. As soon as the embryo reaches a stage with several number of cells, more elaborate development process kicks off. This includes differentiating specific cells into different types, reshaping tissues by exerting mechanical forces, signaling and secreting morphogens, and many more. All these require precise spatio-temporal coordination to turn the embryo into an adult animal with complex organ shapes and functions.

While it is easy to attribute the above process to the genetic materials in the DNA, it is important to realize that they do not contain explicit information on the eventual shape of the animal. The DNA encodes proteins that, among other functions, determine how cells should behave and interact with each other. This interaction between cells is arguably as important as the genetic blueprint itself in determining the eventual outcome of the development. The final shape of an organ then emerges from specific interaction and behavior of the underlying cells.

It is no coincidence that many physicists find the field of developmental biology fascinating: the development process sketched above resembles self-organization phenomenon found in many physical systems, albeit in a much more complex setting. While genetic materials specify how different cells should function and interact, the final shape of the animal is an emergent result from the dynamics of the underlying cells with minimal external intervention.

On the Organization of Epithelial Sheets

A major theme in developmental biology is self-organization of cells into functional organs. In animal development, epithelial tissues form basic building blocks on which more complex organs are sculpted [1–5]. An epithelium consists of a sheet of cells adhering tightly to their neighbors through some specialized apical junctions. Here apical junctional proteins bind neighboring cells together to form a physical barrier separating the space above and below the tissue. This adhesion also gives the epithelial sheet its integrity and tensile strength [6–9]. Inside each cell, the junctional protein complexes (e.g. adhesion proteins) are connected to networks of actins and myosins, and in particular to the band of cortical actin located right next to the junctions. These actomyosin networks in turn interact with signaling pathways that coordinate changes in cell morphology and fate [10, 11], allowing

remodeling of epithelial tissues through active and coordinated cell movements.

Since the epithelial cells adhere tightly to each other, it is often useful to model this layer of cells as a two-dimensional object with mechanical integrity [12–17]. It also means that mechanical forces can be propagated through the plane and influence tissue shape. Two major sources of mechanical force on this plane are thought to be: (1) cell-cell adhesion and (2) myosin-dependent cytoskeletal contraction [18, 19]. At the single cell level, these forces allow cells to change their apical shapes and mechanically influence their immediate neighbors. When such actions are coordinated across many cells, tissue-scale remodeling can be achieved.

One example of collective tissue remodeling is epithelial invagination driven by apical constriction. In this process, contraction of the acto-myosin band causes cell apical area to shrink. When the apical area constriction is coordinated across many cells, shrinkage on the apical surface (but not on the basal surface) of the epithelium causes the tissue to bend. This process is important in many development processes, for example in forming ventral furrow of *Drosophila* embryo [20, 21]. The ventral furrow, driven by coordinated apical constrictions, is a stage of fly embryo development where epithelial cells at the surface invaginate into the embryo to make internal organs of the animal.

Apical constriction-driven tissue invagination is far from being the only way nature sculpt epithelial tissues. Activity of the acto-myosin network can induce epithelial cell rearrangements to achieve specific goal, such as growing tissues in a certain direction [22–27]. Similarly, cell-cell adhesion can also drive morphogenesis. It has been shown in *Drosophila* eye that cadherin-mediated adhesion can generate complex patterns [13,15,28]. Differential adhesion between cells of different types is also known to facilitate cell sorting, forming physically distinct epithelial compartments, and maintaining straight compartment boundaries [16, 29–32]. Yet in some other cases, external mechanical stress of various origin, transmitted throughout the tissue via cell adhesion and cytoskeletal contractility, can also play role in tissue morphogenesis [25, 33, 34].

To achieve a more complex morphogenesis, often a preferred direction is established and communicated throughout the epithelial tissue. This is commonly achieved in epithelium through the so-called planar cell polarity (PCP) mechanism. It refers to the ability of individual cells to assume common polarization on the apical plane of the epithelium through asymmetric protein localizations [35–37]. The asymmetrically-localized proteins could be some adhesion complexes, or signaling molecules that affect adhesions and cytoskeletal functions. Physically this amounts to breaking rotational symmetry. Directional information can be propagated from one cell to the next through homo- or hetero-typic binding of intercellular protein complexes. These proteins can be the same ones as the PCP

proteins, or can be different but connected to the polarity through some signaling pathways. It has been shown that, when combined with appropriate initial condition, PCP can reliably and collectively orient epithelial cells along some direction [38].

Breaking rotational symmetry and picking a preferred direction allows for a more complex, non-isotropic tissue remodeling that otherwise is not possible. One example is a process called convergence-extension, where an epithelium elongates through a series of directional cell intercalation [39–45]. Here planar cell polarity plays role in picking the direction which cell intercalation should happen. Another classical example of PCP is the uniform growth of bristles in *Drosophila* wings, where PCP determines the orientation of the bristles that grow from the wing epithelial cells. Many other examples of PCP driving rotationally-asymmetric development are given in [36–38, 46–50], illustrating the importance of breaking rotational symmetry to achieve complex morphogenesis.

Yet more complex organ shaping can be achieved by lowering the symmetry even further and break reflection symmetry. This amounts to establishing chirality in the tissue to allow for left-right asymmetric organs to be formed. Conventionally, chirality at tissue scale is thought to originate from molecular handedness [51–58]. A classic example of this is the nodal flow in vertebrate, where a cillia-driven fluid flow establishes left-right axis in embryos. The rotating cillia are driven by molecular motors composed of chiral molecules, causing them to rotate only in one direction. Another example linking molecular and tissue-scale chirality is torque-generating acto-myosin contraction that establishes the left-right axis of *C. elegans* embryos [52]. Both actin and myosin are chiral, and their contraction generates torque dipole that is then sensed by the embryos.

Despite the existence of several mechanism linking tissue chirality to molecular handedness, it is not clear that if such system is always at play. Recently, there have been studies showing that formation of several left-right asymmetric organs are driven directly by chiral epithelial cells. Once the epithelial cells are chiral, they can drive left-right asymmetric tissue remodeling through, for example, chiral cell intercalation, signaling, and force exertion. One example is the *Drosophila* embryonic hindgut, which starts as a straight, symmetric tubes that later makes a left-hand twist. The direction of the twisting is consistent in all wildtype flies, and have been shown to originate from the left-right asymmetric intercalation of the epithelial cells [59–61]. Similarly, chiral epithelial cells has been shown to initiate chiral morphogenesis in adult fly gut and genitalia [58, 60, 62].

Motivated by this, we explore an alternative mechanism where cell chirality can arise spontaneously from PCP protein interactions. In this framework, instability in protein-protein interactions give cells intrinsic tendency to be chiral. External cues, such as that from molecular chirality, can then bias the system to the direction seen in wildtype. We

show that generic PCP interactions are sufficient to produce the said chiral instability, and that in principle no new biological machinery beyond PCP is needed to establish cellular chirality. We show that the proposed model results in clear interpretation of many mutant phenotypes, especially those that result in incomplete inversion.

On the Organization of the Thesis

Just as epithelial tissues have to be organized to perform specific functions, I believe proper organization of the thesis is crucial for its usefulness. Given the wide spectrum of topics discussed, chapters are designed to be independent of each other. More specific introduction, background, and motivation pertaining to a specific topic are given at the beginning of each chapter.

Chapter 2 discusses a theoretical study of spontaneous chiral symmetry-breaking from generic PCP mechanisms. Most animal body plans have some degree of left-right asymmetry. This chirality is conventionally thought to originate from handedness of biological molecules. However, how the chirality is transferred from molecular to tissue scales is not clear. Here we propose an alternative paradigm where chirality results from spontaneous symmetry-breaking. We showed that PCP systems, which are commonly found in epithelial tissues, can generically produce this chiral instability. Our results have clear implications for the interpretation of many mutant phenotypes, especially those that result in incomplete left-right inversion. This work is written as a manuscript for submission to Physical Review Letters, and will be presented as such.

Chapter 3 describes a larger, still ongoing project to understand the mechanisms patterning retinal cone photoreceptors into a near crystalline array in zebrafish. In this project I did mostly quantitative image analysis and programming to better understand and quantify fluorescence microscopy data. Hence, emphasis will be put on describing in more details the analysis procedures. The project spans multiple published and submitted works that combine experiments with quantitative analyses and computer simulations. While enough background and results will be given to put the analysis procedures into context, interested readers are invited to read the published papers, cited in the text, for a more complete picture.

Chapter 4 summarizes the work we did in collaboration with the Bellaïche group in Institut Curie, Paris, where we spent wonderful 6 months of 2015 in their lab. Here we looked at morphogenesis of *Drosophila* dorsal notum and how it can maintain symmetry between its left and right halves in the presence of biological noise. At tissue scale, the notum maintains its symmetry throughout the development. However at cellular scale, cell

divisions and other stochastic processes impart observable noise to individual cell trajectories. Hence it is unclear how the epithelial tissue can maintain its symmetry despite this noisy movement of the underlying cells. Looking at the correlation of cell movements between the two halves gave us insight into whether any sort of feedback or correction mechanism is at work to counteract the noise and maintain they symmetry. We found that the noise from both halves is non-trivially correlated and does not match predictions from a naïve stochastic model with simple noise. Several interesting auto-correlation results are also discussed and compared to known features of the notum morphogenesis.

Additional materials that are not central to the main story but might be of interest to some readers looking for more details are given in the Appendices. Appendix A contains MATLAB routines used in Chapter 3. A manuscript of our most recent work, submitted to Nature Communications at the time of writing, is given in Appendix C and contains our work presented in Sections 3.4 and 3.5. Readers interested in the said sections are invited to read the manuscript for a more comprehensive picture. Appendix B gives additional methods for Chapter 4.

Finally, it is my hope that our works outlined here contribute to the collective understanding of self-organization and patterning in biology. This thesis summarizes the work I have done during my PhD years. At the very least, I hope that this thesis can benefit others, especially future researchers in the Raymond and Lubensky labs who will continue working on related topics.

CHAPTER 2

Spontaneous Chiral Symmetry Breaking in Planar Polarized Epithelia

Jeremy Hadidjojo and David K. Lubensky
Department of Physics, University of Michigan, Ann Arbor, Michigan 48109-1040, USA
(Manuscript for Physical Review Letter, May 10, 2017)

2.1 Abstract

Most animal body plans have some degree of left-right asymmetry. This chirality at the tissue and organ level is often assumed to originate from the intrinsic handedness of biological molecules. How the chirality is transferred from molecular to tissue scale during development, however, is not well understood. Here we propose an alternative paradigm where tissue chirality results from spontaneous symmetry breaking, with molecular chirality acting only as a weak bias that ensures that one handedness predominates over the other. In particular, we show that systems capable of generating planar polarity, found in many epithelial tissues, can also generically break left-right symmetry, and we identify the key interaction parameters that must be varied to access the chiral phase. In addition to a chiral polar phase corresponding to one found in liquid crystal films, a chiral nematic phase with no liquid crystal analog is also possible. Our results have clear implications for the interpretation of the phenotypes of many mutants, especially those that result in incomplete inversion.

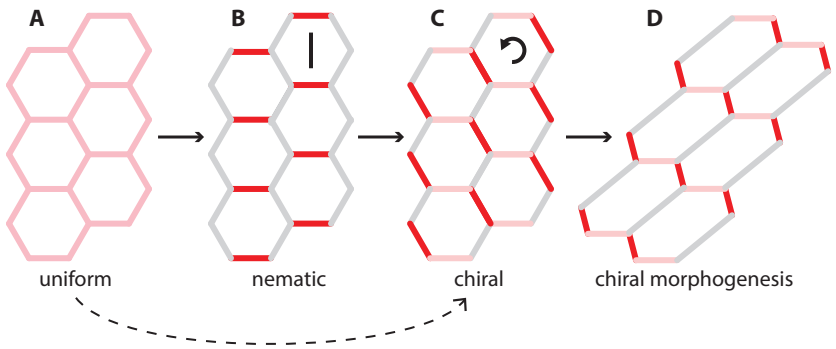

Figure 2.1: Chiral morphogenesis driven by spontaneous left-right symmetry breaking. Cells (hexagons) in an epithelial sheet have an initially uniform membrane protein distribution (A) which goes unstable to an intermediate polar (not shown) or nematic (B) state before a secondary instability to a final chiral distribution (C); in certain special cases, a direct transition from isotropic to chiral is possible (dashed line). Cell and organ shapes then develop a definite handedness in response to chiral protein distribution (D).

2.2 Introduction

It is only a small exaggeration to view animal development as a progressive breaking of symmetries through which an egg's simple shape gradually transforms into an elaborate adult form. One example of such a broken symmetry is the reflection symmetry linking left and right: Everything from the twist of the *Drosophila* gut to the orientation of the human heart has a definite handedness, but how this handedness is reliably chosen during development remains unclear in most cases. With few exceptions [63], researchers have typically assumed that chirality at the cellular level and above originates directly from molecular handedness [51–56]. In this spirit, considerable effort has gone into exploring mechanisms that might directly transduce chirality from molecular to cellular scales [62, 64–66]. Here we argue that an alternative scenario, wherein cellular handedness results instead from spontaneous left-right symmetry breaking, may be equally widespread. In this picture (Fig. 2.1), the basic mechanism of symmetry breaking does not depend on molecular chirality and does not favor one handedness over the other. (Molecular handedness can, however, bias this intrinsic tendency towards chirality to ensure that wildtype animals always break symmetry in the same direction.) Specifically, we show that the planar cell polarity (PCP) systems that determine a preferred direction in many epithelial tissues are generically also capable of spontaneous left-right symmetry breaking. Thus, establishing cellular chirality may not require any new biological pathways or molecular mechanisms beyond those already characterized for PCP.

Recent experiments on development of various *Drosophila* visceral organs have high-

lighted the role played by cellular chirality. These organs are formed by epithelial sheets, where approximately polygonal cells are joined together to form 2D layers of tissue (Figure 2.1, left). The cells are observed to have intrinsic handedness that drive chiral morphogenesis. In the embryonic hindgut twist, for example, the cells are shown to displace their centroids chirally at an angle and have chiral DE-Cadherin protein localization around their membranes (illustrated in Figure 2.1, middle) [59, 60]. In adult male genitalia, cells in A8 domain are seen to have chiral Myosin II distribution and undergo left-right asymmetric T1 topological transitions that leads to clockwise tissue rotation [57]. Myosin ID has been shown to influence the direction of handedness [57–59, 67, 68]. In embryonic gut, a mutation of *myosinID* results in a bimodal distribution of correct and inverted, but not loss of, chirality [69]. This suggests the presence of some mechanism that favors breaking chiral symmetry, which then can take cues from elsewhere to consistently bias it to the correct wildtype direction. Furthermore in the first evidence showing a connection between chirality and PCP, González-Morales *et. al.* showed that both Ds/Fat and Fz/Dsh/Dgo PCP pathways commonly found in epithelial tissues are involved in establishing cell chirality for proper adult hindgut looping [58]. Guided by these observations, we asked the question of whether PCP can lead to spontaneous chiral symmetry breaking. We show that the chiral states can be reached from both disordered and ordered states, and it requires no new interaction beyond those generic to PCP.

This paper is organized as follow: first we will show based on general symmetry arguments that concentration of membrane proteins in a lattice of cells can have polar chiral (P^*) and nematic chiral (N^*) modes. For regular hexagonal cells both modes are accessible only through some intermediate, non-chiral ordered phases, and direct isotropic (I) to either chiral mode is forbidden. Although transitions to the P^* phase have been described in the context of tilted liquid crystals [70, 71], spontaneous symmetry breaking into N^* phase is not usually present in traditional $2D$ systems and, to our knowledge, has not been studied before. To understand interactions important for chirality, we take a simple mean-field model of PCP that is initially designed to produce polar concentration [72, 73] and show what parameters need to be varied to achieve the chiral configurations. Finally, we will show that direct $I - N^*$ transition is possible in two different scenarios where: (1) we have stretched hexagon with D_2 symmetry, or (2) we have two species of proteins with symmetrical interaction.

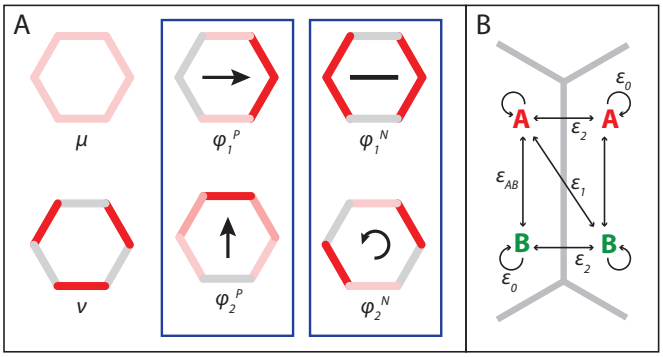

Figure 2.2: Cartoons of rreducible representations and mean-field PCP model. (A) Irreducible representations of protein concentration on regular hexagon (D_6 point group symmetry). μ and ν are $1D$ uniform and alternating representations, respectively. Boxed: $2D$ representations that transform like polar (left) and nematic (right). (B) Cartoon of protein interactions in the mean-field PCP model described in [72]. A and B are two different species of transmembrane proteins, and the parameters set interaction strengths between: unlike proteins (ϵ_{AB}) and like proteins on the same side (ϵ_0), unlike protein (ϵ_1) and like proteins (ϵ_2) across an interface. J_1, J_2, T, and $c_{\max}$ are not drawn and are described in the text and in ref [72].

2.3 General symmetry arguments

We begin by working out the generic behavior dictated by symmetry near an instability from an isotropic and achiral state [74]. For concreteness, we consider a field of identical hexagons with multiple protein species $A, B, C, \ldots$ concentrated on the edges, but because they are based only on symmetry considerations, the arguments in this section apply equally well to systems where the concentrations of proteins in the cytosol, the orientations of cytoskeletal filaments, or similar factors play an important role. We restrict ourselves to the spatially uniform case in which every cell has an identical protein distribution. As usual, we expect that only one mode will initially go unstable, which must correspond to some linear combination of protein concentrations (e.g. $A-B$ or $A+B$) whose amplitude varies from edge to edge according to a representation of the symmetry group D_6 of the hexagon. Denote the coefficients of the appropriate linear combination on the six edges as $c_1, \ldots, c_6$; these are assumed to follow the deterministic dynamics $\dot{\mathbf{c}} = f(\mathbf{c})$. Decomposing the 6 concentrations into irreducible representations yields the modes shown in Fig. 2.2A. The first mode, μ, encodes the total protein number and is fixed in this study. The two two-dimensional representations correspond to polar and nematic order parameters. In principle, they could be expressed in terms of any linear combination of the basis vectors shown in Fig. 2.2a. The choices of basis shown in the figure lend some convenience,

however, since now we can write the concentrations in terms of a complex order parameter $z = \phi_1 + i\phi_2$, where ϕ_1 (ϕ_2) is the coefficent of the corresponding basis vector. In this formulation, reflection through the x-axis is simply complex conjugation of z, and rotation by $\pi/6$ corresponds to multiplication of z by $e^{i\frac{\pi}{3}}$ ($e^{i\frac{2\pi}{3}}$) in the polar (nematic) case.

Suppose for the moment that the initial instability is towards a nematic distribution. We can expand the dynamics of the unstable mode in a power series, keeping only terms allowed by symmetry [74]:

$$\dot{z} = az + 3b\bar{z}^2 + 2c|z|^2 z + \dots. \tag{2.1}$$

Although the general dynamics $\dot{\mathbf{c}} = f(\mathbf{c})$ is not variational, all of the terms shown above can be written as the gradient of an appropriate free energy; at low order, active, far-from-equilibrium systems are hence indistinguishable from equilibrium ones. In fact, it is not until the 4th order in the nematic expansion (8th order in polar) that we get non-variational terms.

The bifurcation diagram corresponding to (2.1) follows a well-established pattern [74]. Writing $z = re^{i\theta}$, and keeping higher order terms in $\dot{\theta}$ than in Eq. 2.1, we obtain:

$$\dot{r} = ar + 3br^2\cos(3\theta) + 2cr^3 + \dots, \tag{2.2}$$

$$\dot{\theta} = -3br\sin(3\theta) - dr^3\sin(3\theta) - 6fr^4\sin(6\theta) + \dots. \tag{2.3}$$

To lowest order in r, the fixed point has $\theta = 0$ or $\theta = \frac{\pi}{3}$ depending on the sign of b, both of which correspond to the non-chiral configuration ϕ_1^N in the nematic representation. A similar treatment for the polar case shows that only either ϕ_1^P or ϕ_2^P is a stable fixed point near enough to the initial bifurcation. Thus, no chiral state is smoothly accessible from isotropic (though we note that the nematic transition is generally subcritical in r, an interesting possibility we will address shortly).

Once some order has been established, however, there can be a secondary transitions into a chiral state. Near enough to an initial bifurcation, we expect that r will be set primarily by low order terms without angular dependence, and we can then focus on finding the fixed point of θ from Eq 2.3, which takes the form [1]:

$$\dot{\theta} = -h_3(r)\sin(3\theta) - h_6(r)\sin(6\theta). \tag{2.4}$$

This is analogous to the description of tilted liquid crystal films studied by Selinger and

[1] More generally, one can imagine solving for r at the fixed point as a function of θ; no qualitatively new behavior will arise as long as $r(\theta)$ is smooth.

Nelson [70, 71], except for the non-variational term $-dr^3 \sin(3\theta)$ in Eq 2.3. Note that this and all higher order non-variational terms carry no new θ-dependence, and so their presence does not affect the qualitative behavior of the system [2]. It follows that for $h_6 < 0$ we have continuous transition between N and N^*, with the angle varying smoothly between $0 \leq \theta \leq \frac{\pi}{3}$. In the case of $h_6 > 0$ we have discontinuous transition between two N states.

The polar case has been worked out in [70,71], and we repeat the results for comparison: the case $h_{12} < 0$ yields continuous transition between ϕ_1^P (vertex-polarized, $\theta = 0$) and ϕ_2^P (edge-polarized, $\theta = \frac{\pi}{6}$) through intermediate chiral state P^* with smoothly-varying θ. On the other hand, $h_{12} > 0$ results in discontinuous transition between ϕ_1^P and ϕ_1^P with no intervening chiral state.

Although treatment for the polar case closely parallels that of the nematic, interestingly it leads to results with different physical interpretations. Depending on the sign of the two lowest θ-dependent terms, close to instability the polar mode can have $\theta = 0$, $\theta = \frac{\pi}{6}$, or continuously-varying $0 \leq \theta \leq \pi/3$. This corresponds to locked vertex-polar VP, locked edge-polar EP, and unlocked P^* phases seen in liquid crystals [70, 71]. Similar analysis with the nematic mode gives exactly the same solutions. However, both $\theta = 0$ and $\theta = \frac{\pi}{6}$ correspond to the same non-chiral ϕ_1^N phase (up to a minus sign).

It is also worth noting that nematic isotropic-to-order transition is generally discontinuous. This leads to an interesting possibility for a system to break both the primary rotational and secondary chiral symmetries at the same time, with the intermediate ordered state unobservable. This phenomenon is absent in the polar case (and thus in the classical studies of liquid crystals) as isotropic-to-polar transition is continuous.

Finally, this result implies that polarity and chirality go together, and that known systems capable of making polarized protein concentrations can, in principle, make chiral concentrations with appropriate choice of parameters. However, this poses an open question of whether the said parameter values are within the biologically-attainable range.

2.4 Mean-field PCP model

To gain some understanding on what interactions need to be tuned to make PCP chiral, we took a simple mean-field model of PCP [72,73]. This model minimizes a free energy, but as discussed above it is sufficient to get the generic phase behavior. Here we have two species of membrane-bound proteins A and B that follows variational dynamics $\alpha \dot{\mathbf{c}} = -\nabla_{\mathbf{c}} F$, with:

[2] Alternatively: ignoring r, the dynamics reduces to one dimension, and $\dot{\theta}$ can therefore can always be written as a gradient of some energy function.

$$
\begin{aligned}
F = \sum_{\substack{\text{cells}\\ \alpha}} \Bigg\{ \sum_{\substack{\text{edges}\\ i\in\alpha}} \frac{1}{2}\epsilon_{AB} l_i c_A^{\alpha,i} c_B^{\alpha,i} - \frac{\epsilon_0}{2} l_i \left(c_A^{\alpha,i}\right)^2 + \sum_{\substack{i\in\alpha\\ \beta \text{ shares}\\ i \text{ with } \alpha}} -\epsilon_1 l_i c_A^{\alpha,i} c_B^{\beta,i} - \epsilon_2 l_i c_A^{\alpha,i} c_A^{\beta,i} \\
+ \sum_{\substack{i,j\in\alpha\\ \langle i,j\rangle}} \frac{J_1}{2}\left(c_A^{\alpha,i} - c_A^{\alpha,j}\right)^2 - \frac{J_2}{4}\left(c_A^{\alpha,i} - c_B^{\alpha,j}\right)^2 + T\sum_{i\in\alpha} l_i \Big[c_A^{\alpha,i} \log\left(c_A^{\alpha,i}\right) \\
+ \left(c_{\max} - c_A^{\alpha,i}\right) \log\left(c_{\max} - c_A^{\alpha,i}\right) \Big] \Bigg\} + (\text{interchange } c_A \leftrightarrow c_B),
\end{aligned}
\tag{2.5}
$$

where ϵ's are parameters controlling the strength of quadratic interactions of various species (see Figure 2.2b), J's set penalty for abrupt concentration jumps, T is temperature-like parameter, and $c_{\max}$ sets the maximum protein concentration an edge can hold.

The total number of both protein species in a cell is normalized according to $\sum_i l_i c_A^i = 1 + \delta$ and $\sum_i l_i c_B^i = 1 - \delta$. For simplicity, we choose parameters such that the energy (2.5) is symmetric between A and B, and tune the asymmetry by giving them unequal protein number parametrized by δ. The presence of two symmetrically-interacting species introduces two copies of irreducible representations shown in Figure 2.2a, one for the $A-B$ and another for the $A + B$ modes. Here we focus on the modes that are (approximately) $A - B$ for (non-)zero δ.

Although the model was designed to produce polarized concentration [72], we showed that with appropriate choice of parameters it is capable of spontaneously breaking chiral symmetry as predicted (Figure 2.3). Not surprisingly, nematic configuration depends on ϵ_1/ϵ_2, which is the ratio of interaction favoring polar to nematic. Another key parameter is $c_{\max}$, which can be thought of setting the number of edges with high protein concentration. In high $c_{\max}$ regime, configurations with few high edges are preferred. This necessarily leads to non-chiral states in polar mode. As $c_{\max}$ is lowered, saturation forces distribution of proteins into more edges, which can trigger transition into chiral states (Figure 2.3).

In the nematic regime ($\epsilon_1/\epsilon_2 \ll 1$), we observe supercritical (continuous) transition between N and N^* phases. For high $c_{\max}$, we have chiral nematic N^* phase with nematic director angle $0 < \theta \leq \frac{\pi}{2}$ varying continuously. Nonchiral nematic N only occurs at relatively low $c_{\max}$, where it is favorable for one species to occupy four opposing edges. In the polar regime ($\epsilon_1/\epsilon_2 \gg 1$), we observe both subcritical (discontinuous) transition between edge-polar (EP) and vertex-polar (VP) as well as supercritical transition with intervening chiral P^* state, as predicted in [70, 71].

[4]Configurations where neighboring cells are mirror reflection of each other were checked to have higher

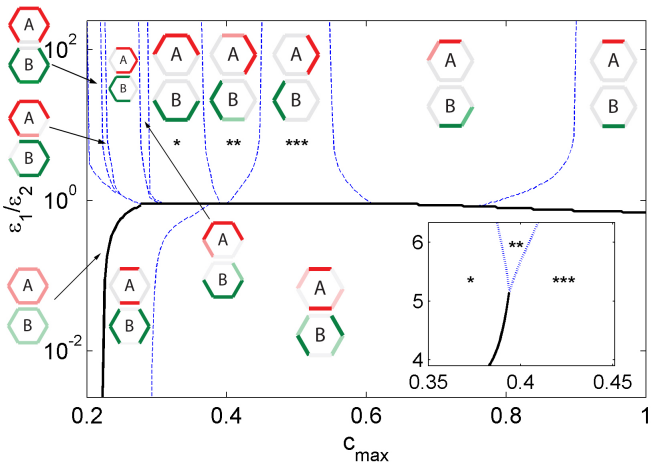

Figure 2.3: Phase diagram of mean-field PCP model on regular hexagon, showing various polar and nematic chiral phases. Dotted (solid) lines indicate (dis)continuous transitions. ϵ_1/ϵ_2 is the ratio of interaction favoring polar to nematic; $c_{\max}$ sets maximum number of protein an edge can hold. $l = \epsilon_{AB} = 1$, $\epsilon_0 = 0.02$, $\epsilon_2 = 0.41$, $J_1 = 0.025$, $J_2 = 0.03$, $T = 0.068$ and $\delta = 0.1$. **Inset.** $T = 0.3$ showing P^* region ends in a 1st-order transition between VP and EP states, stars denote corresponding phases. Phases found by numerically minimizing free energy (2.5) with periodic boundary condition from multiple random starting points [4].

2.5 Direct I $\rightarrow$ N* transitions

Although direct continuous $I - N^*$ is prohibited by D_6 symmetry, we found two special cases in which it is allowed: (1) when the cells are stretched so the symmetry is lowered to D_2 and (2) when the two protein species A and B have perfectly-symmetrical interactions.

In the first case, stretching regular hexagons splits both polar and nematic representations into four different $1D$ representations ϕ_1^P, ϕ_2^P, ϕ_1^N, and ϕ_2^N. Writing dynamics expansion similar to Eq 2.1 of ϕ_2^N, one quickly sees that reflection symmetry prohibits quadratic term and thus the system has continuous phase transition. Indeed, we verify that the mean-field PCP model on stretched hexagons exhibits this direct continuous $I - N^*$ transition (Fig 2.4). Biologically, epithelial tissues are frequently under tension along some body axis. Thus, this result suggests a way that these tissues can directly break left-right symmetry without going through some intermediate states.

In the second case, having two symmetrical species introduces a new exchange symmetry to the $A - B$ modes, forcing the dynamics to be invariant with respect to $z \rightarrow -z$. This excludes all even order terms in Eq 2.1, leaving only linear and cubic terms at the lowest order that leads to a continuous phase transition. This special case might be realizable

energy for all parameters shown.

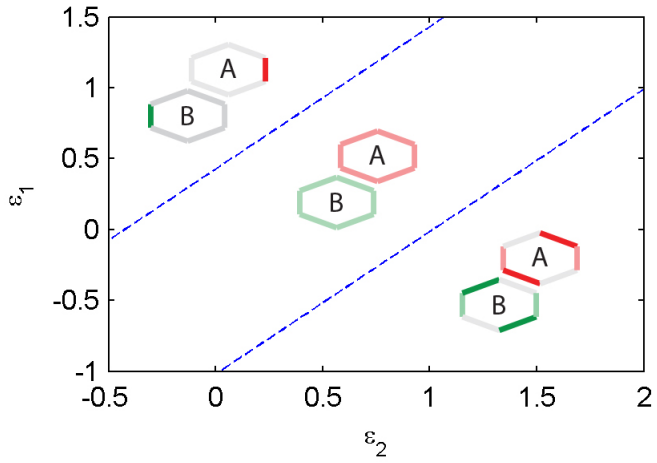

Figure 2.4: Phase diagram of mean-field PCP model on stretched hexagon, showing direct continuous $I - N^*$ transition that does not exist in D_6 symmetry. The length of long and short edges are defined as $L + dL$ and $L - dL$ respectively. Parameters are identical to Figure 2.3 except $dL = 0.3$, $J_2 = -0.8$, and $c_{\max} = 0.7$.

in vitro using, for example, lipids. Since lipids can be synthesized without using (chiral) enzymes, one might be able to preserve both enantiomers of the same adhesion molecule. Weakly breaking this symmetry still preserves the chiral phase, but introduces a narrow intervening non-chiral state (see Figure 2.5).

2.6 Discussion

In this work, we showed that polarizable systems can in general break chiral symmetry. This suggests a scenario where PCP is responsible for the cell chirality observed in experiments. In line with this story, a recent report by Gonzáles-Morales *et. al.* [58] demonstrated that the classic Fat/Ds and Fz/Dsh/Dgo PCP pathways are required in maintaining left-right asymmetry in adult fly gut looping. Here they showed that, unlike mutants of *MyosinID* that shows inverted handedness, mutants of *Ds* exhibit complete loss of chirality suggesting that *Ds* plays a central role in cell chirality.

The presence of mutants with both correct (wildtype) and inverted laterality provides another evidence in favor of spontaneous symmetry breaking. In the fly gut mutation of *myosin ID* leads to a bimodal distribution of correct and inverted looping [69]. Similarly in male genitalia rotation, flies with impared *sqh* function show a mix of left- and right-chiral cells in the A8 domain [57]. This bimodality suggests the existence of a mechanism responsible for establishing chirality that is separate from Myosin ID, and that the latter

might influence the former only in selecting the correct handedness. Experimentally, this can be tested by knocking down Myosin ID to varying degrees. A model in which Myosin ID is central in establishing chirality is predicted to simply lose laterality as more Myosin ID function is disrupted. In contrast, a model with an independent chiral instability mechanism is predicted to transition from consistent wildtype laterality to random laterality (in absence of any cues), or to inverted laterality (if there is a secondary cue favoring such) as Myosin ID function is impaired.

PCP-based chirality also gives a natural, built-in way to couple neighboring cells. It has been proposed that cell chirality is propagated throughout the tissue from a localized domain termed 'left-right organizer' [58, 75]. Here they showed that abolishing chirality in this domain early on results in complete loss of chirality throughout the organ. Although further studies need to be done to understand the mechanism responsible for propagating chiral information, we note that PCP-based chirality provides a natural way to do this.

In systems where cells have regular hexagonal symmetry, both polar and nematic chiral states are only reachable through a secondary instability from some (non-chiral) ordered states. Direct transition from isotropic is forbidden by symmetry. However, perfect hexagonal packing is rarely found in living tissue. Often epithelial cells are stretched along some body axis. Interestingly, we found that lowering the symmetry from D_6 to D_2 makes some chiral states more accessible in general. Particularly, this allows previously-forbidden direct continuous isotropic to chiral-nematic transition. This suggest that stretching or applying tension on the tissue might be favorable for breaking chiral symmetry. Similarly, having two protein species with perfectly symmetrical interactions can help by allowing continuous $I - N^*$ transition in regular hexagonal packing. Although finding a system that exhibits perfect exchange symmetry might be difficult *in vivo*, it may be realizable *in vitro* using lipids synthesized non-enzymatically to preserve both enantiomers of the molecule.

Perhaps most importantly, our results suggest that spontaneous breaking of chiral symmetry requires no new biological pathway. Instead, we show that PCP pathways commonly found in epithelial tissues are generically capable of producing spontaneous chiral protein localization by appropriate modulation of various components. This can be done in many different ways: genetically by up/down-regulation of various PCP components, biochemically by changing affinity of the interacting proteins through binding/unbinding of modifier molecules, or even mechanically by changing cell shape or subjecting the tissue to tension. Once chiral concentration has been established, it can be used in many ways. For example, it could affect cell functions such as preferentially shrink and remodel junctions in a left-right asymmetric way and drive chiral morphogenesis as observed in [57, 59, 76], or it can be propagated out to establish chirality in neighboring cells as suggested in [58].

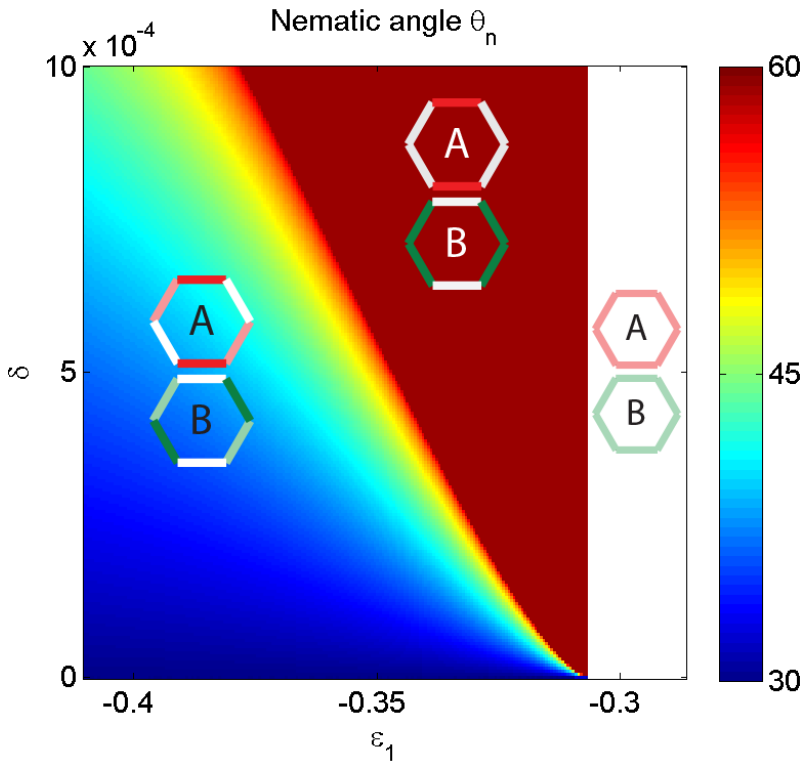

Figure 2.5: Phase diagram of mean-field PCP model on regular hexagon with slight asymmetry in A & B interactions, showing that chiral phase persists with an intervening non-chiral state upon breaking the A-B exchange symmetry. Symmetry between proteins A and B in the free energy is broken by giving them unequal protein number parametrized by δ: $\sum_i l_i c_A^i = 1 + \delta$ and $\sum_i l_i c_B^i = 1 - \delta$. Note that at $\delta = 0$ we have direct continuous I-N*, with the latter phase locked at $\theta_n = 30°$.

Finally although we only consider a variational PCP model for this demonstration, we showed that the same qualitative results still hold for non-equilibrium models. We also note that only the noise-free, spatially-uniform hexagonal case is considered here. It is known that fluctuations in low dimension and non-equilibrium noise can change qualitative behavior of a system on a long enough lengthscale [77, 78], however we expect the treatment presented here remains appropriate on shorter scales, possibly including biological tissues with a few thousand cells or less. We also expect to see more interesting behaviors as we include noise or allow spatial non-uniformity [79].

CHAPTER 3

Quantitative Analysis of Fluorescence Microscopy Images

In order to make models that are biologically relevant and predictive, one inevitably has to come in contact with experiments and deal with biological data. As most of our data come in the form of fluorescent microscopy images, we spent significant amount of time analyzing and processing those images. This ranges from simply building tools to better understand the data to extracting some quantitative measures to guide modeling and test hypotheses. This chapter is an effort to collect all the image analysis techniques we have successfully applied throughout the years.

In writing this chapter, emphasis is put on providing enough details of the algorithms and decision choices with the hope that interested readers not only can understand the rationale behind the techniques, but are also able to adapt and apply them to their own problems. Just enough biological background and results will be provided to put the techniques into context. When a work has been published, proper citations are given and interested readers are invited to read the published papers for more complete picture of biological relevance and impact.

This chapter is organized as follow: First, we give a brief introduction of zebrafish retina, where photoreceptor cells exhibit a high degree of crystalline order (Section 3.1). Most of the image analysis work was done on this system examining the patterning mechanism. Section 3.2 discusses column fragment analysis of *tbx2b* mutant fish retina. In this mutant, although the crystalline order is lost, there is some local remnant of wildtype order. Section 3.3 discusses a very useful algorithm to project z-stack images by selectively taking information from a certain surface. As most of our images came in this form, the Selective Projection algorithm has become our standard preprocessing routine for all types of analysis. Section 3.4 and 3.5 describe our most recent work in analyzing Müller glia bands and laser ablation experiments to investigate tension anisotropy. Together they suggest a new, more active role of Müller glia cells in epithelial patterning.

This work is done in close collaboration with Pamela Raymond (UM MCDB) and her lab, who did all the zebrafish experiments. Imaging data were taken by Mikiko Nagashima and Linda Barthel from Raymond lab. Parts of this work have been published in [80, 81].

3.1 Introduction: Cone Mosaic in Zebrafish Retina

Epithelial tissues are important biological building blocks from which more complex organs are sculpted [1–4]. They consist of cells packed together into 2D layers by forming apical junctions. These specialized junctions hold the epithelial cells together and give the tissue its mechanical integrity [6–9]. In vertebrates, the retina is an epithelial tissue that exhibits a high degree of organization within the epithelial plane [82]. Teleost fish retina has one of the most striking examples of this precise organization, where cone photoreceptor cells are arranged in a well-defined periodic pattern called the cone *mosaic* (Figure 3.1) [83–87]. This precise patterning involves both spatial alignment of cone cells into straight columns and correct specification of their spectral types [38, 80]. How biology does this, however, is not completely understood.

In this study, we focus on the retina of zebrafish *Danio rerio*. The retina is a thin, hemispherical epithelium that continues to grow along with the rest of the fish. The growth happens at the germinal zone located at the rim of the hemisphere (Figure 3.1 E). There, cone precursor cells proliferate and are periodically added into the mature retina mosaic [88–91]. Due to this mode of growth, new cells are added in concentric rings around the mature retina, thereby growing it radially. This also means that the oldest cells are located at the center of the retina, whereas progressively younger photoreceptors are found towards the germinal zone [38, 80, 85].

Of particular interest is the marginal zone, which is located at the transition between the germinal zone and the mature mosaic area. This is where most patterning is thought to occur. In this marginal zone, cone precursor cells are thought to have exited cell division but at the same time have not fully differentiated into mature photoreceptors. Interestingly, these precursor cells are packed somewhat randomly. This is in striking contrast to near crystalline packing of cones in the mature retina right next to them. The transition from disordered precursor into fully-ordered mosaic cones happens abruptly within several cell diameters long (Figure 3.1 D). Therefore, two things must happen during this transition: the precursor cones must (1) arrange themselves to the right spatial positions and (2) differentiate into the correct spectral subtypes, in order to match the mosaic pattern already established in the mature area [38, 80].

Most of our work is focused on the apical side of the epithelium where photoreceptor

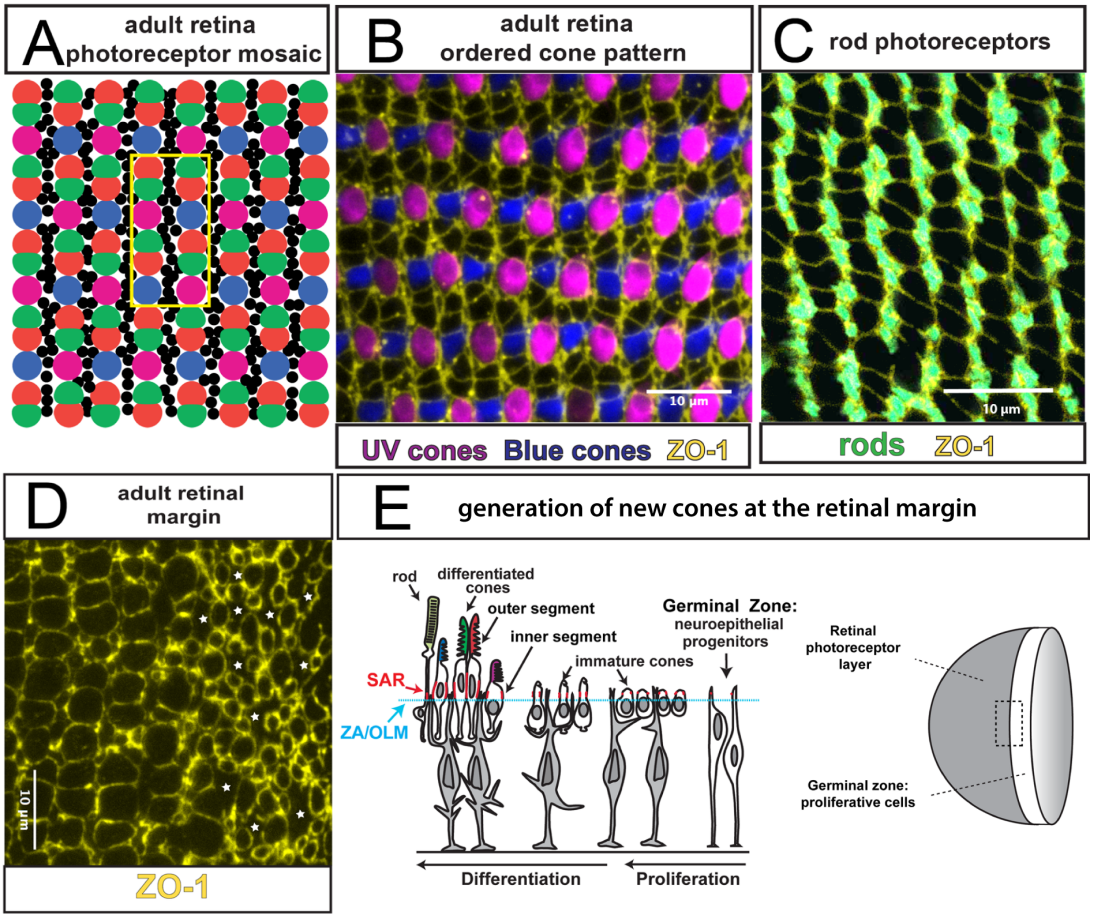

Figure 3.1: **Anatomy of zebrafish retina mosaic. (A-C)** Cone mosaic pattern is shown both in cartoon (A) and in actual retina sample (B) stained for UV and blue cones. Repeating unit lattice is shown in yellow box. Immunostaining against apical junctional protein Zonula Occludens-1 (ZO-1) is used to visualize cell profiles at the level of outer limiting membrane (OLM). (C) Rod photoreceptors insert between cone columns in mature retina. **(D-E)** Growth of retina mosaic. At the margin (D), randomly-packed immature cones can be seen next to mature cones ordered in columns. Periodically, these progenitor cells differentiate and assume columnar order, growing the retina at the rim of the hemisphere (E, right). Stars denote irregular shapes of Müller glia. Cartoon of retina cross-section (E, left) shows various cone and rod photoreceptors. Mosaic pattern can be seen at the OLM, where photoreceptor cells are tightly bound together forming zonula adherens (ZA). Figure adapted with permission from [38].

cells form a special type of epithelial apical junctions called Zonula Adherens (ZA in Figure 3.1 E). At this level, also known as the outer limiting membrane (OLM), cell profiles can be visualized using antibody against Zonula Occludens-1 (ZO-1), a type of scaffolding proteins that localizes at cell-cell junctions at the OLM. This is the level where the cone mosaic is observed (Figure 3.1). There are four subtypes of cone photoreceptors in zebrafish, classified based on the absorption peak of their color pigments: red, green, blue, and UV [92, 93]. Aside from the cones, there are two other cell types at the OLM: non-color-specific rod photoreceptors and neural Müller glia cells. Unlike cone photoreceptors, rod photoreceptors are known to be continuously added to the mature retina by inserting themselves in spaces between cone columns [80, 94, 95] (Figure 3.1 C). Müller glia cells are a type of neural glial that is present in the retina. They form thin lamellar processes apically that wrap around the photoreceptor cells at the OLM. Conventionally, Müller glia cell are thought to play passive, supporting role [96, 97]. However, later in Section 3.4 and 3.5 we show that these glial cells might play a more active role mechanically in establishing the mosaic pattern.

Despite knowledge of various players making up the epithelium, little is known about how they interact with each other and form the mosaic. Earlier work from our lab identified two mechanisms necessary in establishing the columnar order: (1) progressive addition of cone photoreceptors at the marginal zone as described above and (2) planar cell polarity (PCP) in cone cells that allows them to coordinate directions and modulate interface tensions [38]. They observed that the adhesion protein crumbs2b exhibits polarized concentration in all cone subtypes but UV, and they showed by numerical simulation that coupling between PCP and mechanical tension is sufficient in generating linearly-aligned column of cells from initial random packing. Consequently, they predicted that the epithelial tissue must be under anisotropic tension. More specifically, they hypothesized that tension of cell junctions oriented parallel to the columns must be higher than junctions oriented in the perpendicular direction.

A significant portion of our work was aimed towards testing these hypotheses. In the next section we analyzed retinas of *tbx2b* mutant fish that, despite loss of global mosaic organization, still show local patterns suggestive of PCP-mediated directional interaction. Section 3.4 addressed the presence of thick Müller glia bands parallel to the mosaic columns, which also extend to the unpatterned marginal zone. This suggests a role for the glial cells in maintaining tension anisotropy and patterning cone precursor cells. Finally, Section 3.5 analyzed experiments directly testing the stress anisotropy hypothesis by means of laser ablation. We showed that cells immediately surrounding the lesion relaxed non-uniformly upon ablation, implying that the retinal epithelium is under constant anisotropic

stress.

3.2 Analysis of *tbx2b* Mutant Column Fragments

In the quest for understanding the mechanism patterning cone cells into straight columns, we examined a mutant line *tbx2b*$^{-/-}$ where the cone mosaic pattern in adult retina is lost. Genetic disruption of transcription factor *tbx2b* eliminates most of UV cone photoreceptors and perturbs the long-range organization of the cone lattice normally seen in adult fish [80, 98]. In addition, *tbx2b* mutant retina exhibit a characteristic 'column fragments' appearance where cone cells form short linear chains reminiscent of wildtype columns but with no long range ordering, as shown in Figure 3.2.

There are a number of interesting questions one can seek to answer about the *tbx2b* mutant retina. The most obvious one is what are the factors that cause the loss of mosaic order (and therefore might play an important role in patterning the wildtype cones). In a recent paper [80], we showed by numerical simulation that loss of UV cones during formation of cone columns reproduces many features of the mutant retina.

However, here we focus on another quantitative analysis presented in [80] which shows that the remaining cone photoreceptors are preferentially attached to two other cone cells, giving the mature retina the column fragments appearance. This tendency to form 2-fold coordination with other cone cells supports the hypothesis that all but UV cone cells exhibit internal planar cell polarity (PCP) that helps them align to straight columns in wildtype fish [38]. This also suggests that, although global mosaic order is lost in *tbx2b* retinas, the PCP mechanism internal to the cone photoreceptors still remains largely intact and interactions between neighboring cone cells are still directional.

The following sections will describe in detail the analysis techniques used to quantify the coordination number of cone photoreceptors fragments in *tbx2b* mutant, from segmenting the z-projected images (Section 3.2.1), classification of segmented cells into cone and rod photoreceptors based on *rhodopsin* rod reporter intensity (Section 3.2.2), and grouping cone cells into column fragments based on some adjacency criteria (Section 3.2.3). To avoid over-dependency of the result on the adjacency criteria, we used two-threshold methods to establish upper and lower bounds of coordination numbers (Table 3.1), and showed that most cone cells are attached to two other cones regardless of the criteria used. This work has been published in [80].

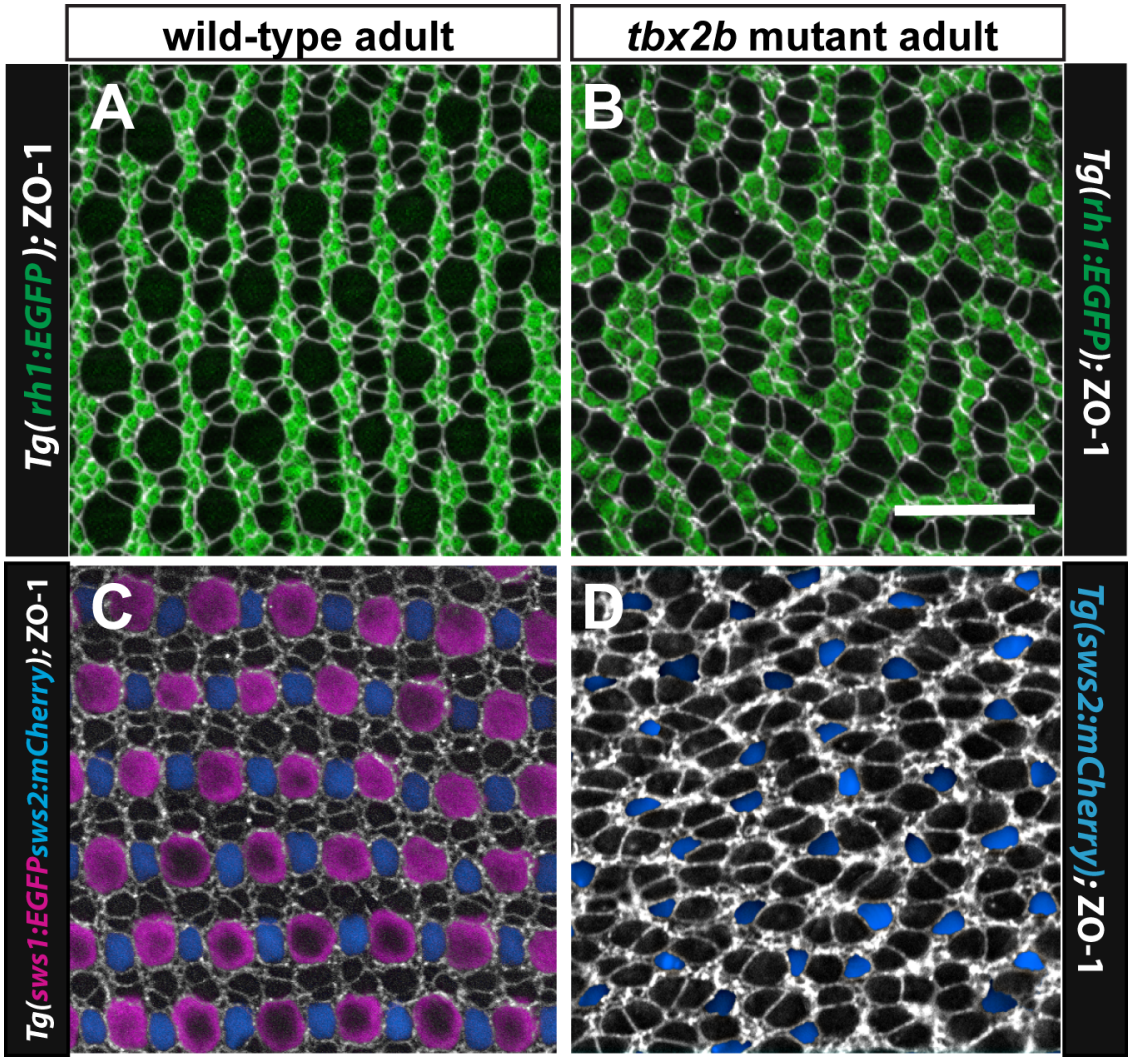

Figure 3.2: **Loss of cone photoreceptor columnar order in *tbx2b* mutant retina.** Comparison between mature wildtype **(A, C)** and *tbx2b*$^{-/-}$ mutant **(B, D)** retinas. Mutant retinas show characteristic loss of mosaic pattern seen in wildtype. Cell profiles at OLM are visualized by ZO-1 antibody staining (white). Transgene *rh1:EGFP*, *sws1:EGFP*, and *sws2:mCherry* mark rod, UV cone, and blue cone photoreceptors, respectively. Figure adapted from [80].

3.2.1 Thresholding-based cell segmentation

To quantitatively show that cone cells tend to have 2-fold coordination and form column fragments, we first need to segment the cone cells. Flat-mount transgenic *tg(rh1:EGFP)* retina samples were treated with ZO-1 antibody to visualize cell profiles at the OLM. Transgene *rhodopsin (rh1)* promoter driving expression of EGFP was used to visualize rod photoreceptors (see Figure 3.3 A-C). For this experiment, maximum intensity z-projection of the ZO-1 channel gave good enough result to be segmented by simple a edge-finding method:

```
M = imadjust(M);     % maximize contrast
M = wiener2(M);      % noise reduction with adaptive Wiener filter
if edgethr == 0;
    E = edge(M, 'canny');        % find edges with Canny method
else
    E = edge(M, 'canny', edgethr);
end
```

Listing 3.1: Code snippet from `FindEdges.m` (Appendix A.1.1).

MATLAB implementation of Canny edge detector [99] was used on the max-projected ZO-1 image. For thick enough ZO-1 profile, this method usually produces two lines for every ZO-1 line, corresponding to the rising and falling edges. To fill the gap between these two lines and get a continuous ZO-1 profile, the original image was thresholded and added to the edge detection result. Morphological closing was then used to smooth out the ZO-1 profile and fill remaining small holes/gaps. Partial cell profiles in contact with the image border were removed using the built-in function `imclearborder`. Segmented cell profiles were then defined as the remaining connected components, identified using built-in function `bwconncomp`. MATLAB code `FindEdges.m` is attached in full in Appendix A.1.1.

```
if graythr == 0;
    M1 = im2bw(M, graythresh(M));        % threshold
    graythresh(M)
else
    M1 = im2bw(M, graythr);
end
E1 = E | M1;         % add thresholded image to E to fill in holes
E2 = imclose(E1, strel('disk', strelsize));   % morphological closing
```

Listing 3.2: Code snippet from `FindEdges.m` (Appendix A.1.1).

3.2.2 Cell classification based on marker intensity

The resulting segmented image from the last section contains profiles belonging to both cone and rod photoreceptors (Figure 3.3 E). To exclude the rod cells, we use information

from EGFP channel driven by rod promoter *rh1*. Since EGFP is expressed in the entire rod cells (not localized at OLM), we picked the EGFP signal at the z-slice where most of ZO-1 signal surrounding the segmented cell is present. The projection is done with a MATLAB function `ProjectRodImages.m` given in Appendix A.1.2. Briefly, it identifies an area surrounding a segmented profile using morphological dilation with circular structuring element of size 5 pixels. The algorithm then tries to find the z-slice with the highest ZO-1 average intensity in this area, from which EGFP intensity in the segmented profile is take. This process is then repeated for all segmented profiles[1].

Figure 3.3 B-C shows the projected EGFP signal in each segmented cell profiles. The mean intensities of the profiles fall into a well-separated bimodal distribution (Figure 3.3 D) and thus can be used to classify profiles into cone (low intensity) or rod (high intensity) photoreceptors. We used `k-means` algorithm [100] to perform the classification and keep only cone profiles (Figure 3.3 F). Remaining cell profiles with area less than 25 pxiels (likely to be Müller glial profiles) and larger than 100 pixels (mostly segmentation error) were excluded. MATLAB code is given in Appendix A.1.3.

3.2.3 Two-threshold adjacency determination

Once we have the cone profiles segmented out, we want to join together nearby cones into column fragments. To efficiently identify neighboring profiles, we use morphological dilation to enlarge all cone profiles, and pairs that overlap were deemed neighbors. The amount of dilation is set by the structuring element used in performing the morphological operation, chosen to be a circle of radius 10 pixels. On the images we analyzed, we found that the said radius is sufficient to make any reasonably-close pairs to overlap[2]. This serves as a good starting point for a more refined criteria presented next. MATLAB code for the dilation-based neighbor determination is given in Appendix A.1.4.

The above definition of closeness based on the presence of overlap after dilation is very loose and includes pairs that one might not call adjacent based on the morphology. To refine the adjacency determination, we use more sophisticated criteria taking into account the known morphology of cell-cell interfaces. Adjacent cones within a column in wildtype retinas are not only closely-separated but also tend to share a length of common interface. Said

[1] More sophisticated Selective Projection algorithm described in Section 3.3, which were developed after this analysis, could also be used. However, given the good quality of the images from this experiment, we expect only marginal improvements at best. Many subsequent experiments, however, would not be suitable for this simple projection method (due to less-than-ideal image quality, difficult/impractical to segment, etc.) and motivated the development of Selective Projection method.

[2] Similar result can be achieved by simply calculating distances between profiles and finding pairs within some short distance from each other. However, for large number of segmented profiles, morphological dilation approach used here is computationally faster.

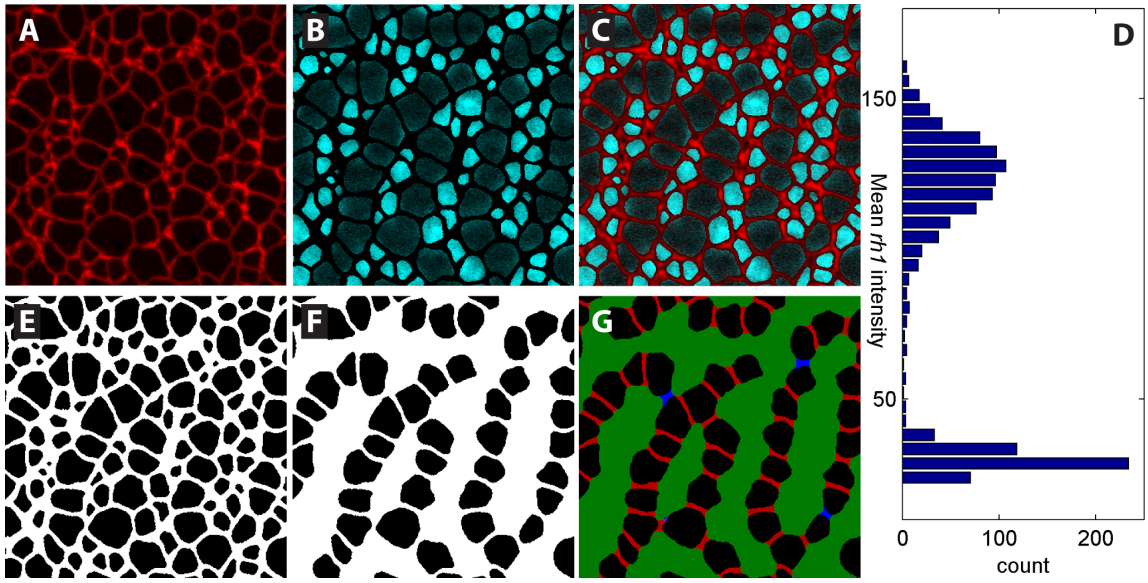

Figure 3.3: **Analysis of *tbx2b* mutant column fragments. (A-C)** *tbx2b* mutant retina imaged with ZO-1 antibody staining (red) showing cell outlines and rod marker *rh1:EGFP* (cyan). Maximum intensity projection of ZO-1 antibody is shown in (A, C). EGFP intensity in (B, C) is taken from the slice that has strongest ZO-1 signal surrounding the cell (see text). (D) Histogram of mean EGFP intensity in each cell showing clear separation between rod and cone cells. Cell segmentation from thresholding ZO-1 showing both rod and cone cells (E), and with rods removed (F) based on EGFP intensity showing cone column fragments. (G) Result of two-threshold adjacency determination on cone fragments. Red interfaces satisfy both strict and loose criteria, while blue interfaces only satisfy the latter (see text for details).

in another way, we expect to see thin and long interface with high ZO-1 intensity between two cells that are adjacent. Closely-separated but otherwise non-adjacent cones typically have this space filled by rod photoreceptors or thicker bands of Müller glia processes.

Transforming this observation into more precise criteria, we therefore set numerical limits on the thickness and aspect ratio of the interfacial regions of two nearby cells, defined as the overlap region computed in the previous section[3]. Neighboring pairs that do not satisfy these criteria are deemed to be non-adjacent. To avoid over dependency of the result on these criteria, we used two-threshold method where we devised two sets of thickness and aspect ratio parameters. The first set is designed to be less stringent, allowing most adjacent cones to be classified correctly but might include some non-adjacent ones. At the end of the spectrum, the second, more stringent set is designed to reject most non-adjacent pairs at the risk of excluding small number of adjacent ones. For the images we analyzed, we found that minimum thickness of 10 pixels and minimum aspect ratio of 2 work well as the less-stringent threshold. For the more stringent one, we kept the same minimum thickness and increased the aspect ratio to 2. MATLAB code is given in Appendix A.1.5.

Figure 3.3G and Figure 3.4 show the result of the two-threshold adjacency determination. Interfaces that satisfy both the loose and stringent criteria are colored red, while those that only satisfy the latter are colored blue. The red interfaces clearly join cells into column fragments. The blue interfaces, on the other hand, frequently give somewhat ambiguous interfaces where it is not clear whether the two cells flanking it are adjacent or not. This, however, provides us with good upper- and lower-bound coordination numbers.

3.2.4 Results: Most *tbx2b* mutant cones are 2-fold coordinated

Once we have determined the adjacency criteria, it is trivial to count the coordination number of each cone, defined as the number of other cones it is adjacent to. Figure 3.3 shows a representative sample of ventral-nasal (VN) region of a mutant retina. The histogram in panel C does not look very different for both low (loose) and high (stringent) set of criteria, confirming that the qualitative feature of coordination number n is insensitive to the details of the analysis.

We analyzed in total of 11 mutant retinas at varying locations, and the result is tabulated in Table 3.1. In almost all of the sample analyzed, the majority of the cones are two-fold coordinated, i.e. adjacent to two other cones. Although *tbx2b* retinas lost the long-range cone crystalline pattern, lack of 3-fold coordination or higher shows that the cones are

[3]To define thickness and aspect ratio, we first calculated moment of inertia of the interfacial region. Then its aspect ratio is defined as the ratio of the two principal moments, and its thickness as the smaller principal moment.

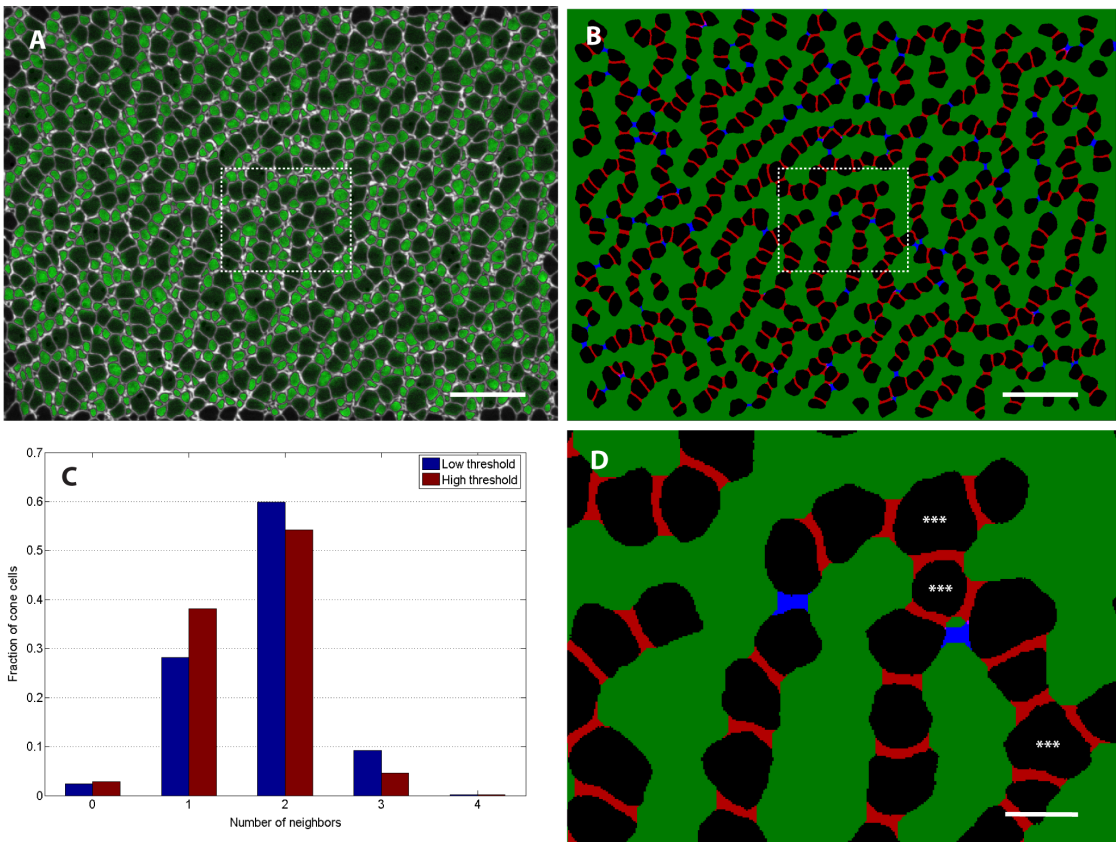

Figure 3.4: **Infrequent 3-fold coordination of *tbx2b* mutant retina cone photoreceptors suggests strongly directional interaction.** (A) Ventral-nasal (VN) region of mutant retina marked for ZO-1 antibody (white) and EGFP (green) driven by *rh1* rod promoter. (B) Result of segmentation and adjacency analysis on cone cells of (A). Cone profiles are shown in black. Red interfaces satisfy both strict and loose adjacency criteria, while blue interfaces satisfy only the latter. (C) Histogram of cone coordination numbers for low (blue bars) and high (red bars) thresholds showing most cones are 1- and 2-fold coordinated. Result remains qualitatively the same for low and high threshold. (D) Zoom around the indicated area, showing 3-fold coordinated cells (triple asterisks). Lack of 3- or higher-fold coordination suggest that cone cells are interacting in highly-directional manner, despite the lack of long range mosaic order in Tbx2b retinas. Scale bars are 2 μm for A & B and 4 μm for D. Figure adapted from [80].

Table 3.1: Most cones are 2-fold coordinated in adult *tbx2b* mutant retinas. D = dorsal, N = nasal, T = temporal, V = ventral. Table adapted from [80].

Sample	Region	# of cones	% n-fold coordination (low/high threshold)				
			$n = 0$	$n = 1$	n =2	$n = 3$	$n = 4$
1	D	683	31.0 / 43	**51 / 47**	17 / 9.2	0.9 / 0.3	0.1 / 0.0
2	N	493	2.6 / 3.0	34 / 39	**57 / 53**	6.3 / 5.1	0.0 / 0.0
3	T	865	7.1 / 14	37 / **47**	**46** / 35	9.7 / 3.7	0.3 / 0.3
4	VN	454	2.4 / 2.9	28 / 38	**60 / 55**	8.8 / 4.2	0.2 / 0.2
5	VN	677	1.5 / 2.1	22 / 28	**51 / 51**	24 / 18	0.6 / 0.6
6	VN	644	1.9 / 3.1	29 / 33	**62 / 59**	6.7 / 4.7	0.0 / 0.0
7	VN	765	5.9 / 7.6	**52 / 56**	38 / 34	4.7 / 2.7	0.1 / 0.0
8	VT	659	1.8 / 2.3	25 / 31	**51 / 52**	22 / 14	0.9 / 0.5
9	VT	840	1.5 / 4.2	19 / 26	**53 / 54**	26 / 16	1.3 / 0.7
10	VT	746	1.2 / 1.7	16 / 21	**52 / 53**	30 / 24	1.1 / 0.4
11	VT	932	1.7 / 2.1	22 / 31	**52 / 49**	22 / 17	2.5 / 1.1

not packed randomly either. Instead, they preferentially form short chains, reminiscent of wildtype columns, that are relatively straight in the short length-scale. This suggest that the PCP mechanism that is responsible for aligning them to columns [38] are not completely lost, and that the cone cells still exhibit highly-directional interaction seen in wildtype.

Parameters used for the analysis are as follow: for the first, looser criteria, we require a maximum thickness of 10 pixels and a minimum aspect ratio of 2. For the second, more stringent criteria, these numbers are 10 pixels and 2.5, respectively. This work has been published in [80]. Interested readers are referred to the published paper for more biological context and relevance.

3.3 Selective Projection of z-stack images

Most of the images we analyzed are z-stack images captured by either confocal or two-photon fluorescence microscopes. These microscopes have good optical-sectioning capability, meaning that they will only collect photons from a thin volumetric slice of the sample centered at the plane of focus. As a result, one can obtain pseudo-3D images by repeatedly capturing 2D images at different z-depths. The resulting stack of 2D images is called a z-stack image (see Figure 3.5 A-E for some examples).

Although having 3D information can be useful, frequently the object of interest for quantitative analysis is some thin surface captured in the z-stack[4]. For example, in looking at the mosaic pattern of zebrafish retinal epithelium we are mostly interested in the outer limiting membrane (OLM) of the tissue, where photoreceptor and glial cells are tightly-bound together forming the zonula adherens (ZA). The antibody against ZO-1 localizes well at this level, and could be used as a marker to identify the OLM surface.

To project ZO-1 intensity z-stack into a 2D image, traditional methods include simple projections such as the maximum-intensity projection. In max-projection, the value of a pixel in the 2D projected image is simply the maximum across the entire depth of the z-stack. This method (and other similar variations such as mean-, median-projection, etc) has one big shortcoming, however, as it only works for fluorescent proteins that are localized at the surface of interest (e.g. ZO-1 which localizes only at at intercellular contacts at the ZA/OLM). Often we are interested in looking at some fluorescent marker that is present throughout the depth of the epithelia (such as the *gfap:EGFP* transgene that marks entire Müller glia cell, see section 3.5) at the OLM level. In this case, people traditionally resort to masking intensities by hand, leaving only those at the OLM level – a laborious and often imprecise method.

To achieve more accurate and reproducible projections, we developed a MATLAB program that can automatically identify the surface of interest and create a projection by selecting intensities only from that surface. Given a marker like ZO-1 that localizes to some surface, the program can reconstruct the depth-profile of that surface and automatically select intensities of a second, non-localized fluorescent marker only from that surface. Not only that, this method can also be used on the localized marker itself to produce a much higher quality projection than traditional max-project allows. Since it can reject intensities away from the surface, the resulting projection usually has a much higher contrast and less 'ghosting' from bright, out-of-focus objects (Figure 3.5). The quality of the projection

[4]Pseudo-3D capture at different z-depths is still needed here since often we cannot precisely align the surface of interest to perfectly coincide with the focal plane. Hence one usually captures z-stack images around the surface, then 'flatten' the z-stack using some projection technique post-acquisition.

compares favorably to the result obtained by careful masking of images by hand, but higher reproducibility and much less labor and user bias.

In the next section we will first discuss the core algorithm to do the projection. Section 3.3.2 discusses several pre- and post-processing subroutines that was employed. The order which these subroutines were applied are given in the code in Appendix A.2. Note that this ordering was determined empirically. One might want to add or remove certain pre- or post-processing subroutines depending on the image to be analyzed. The main MATLAB code `Estimate_OLM_From_ZO.m` (Appendix A.2.1) provides switches to easily turn on and off different subroutines. Default parameters for these subroutines are given in the code as well.

3.3.1 Core Algorithms

The method relies on the assumption that, for properly selected pixels, the intensity profiles versus z-depth should have a strong peak located on the surface of interest. (How to select such pixels will be addressed in the next section). This is true for all the ZO-1 antibody markers we analyzed (and to some extent, *gfap*:EGFP markers marking Müller glia), where it produces sharp image of cell outlines at the level of the OLM. Away from the OLM, the ZO-1 intensity quickly fades away into some background intensity, thanks to the good sectioning ability of confocal and 2-photon microscopes. Hence, given this 'properly-selected' pixels, one should be able to estimate the location of the OLM from peaks of the intensity vs. z-depth profiles.

3.3.1.1 Max-projection and Entropy Filtering

For a pixel to have intensity profile as described above, it must have a meaningful intensity at the OLM. In the case of the ZO-1 marker, this means we want to select the pixels at and between cell boundaries (Figure 3.5 A'-E', ZO-1/red channel). If one were to select pixels on the background or inside a cell, it is not hard to see that the intensity profile will not have the desired peak. Hence we use as a starting point max-projection of heavily-smoothened ZO-1 (Figure 3.5 F):

```
% Apply wiener2 eliminate noise before max projection
if p{3,2} == 1
    disp('Pre-process: wiener filter...')
    ZOblur = zeros(size(ZO));
    for i = 1:nStack
        ZOblur(:,:,i) = wiener2(ZO(:,:,i), [p{4,2} p{4,2}]);
    end
else    ZOblur = ZO;
end
```

```
% Maximum projection
ZOmax = double(max(ZOblur,[],3));
ZOmax = ZOmax - min(min(ZOmax));
ZOmax = ZOmax ./ max(max(ZOmax));
```

Listing 3.3: Code snippet from `Estimate_OLM_From_ZO.m` (Appendix A.2.1).

The smoothing is done here using `wiener2` adaptive noise filter [101], but in principle could be done with Gaussian or any other filter. Its purpose is to suppress noise/bright pixels that might not correspond to the OLM, and hence heavy filtering is preferred here. The resulting image is shown in Figure 3.5 F. The max-projection can then be thresholded very conservatively to get the desired pixels, shown in Figure 3.5 H.

In some cases, part of the field-of-view (FOV) contains background with no object. We also have to exclude the background region from analysis. This can be done with a class of texture filtering, whose response depends on the presence of certain texture in the image. In our case, we used entropy filter `entropyfilt` which essentially calculates the entropy $S = p\log(p)$ of intensity histogram in a moving window [99]. Hence, the output of the filter will be small in regions with no detail, and large in areas with lots of pixel intensity variation. This texture filtering is done on a separate sub-function `Separate_ROI_from_background.m` that contains other preprocessing steps to improve the background-object separation. Figure 3.5 G shows the output of the entropy filtering.

```
%% 4. Texture filter
% Currently entropy filter is used. It works fine but a little bit
    slower.
% Alternatively it can be replaced with e.g. stdfilt or other texture
% filtering.

t = entropyfilt(M, ones(entropyFilterSize));
% normalize to [0,1]
t = t - min(min(t));
t = t ./ max(max(t));
```

Listing 3.4: Code snippet from `Separate_ROI_from_background.m` (Appendix A.2.2).

We also note that, while doing the job very well, the entropy filter is also slow to run. For very large images (much larger than 1024×1024) one might want to decrease the filter size, or replace it altogether with faster texture filters such as `stdfilt` [99].

3.3.1.2 Finding peaks on intensity profile

Once we have successfully separated the background out and selected the candidate pixels, we want to find peaks in their intensity profiles vs. z. The locations of the peaks give the

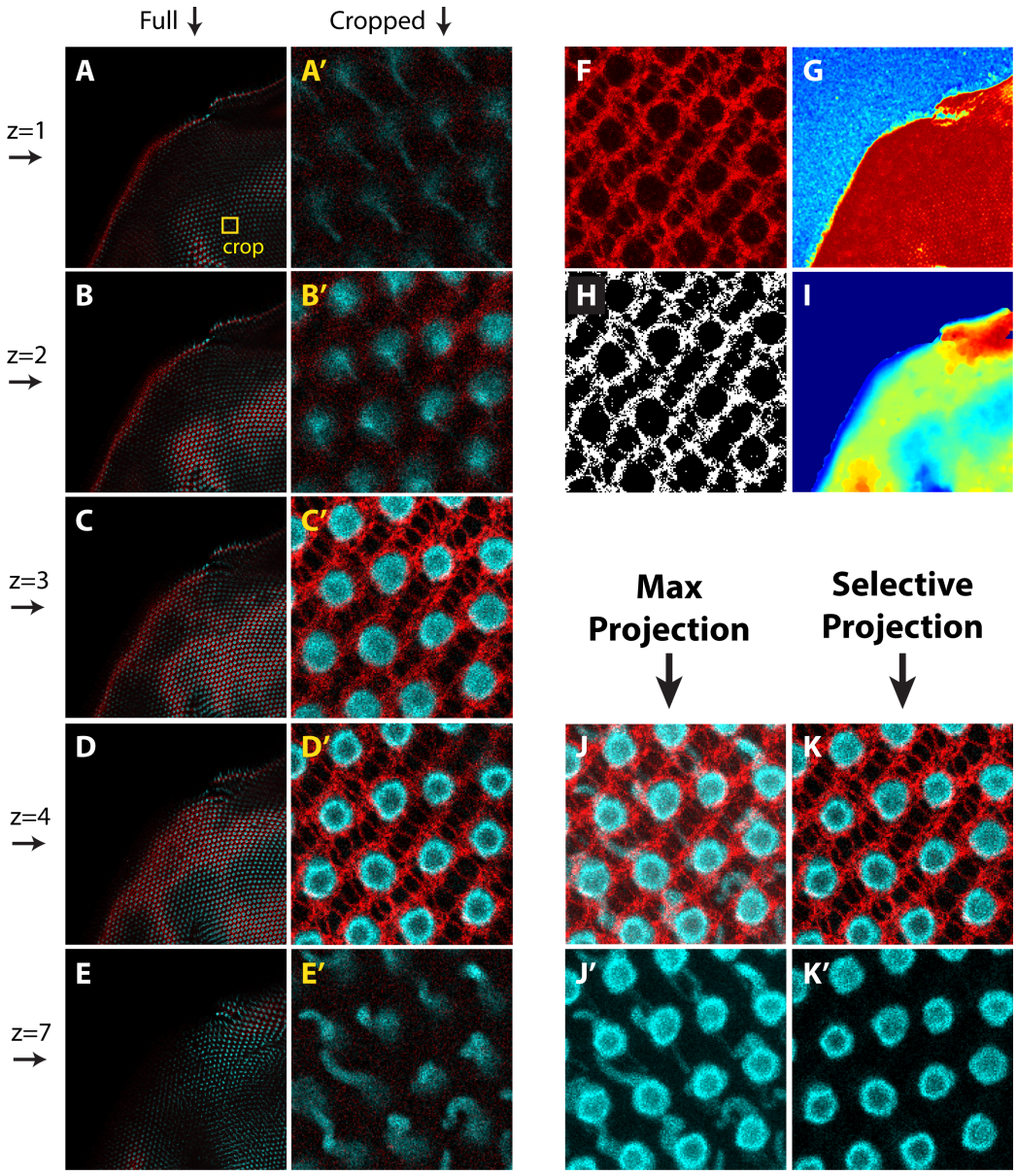

Figure 3.5: **Selective projection of z-stack images: example and methods. (A-E')** Full and zoomed views of z-stack images of zebrafish retina. Antibody for junctional protein ZO-1 (red) localizes to a thin surface at the OLM, while EGFP (cyan) driven by UV cone opsin promoter *sws1* is expressed broadly throughout the apical region. **(F-I)** Steps of selective projection algorithm. (F) Zoomed view of max-projection of ZO-1 with high smoothing for detecting the OLM surface. (G) Full view heat map of texture filtering applied on (F) shows clear separation between retina and background. (H) Thresholding (F) gives candidate pixels whose intensity profiles are used to estimate the depth of OLM surface. (I) inferred depth profile of the OLM surface used for projection. **(J-K')** Comparison between traditional max-projection and Selective Projection. Note how Selective Projection produces much higher contrast and eliminate 'shadows' of objects away from the OLM surface. (K') Selective Projection of *sws1*-driven EGFP at the level of OLM (indicated by ZO-1).

depth of the surface at different locations. This depth information can then be interpolated to construct the estimated depth profile of the entire surface. The interpolation is done by averaging over 100×100 pixels neighborhood, weighted by Gaussian of standard deviation 10 pixels. Figure 3.6 (left) shows typical $(> 80\%)$ intensity profiles of the candidate pixels, where each one exhibits a single prominent peak. To achieve higher accuracy, we fit the peaks with Gaussians and locate the maxima.

A small fraction $(< 20\%)$ of the profiles will exhibit irregular shapes shown in Figure 3.6 (right) that do not lend easy estimation of the OLM. Some common causes for bad profiles are: (1) exhibiting two or more peaks with comparable intensity (either due to presence of strong speckle/noise or weak intensity at the OLM level), or (2) having broad and low peaks. These bad profiles can be identified by some simple criteria, such as the standard deviation/width of the fitted Gaussian, ratio between highest and second highest peaks, etc. They are then excluded from analysis.

Once the peak location of all the 'good' intensity profiles are found, they are interpolated to the entire surface. This interpolation is necessary to cover regions without significant ZO-1 intensity, such as the interior of cells, as well as for pixels excluded above. Gradient-based speckle detection can also be done here to detect large jumps in depths, usually caused by bright noise or objects away from the OLM. Projection of any marker (including the marker used to estimate the surface) can then be done by picking intensities only at z-position specified by the estimated surface profile[5].

The full code is attached in Appendix A.2. Other than the main algorithm described above, the code also contains some other pre- and post-processing routines, some of which are described below. The order in which different routines are employed are given in the code in Appendix A.2.

3.3.2 Misc: Pre- and Post-Processing Routines

In most image analysis tasks, employing appropriate pre- and post-processing techniques can improve the output of the analysis significantly, sometimes even more than tweaking/switching the core algorithm. Here we discuss several of these techniques. Most of them are either available as a built-in MATLAB functions or a simple combination of them. Some techniques however are not available readily in MATLAB, and we relied on external programs such as ImageJ/Fiji.

[5] An option to project by taking Gaussian-weighted average of several slices around the maximum is available in the code. Practically, however, we found that rounding the depth to the nearest integer and taking intensities only from that slice produces sharper image in many cases we encountered. This is true especially when the step-size between subsequent z-slices is small enough such that features stay in focus in two or more slices.

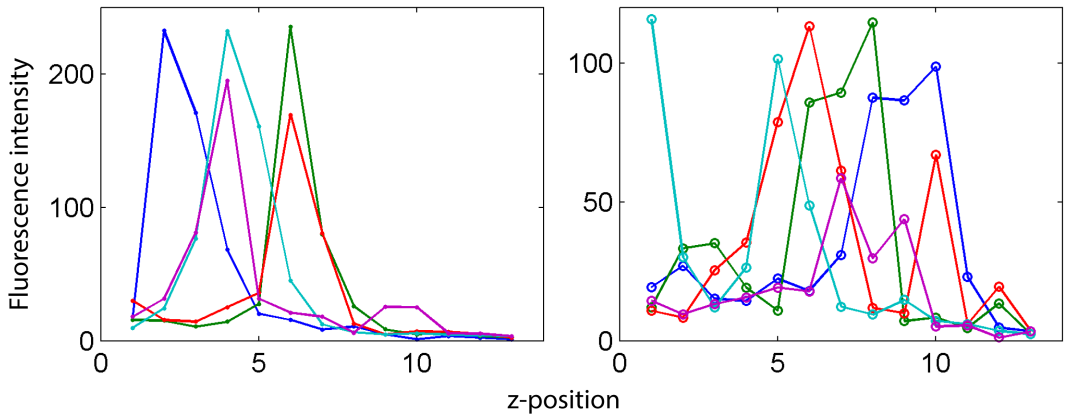

Figure 3.6: **Selective Projection of z-stack images: intensity profiles.** Representative samples of intensity profiles showing good (left) profiles that were used for OLM estimation, and bad (right) profiles that were discarded. Profiles without clear and well-defined peaks were classified bad and excluded from analysis. This can be due to: presence of multiple/ambiguous peaks, broad or irregular profiles, etc. Note how smoothened max-projection and texture filtering (step F-H in Figure 3.5) selects only pixels with significant intensity peak at OLM. As a result, most $(> 80\%)$ of the intensity profiles analyzed fall into the good category.

3.3.2.1 Noise reduction

This is arguably the single most important pre-processing technique. It usually involves trade-off between effectiveness and reduction in image resolution/sharpness. Most of the time, we use MATLAB's built-in adaptive noise filtering `wiener2`, which adapts the strength of the denoising to the statistics of the surrounding region. In areas with large intensity variance, the filter performs little smoothing. On the other hand where the variance is low, `wiener2` performs more aggressive smoothing. This achieves superior noise suppression in flat areas while at the same time does a good job in maintaining edge sharpness [99].

In almost all cases we encountered, we found `wiener2` to perform equally or better than Gaussian blur, while taking negligible extra computation time.

3.3.2.2 Background compensation

Images sometimes can have light fall-off, due to either uncorrected optical vignetting (where edges and corners of an image tend to be darker due to uncorrected objectives) or fluorescence bleaching. An example of the latter is when scanning multiple tiles with overlap for stitching. The overlap regions, necessary for aligning adjacent images before

stitching, are inevitably scanned twice and thus tend to be less bright due to optical bleaching. This can be corrected by estimating and correcting for overall signal intensity when close to uniform illumination is desired (e.g. when stitching multiple images to produce a single image with much larger field of view).

To correct for uneven illumination, we first have to estimate how this illumination varies spatially. A common way to do this is to measure how background intensities vary over the image. This relies on the assumption that any unevenness or fall-off in illumination affects both the signal and the background. To get the latter, we applied morphological closing with large structuring element to the image (see [99, 102] for good reviews on morphological operations). This will pick minimum intensity in a large area defined by the structuring element, and the spatial profile of this intensity can be used to non-uniformly scale the original image to correct for spatial intensity variation [99].

Note that a possibly undesired side effect of this is that it will increase noise intensity in the areas with significantly lower illumination. For applications where noise intensity is crucial (e.g. edge detection, segmentation, etc.) one might want to apply noise reduction to these areas before and/or after the illumination correction, or even skip it altogether.

```
% Background compensation
bgm = imclose(ZOmax, strel('disk', p{7,2}));
scale = max(max(bgm)) ./ bgm;
scale(isinf(scale)) = 1;    % background was set to Inf
scale(~bgmMask) = 0;
if p{6,2} == 1
    disp('Pre-process: background compensation...');
    ZOmax = ZOmax .* scale;
end
ZOmax(~bgmMask) = 0;
```

Listing 3.5: Code snippet from `Estimate_OLM_From_ZO.m` (Appendix A.2.1).

3.3.2.3 Contrast enhancement

Contrast enhancement can help improve analysis by maximizing the use of available dynamic range (i.e. all the 256 values in 8-bit, or 2^{16} values in 16-bit images, etc). The simplest method is just to scale the pixel intensities to fit the dynamic range. Although easy, this is sometimes not enough since it scales the entire image uniformly, potentially leaving some regions still low in contrast [99]. A more advanced contrast-limited adaptive histogram equalization (CLAHE) method is available in MATLAB as `adapthisteq` (see also similar non-adaptive variation `histeq`). It works locally in tiles and transforms the intensity histogram to match certain distribution (usually uniform, but other distributions can be equally used) [103]. Note that enhancing contrast necessarily makes noise

more prominent, so one might want to experiment interleaving this with noise reduction routines.

```
154 % CLAHE
    if p{8,2} == 1
156     disp('Pre-process: CLAHE...');
        nTiles = floor( size(ZOmax) ./ p{9,2} );
158     ZOmax = adapthisteq(ZOmax, 'NumTiles', nTiles);
    end
160 ZOmax(~bgmMask) = 0;
```

Listing 3.6: Code snippet from `Estimate_OLM_From_ZO.m` (Appendix A.2.1).

3.3.3 Conclusion

The Selective Projection algorithm is very useful and has become our default approach in projecting z-stack images. It produces higher quality projections of markers localized to a specific z-level than it is possible with traditional, non-selective methods. When used in conjunction with non-localized markers, it enables selecting intensity only at the level of the localized marker (or, with slight modification, a fixed distance from it).

The algorithm has been used in our published and unpublished analyses of various fluorescent markers, in conjunction with the ZO-1 OLM marker, such as: expression of non-localized reporter of rod photoreceptors *rh1:EGFP* (published in [80]), expression of non-localized reporter *trβ2:tdTomato* marking red cones and several non-photoreceptor cells (unpublished), and *sws1:EGFP* promoter specific to UV cones (unpublished). Recently we have also successfully applied the method to project non-localized marker of Müller glial cells *gfap:EGFP* on its own without any localized marker. The *gfap:EGFP* marker has ZO-like localization at the OLM, but forms stalk-like processes above and below OLM. In this case, very rough masking of the processes away from OLM helped the algorithm to lock into the ZO-like pattern of *gfap:EGFP* expression at OLM[6]. Without it, one would need to do very careful masking to achieve the same result.

MATLAB code for Selective Projection and various auxiliary routines described above are included in Appendix A.2.

[6]The rough masking was done by painting black parts of the images clearly far from OLM, based on morphology. One could do it equally well in Adobe Photoshop or any other image manipulation software.

3.4 Ridge Analysis of Müller Glia Bands

To elucidate the mechanisms leading to the ordered photoreceptor packing in mature retina, we look for hints at the marginal region of the retina where growth takes place. Located at the periphery of the mature retina, this marginal zone is characterized by the presence of disordered cone precursor cells [88–91]. These precursor cells are thought to have not yet fully differentiated to specific spectral types, but otherwise are known to have exited proliferation cycle (i.e., no longer dividing). Unlike mature cones that form near crystalline order, these progenitor cells clearly lack the spatial ordering seen in mature retina. As the retina grows, precursor cells periodically differentiate into mature cones with the correct spectral types and align themselves spatially to match the pattern already defined in the mature area. Here we look at the role of another type of cells called Müller glia in helping the cone cells form linear columns.

Müller glia is a type of neural glia cell that is present in the retina. Classically thought to give support to other cells, they form lamellar processes that wrap around photoreceptor cells apically [96, 97]. However, we found that the thickness of these processes at the OLM varies depending on the direction along the plane of epithelium. Along the direction of the column of the mature retina, Müller glia processes form thick 'bands' that separate one column from the next. In contrast Müller glia form relatively thin layers between two cones in the same column. (see Figure 3.7).

We report that the thick Müller glia bands normally associated with the mature retina extend into the marginal zone where columnar ordering is not yet established. Therefore we hypothesize that Müller glia cells might play a role in guiding the precursor cells into straight columns as they mature and join the mosaic pattern. A related hypothesis that Müller glia cells help bear tension, based on the observation that the thickness of the bands is correlated with the expected tissue stress anisotropy, is tested by performing and analyzing laser ablation experiments, presented in Section 3.5 and in [81].

In this section we describe in more detail the image analysis technique to show in an unbiased way that the glial cells indeed form thick bands at the margin along the direction corresponding to column orientation in the mature area. Both the works presented in this section and in Section 3.5 are included in our most recent manuscript, currently in consideration for publication at Nature Communications and is attached in Appendix C. Interested readers are invited to read the full manuscript for more biological context.

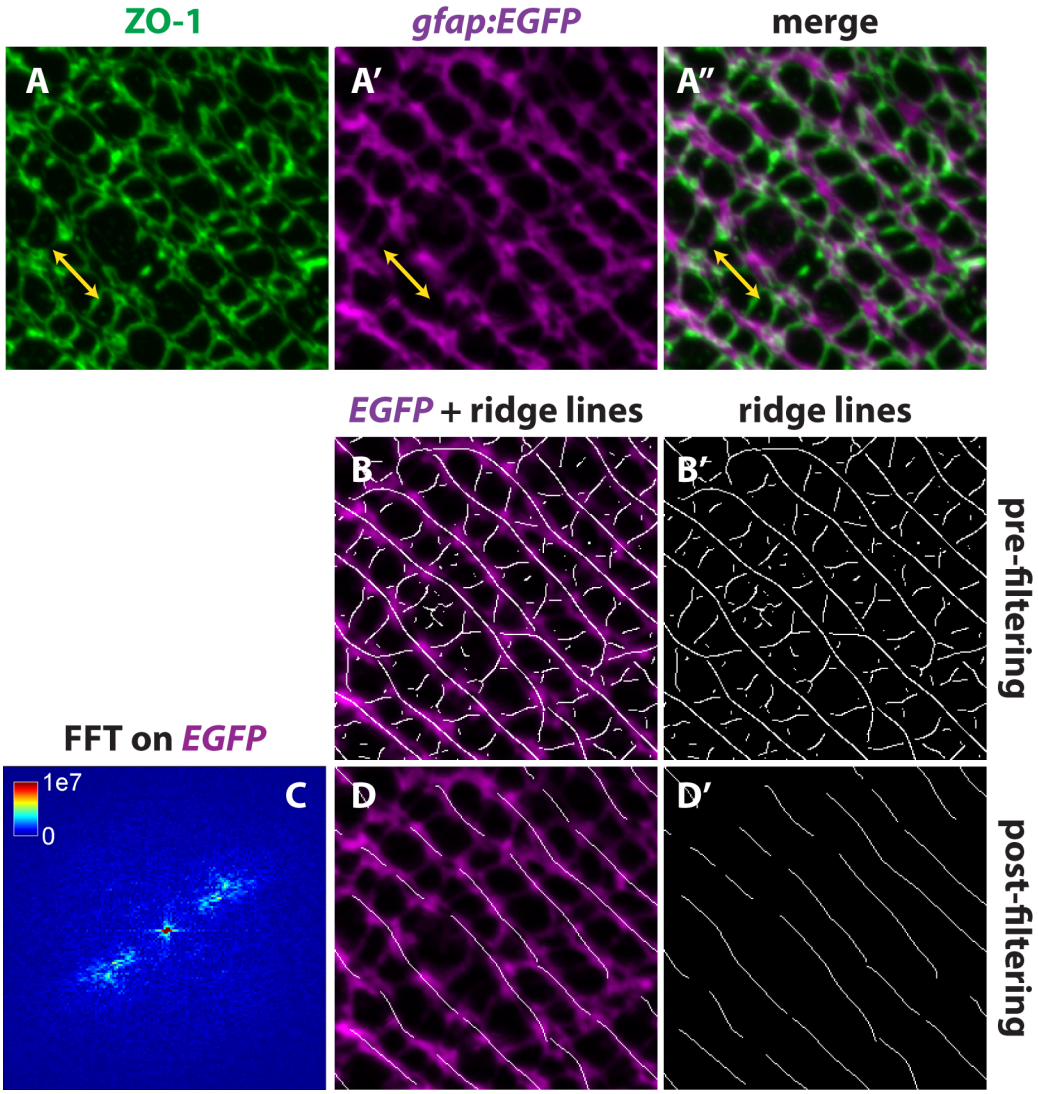

Figure 3.7: **Detection of thick inter-column Müller ridges.** Mature retina showing columns of cone photoreceptor with ZO-1 antibody staining (A) showing cell profiles and *gfap:EGFP* transgene (A') marking Müller glia cells at the OLM. Note how the latter form thick bands between adjacent columns (A'-A"). Column direction is indicated by yellow arrows. Ridges of *gfap:EGFP* as detected by 4th order ridge filter described in the text (after non-maximum suppression, B-B'). Thick intercolumn bands produce long continuous lines, while thin within column lamellae tend to produce short and perpendicular lines. FFT on *gfap* picks up the direction of the columns (C). Selecting only lines parallel to the column (and eliminating short line fragments, see text for details) produces cleaner ridge lines that now correspond only to the thick inter-column bands, as desired (D-D'). In (A-A", B, D) Selective Projection algorithm (Section 3.3) was used to project EGFP signal at the level of OLM as indicated by ZO-1.

3.4.1 Steerable ridge filter

Optical section z-stack images were obtained from the margins of flat-mounted retinas of transgeninc fish *tg(gfap:EGFP)* as described in [81]. Transgene for glial fibrillary acidic protein *gfap*, a Müller glia-specific promoter, was used to identify the said glial cells. Antibody against ZO-1 was used to visualize cell profiles at the level of the OLM. Since *gfap:EGFP* is expressed throughout the glial cells from apical to basal, we used the Selective Projection method described in Section 3.3 in conjunction with the ZO-1 antibody to project the EGFP signal at the level of the OLM. As expected, Müller glia cells in mature retina form thick bands running along and between two adjacent columns (see Figure 3.7).

The between-column bands have some characteristic thickness that is roughly equal to the gap between adjacent columns, and is significantly different than the thickness of lamellar processes between cones in the same column. Hence we can use ridge filter of certain thickness and orientation to detect and isolate only the thick bands. Here we used a steerable version of such filter described in [104].

A steerable filter is defined as an orientation-specific filter that can be expressed as a linear combination of a small set of base filters. The advantage of using a steerable filter is mostly computational: it allows efficient computation of the same filter rotated through many different angles. Since any rotation of the filter can be expressed as a linear combination of the base filters, one only need to compute convolutions with the base filters. If a non-steerable filter was used, one would then need to have many copies of the same filter rotated at discrete angles and apply all of them to the image.

A publicly-available ImageJ implementation of the steerable filter by the same authors [104] was used. Briefly, it takes as input a gray scale image and returns two numbers at every pixel: (1) angle orientation of the filter that best fit the image in the region surrounding that pixel and (2) the response/magnitude of that optimal filter. We used 4th order ridge detector [104] and found that a width of 10 pixels worked best in discriminating the thick, between-column bands from thin, within-column lamellae. (We will later change the width slightly to 8 pixels when analyzing the marginal zone, as the bands are slightly thinner there). Non-maximum suppression (available as 'Refine feature' function in the plug-in) was used on the magnitude of the output to obtain single pixel wide lines along the center of the ridges. This is a common edge thinning technique that works by suppressing all pixels except those that are local maxima along the perpendicular direction of the ridges [99, 102].

As expected, the above series of operations produce mostly long, continuous lines along the thick inter-column bands (see Figure 3.7 B-B'). Thin within-column lamellae are sometimes detected, but they tend to be much shorter in length and oriented perpendicular to the

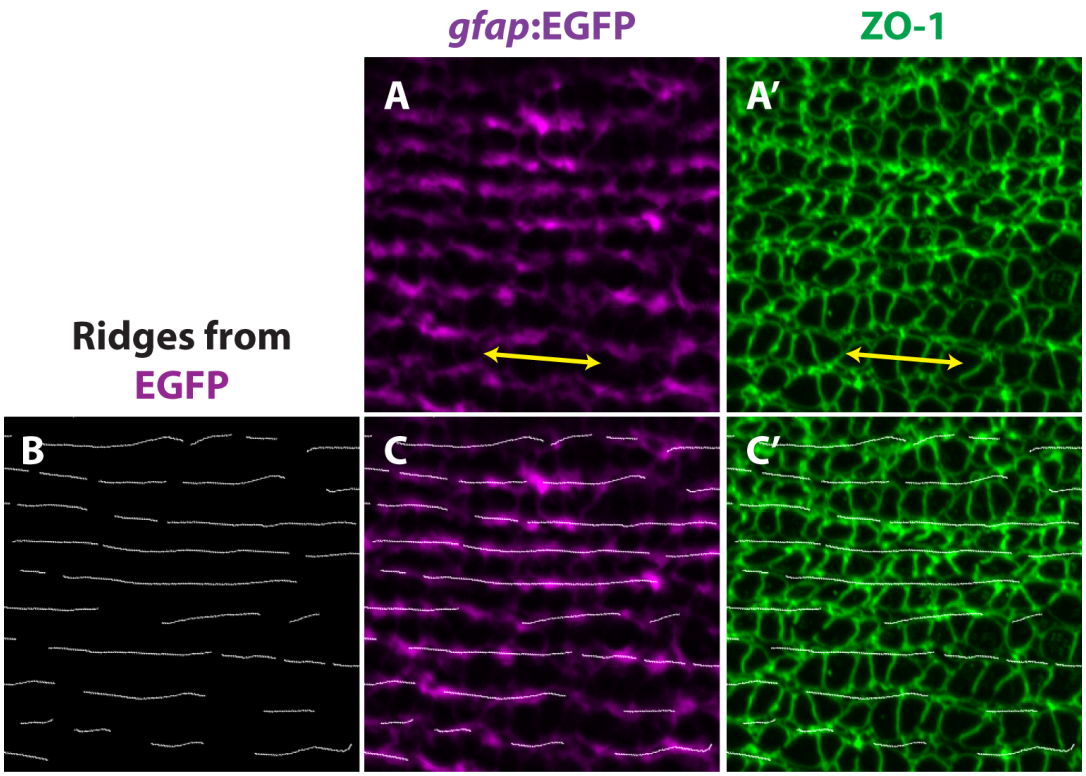

Figure 3.8: **Ridge detection of Müller glial bands in mature retina.** **(A-A')** Selective projection of EGFP (magenta) driven by Müller glia-specific promoter *gfap* showing thick bands between columns of photoreceptors and thin lamellae within columns (A). Cell profiles at the OLM is visualized by ZO-1 antibody (green, A'). Yellow arrows indicate column orientation. **(B)** Ridge lines showing orientation of EGFP bands detected by the ridge analysis described in the text. **(C-C')** Overlay of ridge lines on top of EGFP (C) and ZO-1 (C') intensities. Note how the ridge lines correctly divide photoreceptor cells into columns in C'. In (A-A', C-C') Selective Projection algorithm (Section 3.3) was used to project EGFP signal at the level of OLM as indicated by ZO-1.

column. The next section on FFT-based filtering attempts to remove the latter while keeping the former mostly intact, with the goal to eventually have ridge lines only at the thick Müller glia bands.

3.4.2 Directional filtering of ridge lines using Fast Fourier Transform

To filter out unwanted ridge lines from anything other than the thick intercolumn glial bands, we leverage on the observation that these 'false positive' lines are mostly short and perpendicular to the column direction. Taking Fast Fourier Transform (FFT) on the projected EGFP image immediately gave us with the orientation of the columns θ_c (Figure 3.7 C). Using the orientation output from the ImageJ plug-in described earlier, we can

efficiently accept only ridge pixels with orientation θ that deviates less than certain limit θ^* from the column orientation: $|\theta - \theta_c| < \theta^*$. This allows for some flexibility in accepting the ridge pixels, as not all correctly-identified ridge pixelss are perfectly parallel to θ_c. We found that $\theta^* \approx 30^\circ$ gives good balance between removing most of the false positives and keeping the desired ridges intact.

Further filtering was done based on the length of the continuous lines. We calculated the unbroken length of the ridge lines and eliminate those shorter than 20 pixels. The remaining ridge lines are shown to faithfully capture the thick Müller glia bands between adjacent columns (Figure 3.7 D-D').

3.4.3 Results

Figure 3.8 shows the analysis result on mature area of the retina. As expected, ridge lines follow the thick Müller glia bands and, when superimposed on ZO-1, nicely delineate the columns.

Applying the same analysis to the marginal zone (with slightly smaller filter width as mentioned above) confirms our earlier observation that the thick Müller bands do indeed extend beyond the mature area well into the unpatterned marginal zone (Figure3.9).

The presence of spatial ordering of Müller glia cells before column formation leads to an interesting hypothesis that these glial cells might somehow help the cone cells organize into straight columns as they mature. Combined with laser ablation result that thick Müller bands correlate with direction of higher tension (Section 3.5), this suggest that tension anisotropy might already be present early in the marginal zone before column formation. Taken together, this suggests a new, more active role of Müller glia cells in patterning epithelial tissues.

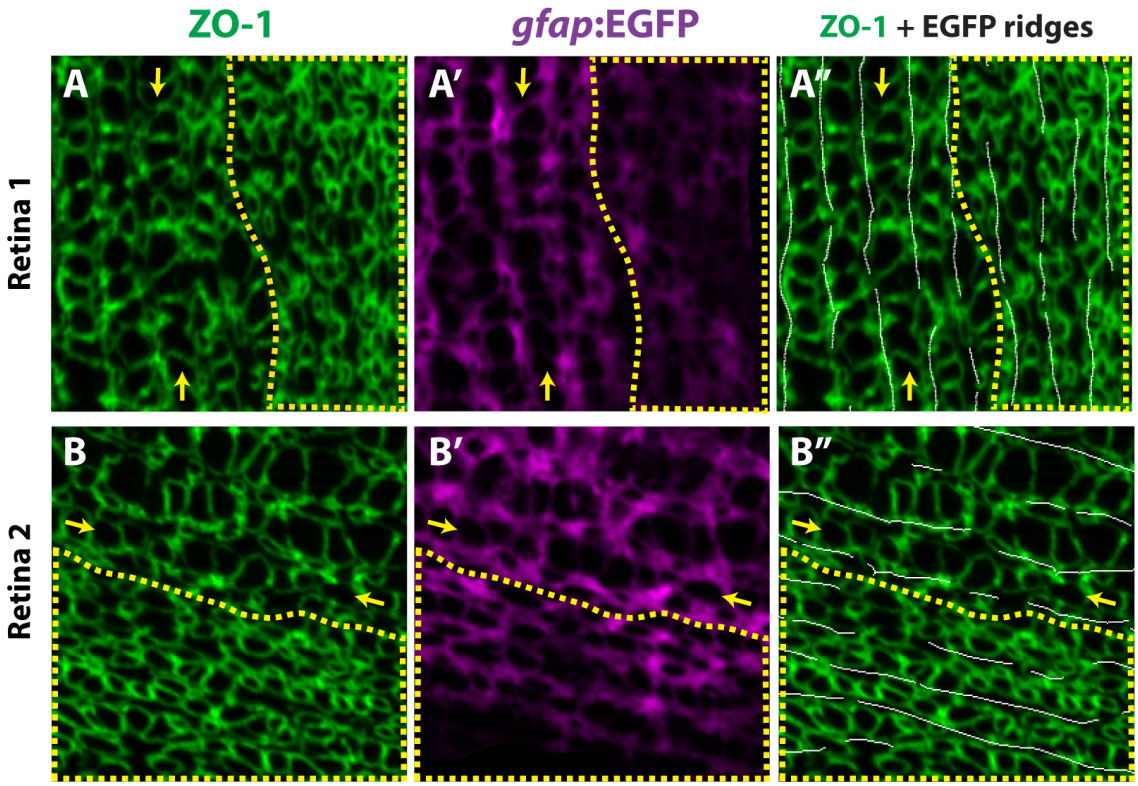

Figure 3.9: **Ridge detection of Müller glial bands at the margin. (A-B")** Two representative images showing the persistence of the ridge lines into the marginal zone. Antibody against ZO-1 (green) highlight cell profiles at the OLM, while *gfap*-driven EGFP (magenta) marks Müller glia cells. Yellow arrows indicate the last mature columns that can be identified from ZO-1 images. Dashed lines indicate the marginal zone where immature photoreceptor cells are packed randomly. Note in (A' & B') how Müller glia bands are already established in the marginal zone. (A" & B") show ridge lines divide progenitor cells into batches that presumably will join the mature retina at subsequent cycles, although columnar order is not yet established. Selective Projection algorithm (Section 3.3) was used to project EGFP signal at the level of OLM as indicated by ZO-1.

3.5 Analysis of Laser Ablation Experiment on Zebrafish Retina

In an earlier publication of our lab, we hypothesized that zebrafish retina tissue is subjected to anisotropic stress across the plane of the epithelium, and that this stress anisotropy is essential for patterning the cones into columns [38]. The paper focused on studying the mechanisms that lead to formation of straight columns of mature photoreceptor cells, from an initially disordered packing, at the proliferation/'marginal' zone (see Figure 3.1D). In the model presented there, mature cone cells have the ability to planar-polarize by localizing concentrations of some planar cell polarity (PCP) proteins in non rotationally-invariant way. These PCP proteins are then thought to modulate effective membrane tension by increasing adhesion (or equivalently, lowering interfacial tension) between adjacent cones in the same column. Hence, collective and consistent polarization of cells across the epithelium will cause the increase of junctional tension along the direction of the column relative to the perpendicular direction, and was shown that, together with progressive growth, it is sufficient to recreate the columnar order [38].

To achieve consistent polarization across all cones, the presence of some global orienting signal is required. We hypothesized that tissue-wide anisotropic mechanical stress plays this role [38, 80]. The retinal tissue is experiencing anisotropic stress due to ocular pressure and the presence the annular ligament, a rigid ring-like structure that holds the retinal epithelium near its periphery. This is supported by the observation that the mosaic order is absent in the larval-remnant region of the retina when the annular ligament is not yet present [38, 85, 105], and mosaic pattern arises as the fish grow and develop the ligament.

Here we tested the hypothesis that the retinal epithelium is under anisotropic tension by performing a laser ablation experiment ([81], also see Appendix C). A high power pulsed laser was used to selectively ablate Müller glial processes, thought to 'glue' photoreceptors together and support the anisotropic tension, and create holes in the tissue which will relax according to the mechanical stress present (see Appendix C for details on the experimental method). If the epithelium is under isotropic stress, we expect the ablated region to relax uniformly into circular shape. On the other hand, if the tissue is under anisotropic stress, we then expect the tissue to relax into an ellipsoidal shape with the long axis aligned with the direction of high stress. By tracking the recoil of cells around the ablation region, we can infer the anisotropic deformation that happens after ablation and showed that it is consistent with our hypothesis that mechanical tension is higher along direction parallel to the columns.

This work, along with that presented in Section 3.4, are included in a manuscript currently under consideration for publication at Nature Communications. The manuscript is attached in Appendix C.

3.5.1 Analysis Method

The data we have is in the form of z-stack images of live fish retina, taken right before ablation and at roughly 5 and 20 minutes after ablation. The experiment is performed on double-transgenic fish expressing *gfap:EGFP* and *trβ2:tdTomato* transgenes in the pigment-free mutant background. *gfap* is a promoter specific to the Müller glial cells and is expressed throughout the glia. It is used both to target Müller glial processes for ablation and to visualize the mosaic pattern at the level of the outer limiting membrane (OLM). At the OLM the Müller glia processes wraps around the photoreceptors, giving what effectively is an outline of their membranes. The cell tracking and deformation analysis described below is done at this level. The second transgene *trβ2* is a promoter marking red cone photoreceptors[7] and is used to check for photoreceptor damage (or rather, lack of thereof) after ablation. Ideally we want to eliminate only the tension-supporting glia and not the photoreceptors themselves. The presence of tdTomato signal, together with loss of EGFP after ablation, indicates that glial cells were successfully eliminated and at the same time red cones were left undamaged.

Since Leica's 2-photon microscope was used for image acquisition, the Z-stack images were saved in Leica's proprietary '.lif' format. We used Leica's 'LAS X' application (whose lite version is freely available for download from their website) to open the files and export the z-stack as tiffs[8]. To obtain the mosaic at the level of the OLM, we projected the EGFP channel using Selective Projection method described in Section 3.3[9]. We cannot use simple max-projection in this case since *gfap:EGFP* expression is not localized at the OLM, but extends to the regions above and below it. The Selective Projection algorithm is designed to look for and only project 'sharp features' such as the OLM, and ignore more fuzzy structures. However to obtain the best possible projection, we usually mask most of

[7] It has been shown in [106] that *trβ2* is expressed in red cone progenitor line that also give rise to horizontal and retinal ganglion cells. However, both the horizontal and ganglion cells migrate basally upon differentiation and only red cone photoreceptors remain at the OLM of adult retina.

[8] LAS X Version 1.1.0.12420 was used.

[9] In contrast to the previous sections, here we do not have ZO-1 antibody marking the OLM since we are working with live fish. Nevertheless, at the OLM the *gfap:EGFP* gives cell outlines similar to the ZO-1, while forming stalk-like processes far from it. We found that the Selective Projection algorithm does a decent job to recognize the ZO-like profiles of *gfap:EGFP* and is able to reject most of the stalk-like processes. To further improve the projection result, we did rough masking of the *gfap:EGFP* processes as described in the text.

the Müller glial processes by painting the image black with large brush on ImageJ. This should take little amount of time and even very rough masking will significantly reduce artifacts due to misidentification of the OLM. See Section 3.3 for details.

To quantify deformation as the tissue relaxes after ablation, we tracked both rod and cone photoreceptors 2-3 cell diameter thick surrounding the ablation region identified by loss of EGFP signal (see figure 3.11A). The centroids of the tracked cell were manually identified using ImageJ's 'Multi-point' tool and the coordinates were then exported to MATLAB. We experimented with various ways to automate detection of the cell centroids, including various combinations of morphological operations, edge detection methods, and watershed segmentation. However, we found that none of the automated procedures are able to identify cells with the desired accuracy and consistency. The problem lies mainly in the poor quality of the EGFP signal, especially at 20 minutes after ablation or longer (see figure 3.11A"-A"'). Since the number of images to be analyzed are not too large (8 ablation and 6 control retinas), we decided that it is more efficient to track cell positions manually.

3.5.1.1 Correcting for Sample Tilt

The raw z-stack images taken by the confocal microscope often have the sample tilted with respect to the focal plane of the microscope. Experimental constraints limit our ability to align the sample plane accurately. Worse still, as we are imaging live fish, the angle between the plane of the OLM (where we can see and track outline of cells) and the focal plane often change (see figure 3.10). If not accounted properly, a change of plane tilt angle between two images will show as strain along some axis. To correct for this, we numerically rotated the 3D coordinate of the cell centroids on each image, such that the OLM is parallel to the focal plane of the microscope.

To do this, we used the z-depth information from the Selective Projection algorithm (see 3.3). Briefly, the program does z-projection by trying to recognize sharp features (in this case, EGFP intensities at the level OLM), and select fluorescent signals only from this level. The program has an option to output the reconstructed surface (i.e. z-depth as a function of 2D coordinates $\mathbf{x_i} = (x_i, y_i)^\top$), which are then used to obtain z-values z_i^0 at each centroid position $\mathbf{x_i^0}$ before ablation. This gives pre-ablation cell centroid coordinate in 3D space $\mathbf{r_i^0} = (x_i^0, y_i^0, z_i^0)^\top$. We then fitted this collection of points with a plane using a least-square method similar to section 3.5.1.2 below. Such plane can be described by two vectors: a vector pointing to an (arbitrary) point on the plane $\mathbf{w}^0$ and a normal vector $\hat{\mathbf{n}}^\mathbf{0}$.

To align different planes from different images, it is easiest to rotate every single one such that their normal vector points along the z-axis, i.e. $\hat{\mathbf{n}} = (0, 0, 1)^\top$. This can be accomplished by rotating every centroid coordinate $\mathbf{r_i^0}$ to $\mathbf{r_i}$ according to Rodrigues rotation

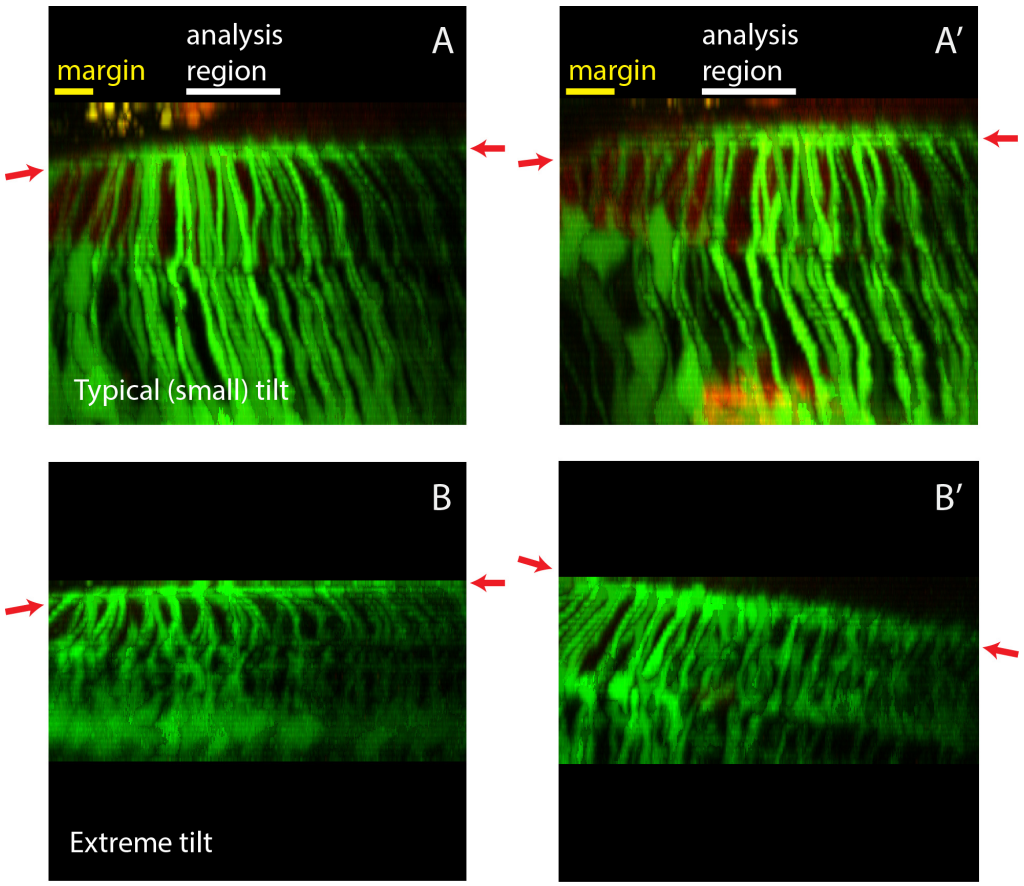

Figure 3.10: **Change in tilt angle of the OLM with respect to the imaging focal plane.** Cross-section view of live adult retinas on x-z plane with *gfap:EGFP* expressions (green) marking Müller glia cells. **(A-A')** Typical change in tilt angle between pre- (A) and post-ablation (A') images. Red arrows indicate the outer limiting membrane (OLM) where photoreceptor cells are tracked. Ablation and analysis regions (white bars) are chosen to be far enough from the marginal zones (yellow bars) so that they are relatively flat. **(B-B')** Example of extreme tilting that can occur before (B) and after ablation (B'). Samples with significant change in tilt angle ($> 15°$) such as this are excluded from analysis.

formula:

$$\mathbf{r_i} = \mathbf{r_i^0}\cos\alpha + (\mathbf{k}\times\mathbf{r_i^0})\sin\alpha + \mathbf{k}(\mathbf{k}\cdot\mathbf{r_i^0})(1-\cos\alpha), \tag{3.1}$$

where $\mathbf{k} = \hat{\mathbf{n}}^{\mathbf{0}} \times \hat{\mathbf{n}}$ and $\alpha = \hat{\mathbf{n}}^{\mathbf{0}} \cdot \hat{\mathbf{n}}$ are rotation axis and rotation angle, respectively. 2D centroid coordinates $\mathbf{x_i}$ on the (rotated) plane of OLM can then be obtained from $\mathbf{r_i}$ for 2D deformation analysis.

The above procedure was repeated for all pre- and post-ablation images. Note that since we are imaging near the margin of the retina, the actual plane of OLM is almost always curved (see Figure 3.10). When fitting a plane through the tracked cells, we assume that the cells are far enough from the margin such that the OLM is locally flat. The goodness of this assumption can be checked by computing the fitting residual (root-mean-square error) – high residual suggests that the assumption does not hold very well. In our cases, most of the residuals are low, on the order of the z-resolution of the imaging, suggesting that the areas we are working on are indeed locally flat. MATLAB code given in Appendix A.3.1.

3.5.1.2 Least Square Deformation

We assumed that the deformation on the plane of the OLM is affine and can be written as:

$$\hat{\mathbf{y}}_i = \mathbf{M}\mathbf{x}_i + \mathbf{b} \tag{3.2}$$

for some d-by-d matrix $\mathbf{M}$ and d-by-1 offset vector $\mathbf{b}$. $\mathbf{x}_i$ is d-by-1 vectors of pre-ablation (tilt-corrected) coordinate the i-th cell, while $\hat{\mathbf{y}}_i$ is the coordinate obtained after transformation 3.2 above. The dimension d is 2 in this case (i.e. we assume the deformation happens primarily on the plane of the epithelium), but can in principle take higher values. We then want to find $\mathbf{M}$ and $\mathbf{b}$ that minimizes the mean-squared error between the transformed $\hat{\mathbf{y}}_i$ and the actual post-ablation (tilt-corrected) coordinates $\mathbf{y}_i$ for all N cells tracked:

$$\min_{\mathbf{M},\mathbf{b}} \mathbf{R}(\mathbf{M},\mathbf{B}), \tag{3.3}$$

where:

$$\mathbf{R} = \sum_{i=1}^{N} \|\mathbf{y}_i - \hat{\mathbf{y}}_i\|^2 = \sum_{i=1}^{N} \|\mathbf{y}_i - \mathbf{M}\mathbf{x}_i - \mathbf{b}\|^2 . \tag{3.4}$$

Following the usual approach to solve ordinary least square problem (see, for example, [100]), we can write the above equation more compactly in full matrix notation by

concatenating the N coordinates into augmented matrices defined as follow:

$$\widetilde{\mathbf{X}} = \begin{bmatrix} 1 & 1 & ... & 1 \\ \mathbf{x}_1 & \mathbf{x}_2 & ... & \mathbf{x}_N \end{bmatrix}, \qquad \widehat{\widetilde{\mathbf{Y}}} = \begin{bmatrix} 1 & 1 & ... & 1 \\ \hat{\mathbf{y}}_1 & \hat{\mathbf{y}}_2 & ... & \hat{\mathbf{y}}_N \end{bmatrix},$$
$$\widetilde{\mathbf{Y}} = \begin{bmatrix} 1 & 1 & ... & 1 \\ \mathbf{y}_1 & \mathbf{y}_2 & ... & \mathbf{y}_N \end{bmatrix}, \qquad \widetilde{\mathbf{M}} = \begin{bmatrix} \mathbf{b} & \mathbf{M} \end{bmatrix}. \tag{3.5}$$

Then we can write equation (3.2) simply as $\widehat{\widetilde{\mathbf{Y}}} = \widetilde{\mathbf{M}}\widetilde{\mathbf{X}}$, and the least-square problem of equation (3.4) as:

$$\begin{aligned} \mathbf{R} &= \sum\nolimits_i \left\| \mathbf{y}_i - \widetilde{\mathbf{M}}\mathbf{x}_i \right\| \\ &= \mathrm{tr}(\widetilde{\mathbf{Y}}^\top \widetilde{\mathbf{Y}}) - \mathrm{tr}(\widetilde{\mathbf{Y}}^\top \widetilde{\mathbf{M}} \widetilde{\mathbf{X}}) - \mathrm{tr}(\widetilde{\mathbf{X}}^\top \widetilde{\mathbf{M}}^\top \widetilde{\mathbf{Y}}) + \mathrm{tr}(\widetilde{\mathbf{X}}^\top \widetilde{\mathbf{M}}^\top \widetilde{\mathbf{M}} \widetilde{\mathbf{X}}). \end{aligned} \tag{3.6}$$

To find $\widetilde{\mathbf{M}}$ that minimizes equation (3.5), set $\frac{\partial \mathbf{R}}{\partial \widetilde{\mathbf{M}}} = 0$. This gives:

$$\widetilde{\mathbf{M}} = \widetilde{\mathbf{Y}}\widetilde{\mathbf{X}}^\top (\widetilde{\mathbf{X}}\widetilde{\mathbf{X}}^\top)^{-1}, \tag{3.7}$$

from which $\mathbf{M}$ and $\mathbf{b}$ can be extracted using definition (3.5). Note that the matrix $\widetilde{\mathbf{X}}\widetilde{\mathbf{X}}^\top$ has dimension d-by-d and is independent of the number of cell N, so the method remains appropriate for large scale analysis where, in typical applications, N can be arbitrarily large but the dimension d remains low.

Note that we assumed that the deformation is affine (equation 3.2) and along the plane of the epithelium. To verify that this is indeed a good assumption, we can calculate the residual (root-mean-square error) of the fitting. For all the samples included in the analysis (i.e. those not exhibiting extreme tilt), we found that the residuals are low (Tables 3.2-3.3). This suggests that the deformation is indeed affine.

3.5.1.3 Polar Decomposition

The transformation encoded in $\mathbf{M}$ contains both elastic deformation of the epithelium as well as rigid rotation (e.g. from movement of live fish and/or microscope stage between acquisitions). To account for possible rotation, we performed polar decomposition on $\mathbf{M}$, defined as:

$$\mathbf{M} = \mathbf{U}\mathbf{P}, \tag{3.8}$$

where $\mathbf{U}$ is unitary and $\mathbf{P}$ is positive-semidefinite Hermitian. (In our case $\mathbf{M}$ is necessarily real, so it follows that $\mathbf{U}$ and $\mathbf{P}$ are orthogonal and PSD symmetric, respectively.)

$\mathbf{U}$ and $\mathbf{P}$ are given as follow:

$$\begin{aligned}\mathbf{P} &= (\mathbf{M}^\top \mathbf{M})^{1/2} \\ \mathbf{U} &= \mathbf{M}\mathbf{P}^{-1}.\end{aligned} \tag{3.9}$$

The angle ϕ of the rigid rotation between the images can then be easily computed from $\mathbf{U}$. In our case it turns out that this angle is small ($\approx 1^\circ$ on average), suggesting that the microscope stage does not rotate much (although it does have significant amount of linear drift as measured by $\mathbf{b}$). Live fish movement typically results not only in rotation but also drastic change in tilt plane. Samples with unambiguous fish movement (abrupt jumps or distortions on z-stack images) were identified manually during visual inspection stage prior to analysis and were excluded.

The amount and direction of the (principal) strains are given by the eigenvalues and eigenvectors of $\mathbf{P}$, respectively. Anisotropy is then defined as the ratio of the difference of the principal strains to their average. The angle θ that the eigenvectors make with respect to the x-axis can also be easily computed. Ideally, the eigenvector corresponding to the larger eigenvalue (i.e. largest relaxation) should point parallel to the column direction where tension is highest. However we found that in some experiments this is not always the case, although the deviation is always less than 45°. This discrepancy could be caused by ablation that is not perfectly circular. Since a single Müller glial process wraps multiple photoreceptor cells at the OLM, it is practically-impossible to create perfectly-isotropic ablation by targeting Müller glial processes. MATLAB code for the entire analysis is given in A.3.2.

3.5.2 Results

We analyzed two groups of data: experiment and control groups. In the experiment group, Müller glia processes were ablated with high-power laser, causing photoreceptor cells to recoil away from each other. In the control groups, the exact same protocol was followed except that the ablation step was done with the laser turned off. See [81] for details on experimental methods. Analysis for ablation and control groups are presented in Tables 3.2 and 3.3. Note that x- and y-strains are strain perpendicular and parallel to the columns, respectively.

Figure 3.11 A-A'' shows tracked cells around ablation region. x- and y-strains are plotted in Figure 3.11 E-F. Our result shows that, while there is no significant difference ($p = 0.1128$) in x-strain (perpendicular to the columns) between control and ablation groups, the latter shows significantly higher y-strain (parallel to the columns) compared

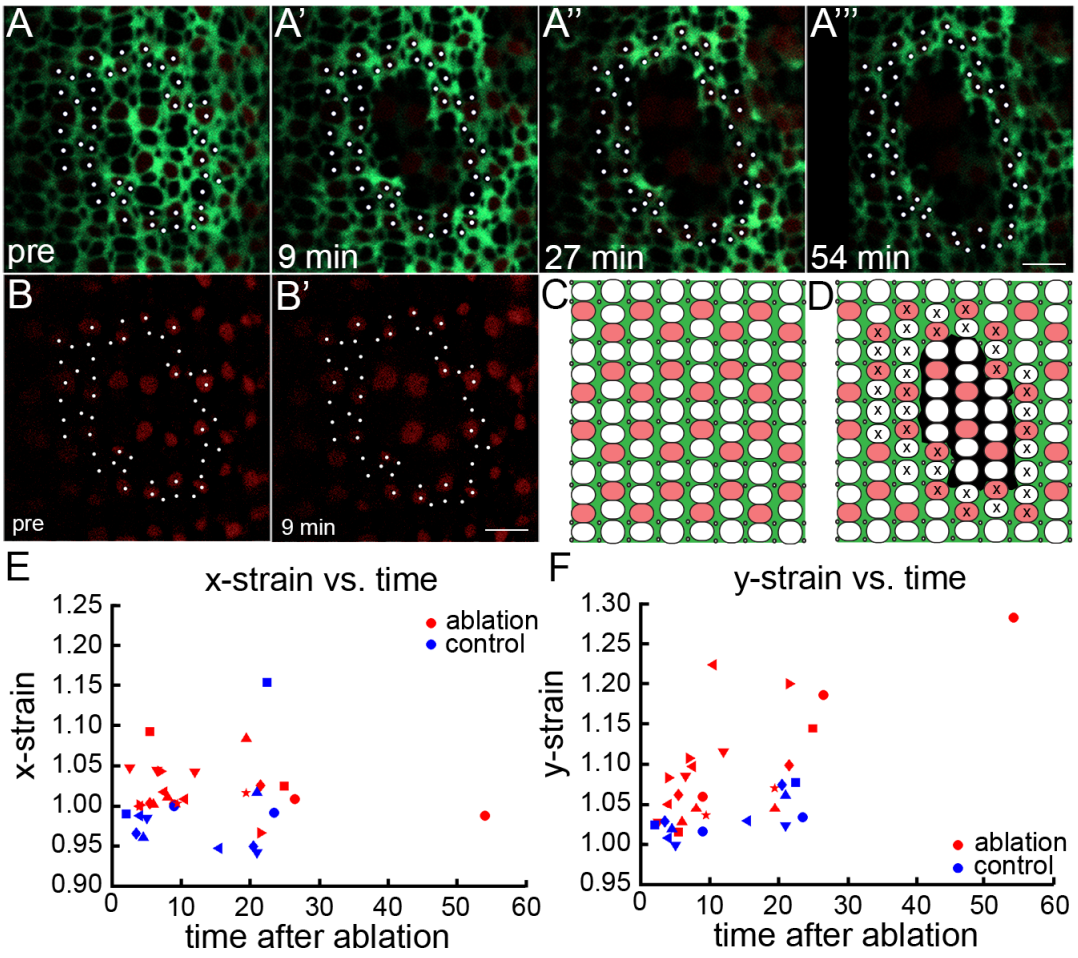

Figure 3.11: **Laser ablation of Müller glial processes.** (A-A") Live imaging time course of targeted Müller glial ablations in *Tg*(*gfap*:EGFP) (green) and *Tg*(*trβ2*:tdTomato) (red) juvenile zebrafish. Photoreceptor profiles tracked for strain analysis (white dots). (A'-A"') Hole in sheet of Müller glial processes at the OLM. Relaxation of surrounding retinal epithelium at 9 min (A'), 27 min (A"), and 54 min (A"') after ablation. (B-B') *Tg*(*trβ2*:tdTomato)+ Red cones survive Müller glial ablation. (C-D) Schematic of pre- (C) and post-ablation (D). Cone cells tracked for strain analysis are marked by 'x'. (E-F) Mechanical strain perpendicular (x-strain, E) and parallel (y-strain, F) to retinal margin. Strains greater and smaller than 1 represent stretching and compression, respectively. Each retina is represented by a different shaped symbol (n=6 controls; n=8 experimental). Horizontal axis is time interval between ablation and middle of the post-ablation imaging scan; two or three post-ablation scans collected for each retina. Scale bars: 5 μm (A"' and B'). Selective Projection algorithm (Section 3.3) was used to project EGFP and tdTomato. Figure adapted from [81].

to control ($p = 0.0008$). p-values were obtained using the (univariate) Welch's unequal-variance test [107, 108]. Confirming this, Hotelling's multivariate unequal-variance test [108, 109] using both x- and y- strains also shows significant (p = 0.0002) difference between the two groups.

Our result shows that the adult retina epithelia are under anisotropic stress. Higher y-strain relative to the perpendicular direction supports our hypothesis that thick Müller glia bands along columns support higher tension than thinner lamellae seen in the perpendicular direction (see also Chapter 3.4 on analysis of thick Müller glia bands). This tension differential might be important in coordinating PCP in cone cells and pattering them into straight columns, as suggested in [80]. This work is included in our recently-submitted manuscript [81], attached in Appendix C.

Table 3.2: Ablation group data

Name	Time after ablation (mins)	No of cells	x-principal strain	y-principal strain	Principal axis angle θ°	RMSE deformation (px)	RMSE plane fit (px)
Fish 1	9	51	1.00	1.06	5	1.7	35
	26.5	51	1.01	1.19	-1	4.3	89
Fish 31	5.5	53	1.09	1.01	-40	2.9	32
	25	53	1.03	1.14	21	4.1	32
Fish 32	5.5	51	1.00	1.06	27	4.0	49
	21.5	51	1.03	1.10	38	5.2	36
Fish 34	6	48	1.00	1.03	23	2.2	31
	8	48	1.01	1.04	37	3.0	42
	19.5	48	1.08	1.04	-37	2.9	25
Fish 35	2.5	54	1.05	1.03	-33	2.8	48
	6.5	54	1.04	1.08	27	3.6	51
	12	54	1.04	1.11	17	4.3	49

Table 3.2: Ablation group data (continued)

Name	Time after ablation (mins)	No of cells	x-principal strain	y-principal strain	Principal axis angle θ°	RMSE deformation (px)	RMSE plane fit (px)
Fish 37	4	59	1.00	1.05	-16	3.7	29
	7.5	59	1.02	1.10	-10	5.1	29
	10.5	59	1.01	1.22	-7	7.8	30
Fish 38	4	50	1.00	1.08	14	4.0	33
	7	50	1.04	1.11	14	4.5	27
	21.5	50	0.97	1.20	12	7.6	86
Fish 30	9.5	49	1.00	1.03	-30	2.7	32
	19.5	49	1.02	1.07	-22	3.8	39

Table 3.3: Control group data

Name	Time after ablation (mins)	No of cells	x-principal strain	y-principal strain	Principal axis angle θ°	RMSE deformation (px)	RMSE plane fit (px)
Fish 18C	6	50	1.00	1.02	24	2.1	25
	23.5	50	0.99	1.03	8	3.1	23
Fish 19C	2	45	0.99	1.02	35	1.8	39
	22.5	45	1.15	1.08	-6	2.6	29
Fish 20C	3.5	53	0.97	1.03	-2	1.8	24
	20.5	53	0.95	1.07	3	2.9	25
Fish 21C	4.5	53	0.96	1.02	7	2.3	29
	21	53	1.02	1.06	18	3.2	24
Fish 22C	5	57	0.99	1.00	0	1.5	14
	21	57	0.94	1.02	-1	2.1	26
Fish 23C	4	54	0.99	1.01	-12	1.5	34
	15.5	54	0.95	1.03	-3	2.1	36

CHAPTER 4

Correlation Analysis of Morphogenetic Noise

During development, animals frequently have to make laterally-symmetric organs. This perfect development between pairs of left and right organs is crucial for proper function and survival of the individuals. For example, *Drosophila* left and right wings grow to remarkable size and shape precision. Although there are some variations between different individuals, within the same animal the relative size between the left and right wings is controlled very precisely. It has been proposed that this precision is essential to the individual's fitness and ability to fly [110–113]. However, how biology achieves this precision in the presence of stochastic noise is not at all obvious. Often these left and right organs grow from different tissues on different sides of the animal (e.g. in the case of fly, left and right wings grow from different larval imaginal discs), and whether there is feedback between them coordinating their development is still hotly-debated [114–116].

This work is a collaboration with Yohanns Bellaïche from Institut Curie, Paris, who hosted us during our 6-month stay in early 2016. Working on *Drosophila* pupa dorsal thorax (also known as notum), they have established a state-of-the-art technique for high spatial- and temporal-resolution live imaging of large scale epithelial remodeling that happens during metamorphosis. They can capture live movies at 5 minutes resolution for over 24 hours and digitally track everything that happens during this period, including cell movements, apical contractions, divisions, and apoptosis. This yields a wealth of information on what is happening at the cellular scale as the tissue is being sculpted.

The final adult thorax is composed of symmetrically-shaped left and right halves, separated by a straight midline running along the anterior-posterior axis. Embedded in each half are 7 macrochetae that have stereotypical positions and shapes. Their unique shapes provide easy ways to quantify the symmetry between the two halves and, together with the midline, serve as landmarks to measure relative positions across the tissue. Although the notum maintains symmetrical shapes and macrochetae positions throughout development, this symmetry does not extend to cellular level. At this scale, cells are packed randomly and thus their positions and numbers do not have clear correspondence between the left and

right halves[1]. Cell division and apoptosis, too, happen stochastically and are not in mirror symmetry at the individual cell level. This stochasticity in turn imparts significant noise (i.e. wiggles) in individual cell trajectories. Given this randomness, it is not clear how the notum is able to maintain its symmetry throughout the remodeling process.

Although the movies were acquired for a different purpose[2], we thought they could shed some light to an interesting question: How growth and morphogenesis are coordinated in development to produce symmetrical organs despite noisy cell movements. We should point out that we became interested in this question after reading an internship report by Anaïs Bailles that claimed this noise has unexpected scaling like $\Delta x \Delta t$. A naïve model based on the assumption that the noise on both halves is random and uncorrelated predicts that the noise should diminish like the volume of the averaging window $(\Delta x)^2 \Delta t$ (see Section 4.2). If the claim is true, this would mean that the noise is not uncorrelated and suggest that more complex mechanisms, such as those involving feedback or coordination between the two halves, are at play.

Naturally, we proceed by first verifying the claim above. We showed, by means of data collapse, that the noise between the two halves does scale unexpectedly like $\Delta x \Delta t$. Unfortunately, only one movie has the full notum with both sides visible, and the remaining has only half of the notum visible[3]. We then tried various analyses on the hemi-notum movies in an attempt to extract the same information. Although some of the things we tried ended up being scraped for various reasons, there are things we can learn from them. Thus, these methods are included in Appendix B for future reference. Finally, we obtained auto-correlation maps for the hemi-nota as a function of space and time, and found some curious negative correlations at 15-20 minutes time-lag.

4.1 Introduction

The *Drosophila* dorsal notum is a monolayer epithelial tissue at the back of the animal. Starting at around 10 hours after pupa formation (hAPF), it undergoes various morphogenesis processes that shape it into the adult thorax (Figure 4.1). This large scale tissue remodeling, which last for about 24 hours, includes several rounds of cell divisions, apop-

[1]Exception to this are the number and location of stereotypical cells, such as those forming macrochetae.

[2]The notum movies are published as part of their works in elucidating the role of Fat/Dachsous PCP pathways in notum morphogenesis [117] and formulating new quantitative framework to analyze tissue deformation [118].

[3]This is related to the fact that the movies were originally taken for different purposes. In their published work using the same dataset [117, 118], they argued that both hemi-nota from the same animal are identical for their analysis. In addition, segmenting the cells requires substantial manual labor to correct for mistakes made by automated segmentation algorithm. Both of these favor collecting data for just half of the notum.

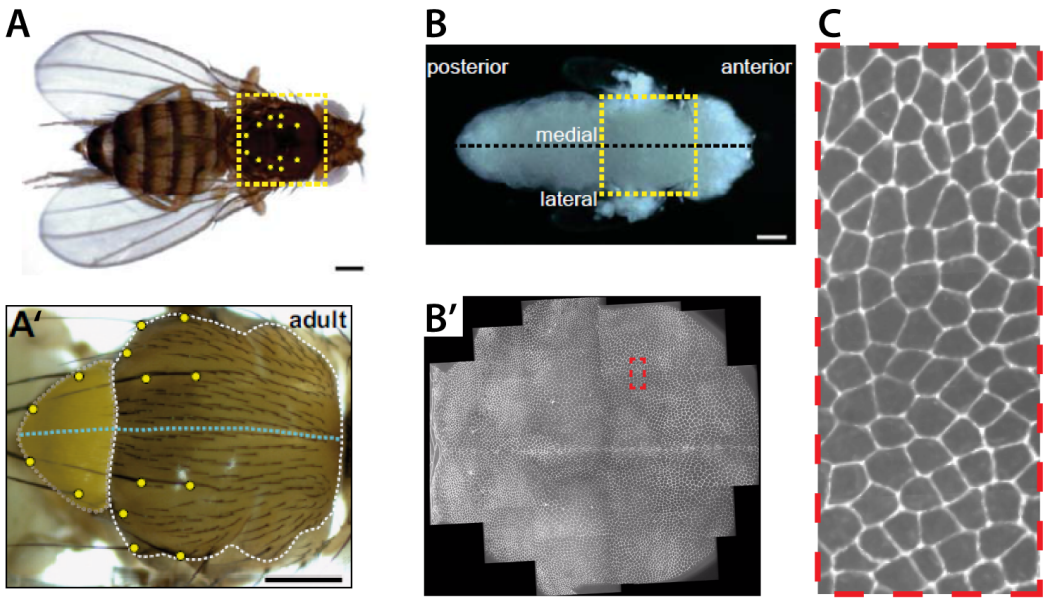

Figure 4.1: **Fly dorsal notum. (A-B')** *Drosophila* dorsal notum () is shown in adult fly (A-A') and pupa (B). Yellow dots indicate the position of the macrochetae, while midline is shown as blue dashed line in A', and can also be seen as bright central line in B'. A frame grab from the full notum movie is shown in B', and zoomed in C showing GFP intensity from E-Cadherin:GFP. In this and subsequent figures, head (anterior) is always oriented to the right and tail (posterior) to the left. Data provided by Bellaïche group and is published in [117, 118].

toses, delaminations, cell rearrangements, and collective cell flows (among other thing, to form neck invagination just anterior to it) [118]. Also happening during this period is the formation of macrochetae – organs that will grow bristles in the adult animal – which can be easily identified during the latter half of morphogenesis from their unique shape. They are also highly symmetrical in location between the left and right halves of the notum. The two halves are separated by a midline, where cells form continuous junctions that run straight along the anterior-posterior axis.

The notum was imaged in flies carrying Cadherin:GFP construct to label adherens junctions. Live imaging of the pupae was done for about 24 hours between 14 and 28 hours after pupa formation (hAPF) at every 5 minutes. A confocal spinning disk microscope (Nikon) was used to acquire 18-28 z-slices (0.5 μm/slice) at several overlapping positions that were then stitched together to give full (or half) view of the notum. A full-notum movie was constructed from 24 such overlapping tiles, while half-notum movies contained 10-12 overlapping positions. See [117, 118] for more details on imaging procedure. Hemi-notum movies were acquired the same way except that only positions covering one half of the notum were imaged. In total, one full-notum movie and 3 hemi-notum movies were collected (available as Supplemental Video in [117, 118]). For hemi-notum analyses (Section 4.4), we digitally split the full-notum movies along the midline to generate two additional hemi-notum movies that were analyzed independently.

Prior to analysis, the movies were segmented through multiple iterations of automatic and manual rounds as described in [118]. Cells were then tracked using a custom MATLAB algorithm developed by the Bellaïche group, taking into account cell division, apoptosis, and movement into and out of the imaging field of view. Altogether, around 7.7×10^6 cell contours were segmented and tracked across the five hemi-notum movies [118]. This yields a wealth of information of time and location of cell rearrangements, flows, divisions, and apoptosis throughout the morphogenesis. Their respective contributions to the overall tissue remodeling has been quantified in a recently publish work by Guirao *et. al.* [118]. For this study, however, we are particularly interested in looking at the movement of the cell centroids.

We observed that individual cell movements are particularly noisy – they jiggle around some mean flow in a random and non-symmetrical fashion. Several mechanisms contributing to this noisy movement are stochastic cell division and apoptosis (which, although happen at the same general area, are not perfectly symmetrical at cellular scale between left and right hemi-nota). It is still unclear how this noise is compensated during development (or, indeed, if it needs to be compensated at all) to achieve the desired accuracy between the two halves. We will show in Sections 4.3 and 4.4 that the noise appears to be

correlated, suggesting that some mechanism is possibly regulating it.

4.2 Model of left-right velocity correlation

We start by assuming that, in absence of noise, both left and right hemi-nota of the same animal share a common morphogenetic flow $\vec{u}(\vec{x}, t)$. The actual observed cell movements might not be exactly the same between left and right due to the presence of noise, and can be written as:

$$\begin{aligned} \vec{v}_L(\vec{x}, t) &= \vec{u}(\vec{x}, t) + \vec{\xi}_L(\vec{x}, t) \\ \vec{v}_R(\vec{x}, t) &= \vec{u}(\vec{x}, t) + \vec{\xi}_R(\vec{x}, t), \end{aligned} \tag{4.1}$$

where the zero-mean noise terms $\vec{\xi}_L$ and $\vec{\xi}_R$ are assumed to be white and uncorrelated:

$$\overline{\xi_L} = \overline{\xi_R} = \overline{\xi_L \xi_R} = 0, \tag{4.2}$$

where the averaging $\overline{(\,\cdot\,)}$ is over different realizations of the noise.

We expect the noise to have common strength that decays as we average over larger space and time. More specifically, we expect it to decay like the *volume* of the averaging box $\Omega = (\Delta x)^2(\Delta t)$:

$$\overline{\langle \xi_L \rangle^2} = \overline{\langle \xi_R \rangle^2} = \sigma^2 \propto (\Delta x)^{-2}(\Delta t)^{-1}, \tag{4.3}$$

where $\langle\,\cdot\,\rangle$ denotes averaging over space-time box Ω.

Let us also define the mean and variance of the morphogenetic flow $\vec{u}$ averaged over some space and time centered at $(\vec{x}', t')$ as:

$$\langle \vec{u} \rangle_{\vec{x}', t'} = \vec{U}(\vec{x}', t') \tag{4.4}$$

$$\mathrm{var}(\vec{u})_{\vec{x}', t'} = \Delta^2(\vec{x}', t'). \tag{4.5}$$

Then we can calculate the correlation between left and right flow velocities $\vec{v}_L$ and $\vec{v}_R$ in terms of the above quantities[4]:

$$R = \mathrm{corr}(\vec{v}_L, \vec{v}_R) = \frac{\mathrm{cov}(\vec{v}_L, \vec{v}_R)}{\sqrt{\mathrm{var}(\vec{v}_L)\,\mathrm{var}(\vec{v}_R)}} = \frac{\Delta^2}{\Delta^2 + \sigma^2}. \tag{4.6}$$

[4]Here we assume that the average over box volume is the same as the average over noise realizations.

This can be normalized such that it scales simply with Δx and Δy:

$$\begin{aligned}\frac{R}{1-R} &= \frac{\Delta^2}{\sigma^2} \\ &\propto (\Delta x)^2(\Delta t). \end{aligned} \tag{4.7}$$

This equation gives the expected scaling of left and right correlation in terms of the size of averaging window.

Another quantity that is expected to scale with Ω is the variance of the difference of the two velocities:

$$\begin{aligned}\mathrm{var}(\vec{v}_L - \vec{v}_R) &= \overline{\langle \vec{v}_L - \vec{v}_R \rangle^2} - \overline{\langle \vec{v}_L - \vec{v}_R \rangle}^2 \\ &= 2\sigma^2 \\ &\propto (\Delta x)^{-2}(\Delta t)^{-1}. \end{aligned} \tag{4.8}$$

Equations 4.7 and 4.8 give the expected scaling of two easily-computed quantities as a function of different averaging intervals Δx and Δt, assuming that the noise is uncorrelated. Deviation from the expected scaling would imply either that the noise between left and right is not uncorrelated, or that they have long range correlation. As previously mentioned, this work was motivated by Anaïs' claim that the correlation scales like $(\Delta x)(\Delta t)$, which suggest that the noise is potentially correlated and/or a mechanism more interesting than the simple model above is at play.

In equations 4.7 and 4.8, we essentially use the velocity from both halves to subtract off the (unknown) morphogenetic flow $\vec{u}(\vec{x}, y)$. This leaves us only with the noise from both halves, which then we know how they are expected to scale. Clearly, this trick works only for the movie containing the full notum. For the hemi-nota movies, where only either the left or right half of the notum are visible, the best we can do is to calculate the variance of either left or right velocity, given by:

$$\begin{aligned}\mathrm{var}(\vec{v}_L) &= \overline{\langle \vec{v}_L \rangle^2} - \overline{\langle \vec{v}_L \rangle}^2 \\ &= \Delta^2 + \sigma^2. \end{aligned} \tag{4.9}$$

We see that the price we pay for only using half the notum is that we cannot eliminate Δ^2. Recall that Δ^2 is the variance of the morphogenetic flow (which can and does vary over space and time). This is saying that with half notum we cannot tell the difference between variation caused by the noise versus actual variation of the underlying mean flow. We will see in Section 4.4 that Δ^2 is non-negligible, and that prevented us from getting nice data

collapse like we had in the full-notum case.

4.3 Analysis of full-notum movie

To calculate left-right correlation from the full-notum movie, two averaging windows of size $(\Delta x, \Delta x, \Delta t)$ were setup at corresponding locations on both the left and right halves. Δx and Δt are specified in units of pixels (0.32 μm/pixel) and frame number or time-step (5 minutes/frame), respectively. v_L and v_R were then calculated as the average velocities of cells with centroids inside the window. Δx was varied between $16 \leq \Delta x \leq 256$ in powers of two, while Δt was varied independently between $1 \leq \Delta t \leq 24$ in unit step.

For each combination of Δx and Δt, the averaging windows were translated by $\frac{\Delta x}{4}$ in both spatial directions and by unit step in time to cover the entire movie. When a window contains a region with no segmented cells (which usually happens near the edges of the notum), velocities from both sides are discarded. This resulted in several thousand pairs of v_L and v_R averaged at different Δx and Δt. We then calculated the correlation coefficient R and the variance $\mathrm{var}(v_L - v_R)$ in equations 4.7 and 4.8.

To check that the noise does not follow the scaling predicted by the uncorrelated noise model in Section 4.2, we plotted the normalized correlation versus volume $\Omega = (\Delta x)^2(\Delta t)$ (Figure 4.2A). It is pretty clear that the data points do not collapse as predicted by the model, suggesting some correlation is present in the noise. We then plotted the normalized correlation and variance against $\Delta x \Delta t$ and obtained data collapse (Figure 4.2B-C), confirming Anaïs' claim that the noise scales like $\Delta x \Delta t$.

At this point, it is pretty clear that either: (1) the noise as defined by equation 4.1 is correlated, or (2) our assumption that both left and right halves share common mean morphogenetic flow $\vec{u}(\vec{x}, t)$ is somehow incorrect. One biologically-plausible scenario that would explain the latter is that if morphogenesis of the left and right halves are not synchronized (e.g. one is significantly delayed with respect to the other). To check relative morphogenesis progression of the two halves, we followed a method to register development time described in [117, 118]. It has been observed that the posterior part of the notum exhibit strong but transient rotational flow. By aligning these peaks of rotation rate, defined to be 18:40 hAPF, one can synchronize development times across animals. We applied the same analysis independently on both halves of the full notum to check whether there is any significant discrepancy in their development.

Plot of rate of rotation for both halves of the full notum is shown in Figure 4.3. It shows that both halves are already synchronized, at least according to this measurement. (This is really not surprising, since they are from the same animal.)

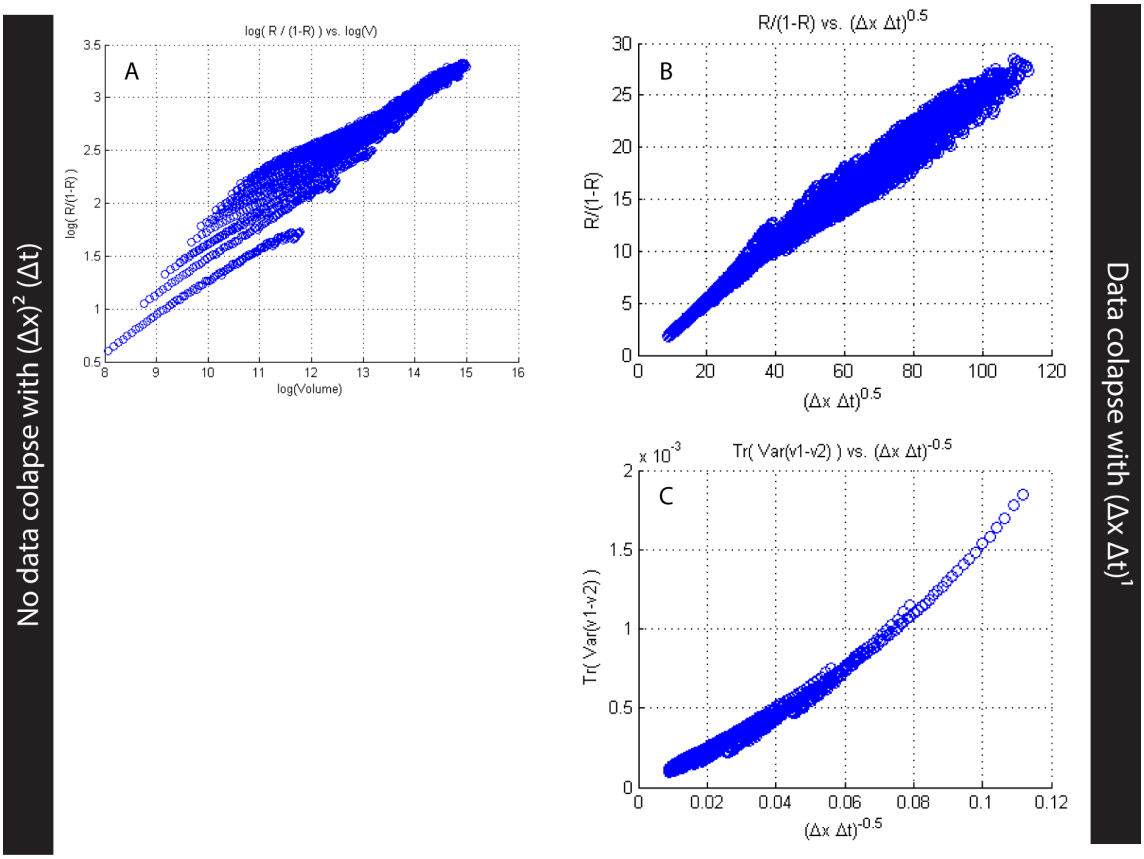

Figure 4.2: **Scaling of noise in full-notum movie. (A)** Normalized correlation coefficient does not collapse when plotted against volume $\Omega = (\Delta x)^2(\Delta t)$. **(B-C)** Data collapse of normalized correlation (B) and variance of left-right velocity difference (B) when plotted against $(\Delta x)(\Delta t)$. See also equations 4.7 & 4.8.

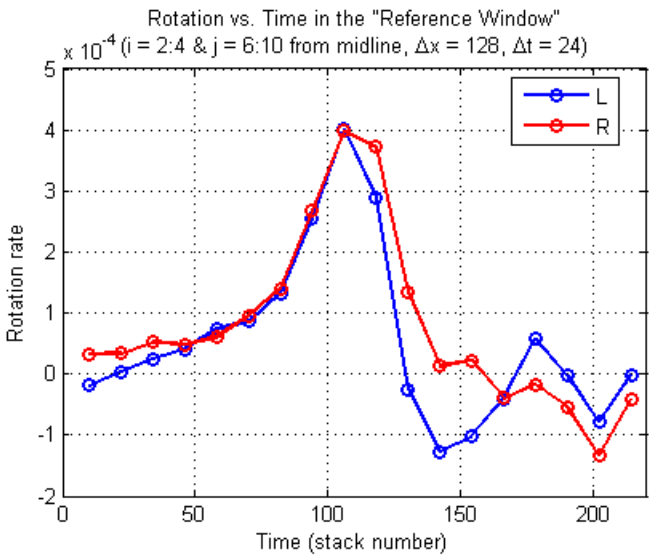

Figure 4.3: **Rate of rotation of left and right halves of full notum show that they are in synchrony**, suggesting that delayed morphogenesis is not the cause for the observed correlated noise. Rate of rotation is computed as the anti-symmetric part of the deformation tensor $\frac{1}{2}(\frac{\partial v_x}{\partial y} - \frac{\partial v_y}{\partial x})$ on the scutellum near the midline, and time on x-axis is given in unit of movie frame number (multiples of 5 minutes starting at 13:55 hAPF). See [118] for more details on the use of scutellum rotation rate as biological reference time.

To summarize, so far we have demonstrated that the noise between both halves does not satisfy the naïve model presented in equation 4.1 with white uncorrelated noise. We have also ruled out one biologically-plausible scenario where morphogenesis of the two halves happens at a different rate or time. Ideally, we would like to perform further analysis on more than one sample. However, since segmenting and tracking additional full-notum movies are prohibitively expensive[5], we decided to focus our attention on the available hemi-notum movies instead.

4.4 Analysis of half-notum movies

For the rest of the analysis involving hemi-notum movies, we split the full-notum movie digitally near the midline to make two additional hemi-notum movies. A total of 5 hemi-nota movies were analyzed independently. The movies were segmented and tracked as

[5]We have also explored ways to analyze new movies without having to perform costly segmentation. We tried to use particle image velocimetry (PIV), including a more advanced variation with deformable windows, to get velocity field without having to perform segmentation and cell tracking. Briefly, PIV produces displacement field by correlating an image with another taken shortly after. However we found that even with the more sophisticated window-deformation PIV, we could not get velocity field that accurately matches the tracking result. This was a useful exercise nonetheless, and it is discussed in more detail in Appendix B.1.

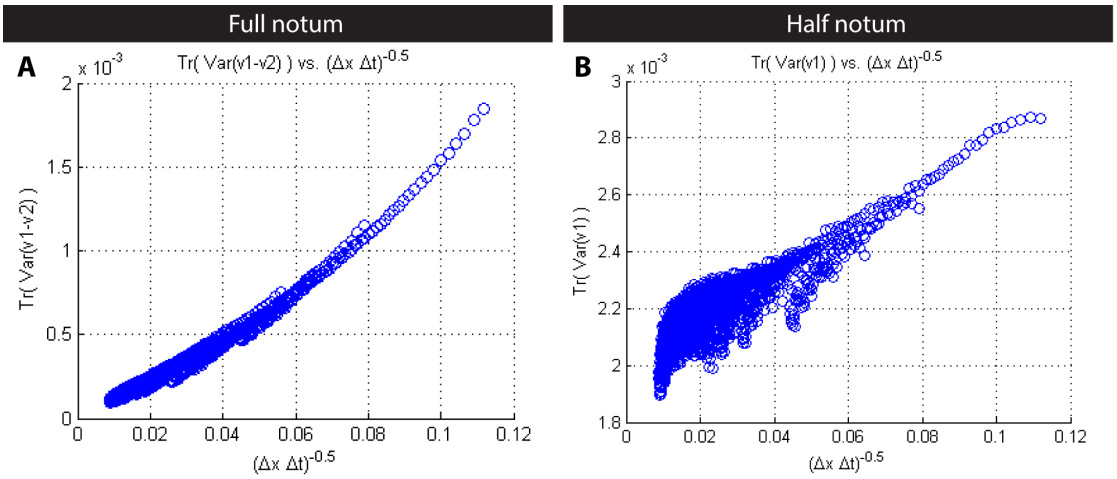

Figure 4.4: **Variance of velocity of hemi-notum does not show nice data collapse** (B) as it does in the full-notum case (A). In hemi-notum, only velocities from one half of the notum are available, and thus the variance does not scale as the noise (see equation 4.9). Panel (A) is previously shown in Figure 4.2 and is replicated here for comparison.

described in section 4.3 and in [118]. Averaging windows of varying size were set up as before. However since we did not have the other half of the notum to compare against, all we could do was to calculate the variance of the average velocities on the hemi-nota.

4.4.1 No data collapse on hemi-notum average velocity

Plot of the variance of v_L as a function of $\Delta x \Delta t$ is given in Figure 4.4. Clearly it lacks the nice data collapse we previously had on the full-notum case. One can understand this in several ways. First, using equation 4.9, one can see that the price we pay of just using one half of the notum is that we have an additional Δ^2 term. This term generally will scale differently with respect to Δx and Δt, thus destroying the data collapse. Another equivalent way to understand the problem is that by realizing the difficulty in separating noise from meaningful morphogenetic movements (i.e. the 'signals'). The average velocity at a given point is assumed to be the sum of the meaningful morphogenetic flow plus noise. The morphogenetic flow, however, is unknown and varies in time and space. Hence with only half the notum, we have no clear way to identify and separate the noise from the average movements[6].

[6]We explored some ideas to better define the meaningful morphogenetic noise, and hence the noise, by using interanimal averages. This follows the analysis by Guirao *et. at.* [118] to create universal archetypal morphogenesis map of the notum by averaging over different animals. However we found that, for our purposes, slight variation between animals is enough to throw the analysis off. Due to this interanimal variation, the remainder velocity after subtraction with the archetypal morphogenesis flow is still highly-

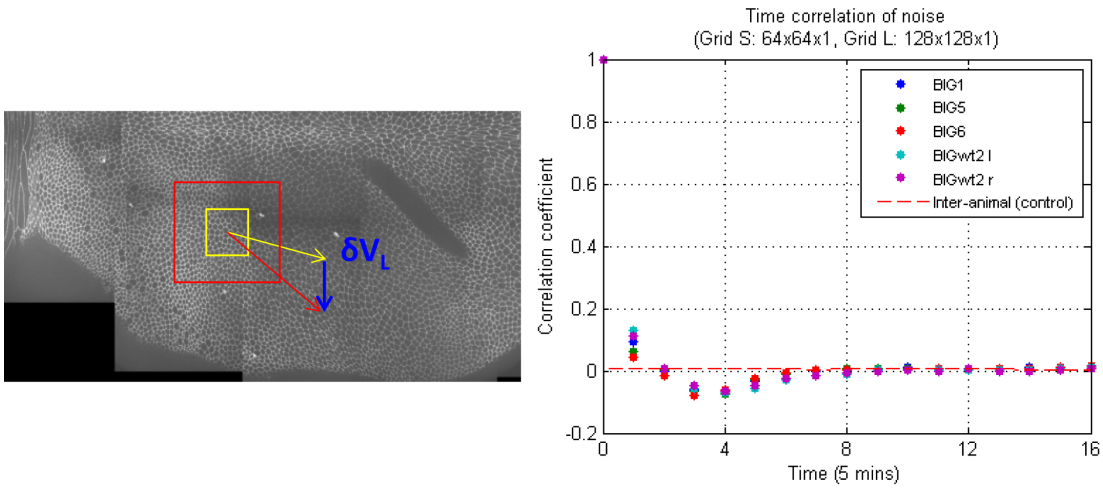

Figure 4.5: **Auto-correlation of hemi-notum movies**. Two concentric windows of different sizes (left) are used to estimate the amount of noise. Auto-correlation averaged across all time and positions (right) shows significant negative correlation at about 15-20 minutes time-lag for all hemi-nota. Control is calculated as cross-correlation between different hemi-nota (colored circular markers). Sizes of averaging windows are $128 \times 128 \times 1$ (large) and $64 \times 64 \times 1$ (small).

4.4.2 Auto-correlation with different window sizes

Another approach we tried is to calculate average velocities using two concentric averaging windows of different sizes (Figure 4.5, left). We expect that the larger window gives averaged velocity closer to the true morphogenesis flow[7], while the smaller window will produce a noisier average. Hence we define the difference of the two average velocities as the noise. We are then interested in looking at the autocorrelation of this noise with some time lag.

Figure 4.5 shows the average autocorrelation as a function of the time lag for all 5 hemi-nota, labeled as different colors of circular markers. Size of the large window was 128x128 pixels-by-1 frame (5 minutes), and the small window was 64x64x1. Auto-correlation was averaged over all time and spatial locations with 50% overlap between adjacent averaging windows. As a control, we calculated average cross-correlation between different animals. Note that all hemi-nota show consistent and significant negative correlation at around 15-20 minutes. While it potentially suggests something interesting is at play, we first have to rule out less interesting possibilities.

A possible case of the negative correlation we cannot rule out at the moment is cell division. It is known that epithelial cells tend to increase their apical area just prior to cy-

correlated. See Appendix B.2 for more details.

[7]This is limited by the scale over which the morphogenesis flow itself varies.

tokinesis. This swelling has the effect of pushing the surrounding cells away, and possibly drawing them back close again once the division is complete. It is thought that the whole process happens at roughly the same time-scale, making it a possible candidate to explain the negative auto-correlation. To examine this further, we decided to compute the spatial map of this auto-correlation and compare that to what is known about the distribution of cell divisions in the system [118].

4.4.3 Spatial map shows regions of positive and negative autocorrelations

To compute spatial auto-correlation maps, a similar approach was used except that we do not average over spatial locations. To compensate for lack of spatial averaging, time averaging was increased to 24 frames (2 hours) to keep the number of data points reasonable. Figures 4.6 and 4.7 show representative correlation maps at 5 and 20 minute time-lags, respectively. At 5 minutes lag, we see strong positive auto-correlations at the posterior-distal part of the notum (also known as the 'scutellum'). Towards the end of the morphogenesis, negative correlations start to emerge at center near the midline. At 20 minutes time-lag, negative correlations are seen at the scutellum part where it was previously positively-correlated. The map at 20 minutes time-lag does not change much over time, with the overall notum remains slightly negative. All 5 hemi-nota analyzed share the same qualitative features.

Though interesting, the implications of these correlation maps are not entirely clear. The scutellum area with strong positive and negative correlations corresponds to the area where active tissue remodeling happens most prominently. However the timing and location do not quite match that of cell divisions. It is known that cell divisions happen in two rounds, first at around 19 hAPF covering the whole notum and second at around 24 hAPF mostly at the scutellum. The positive and negative correlations of the scutellum, however, remain roughly constant throughout the entire movie.

4.5 Conclusion

In this work, we showed that noisy cell movement during *Drosophila* pupa notum morphogenesis does not follow a naïve model where the observed movement is simply the sum of morphogenetic flow and some uncorrelated noise term. Rather, study of the full-notum movie suggests that the noise might be correlated and has non-trivial $\Delta x \Delta t$ scaling. This is different than the expected $(\Delta x)^2 \Delta t$ scaling one would expect from white, uncorrelated

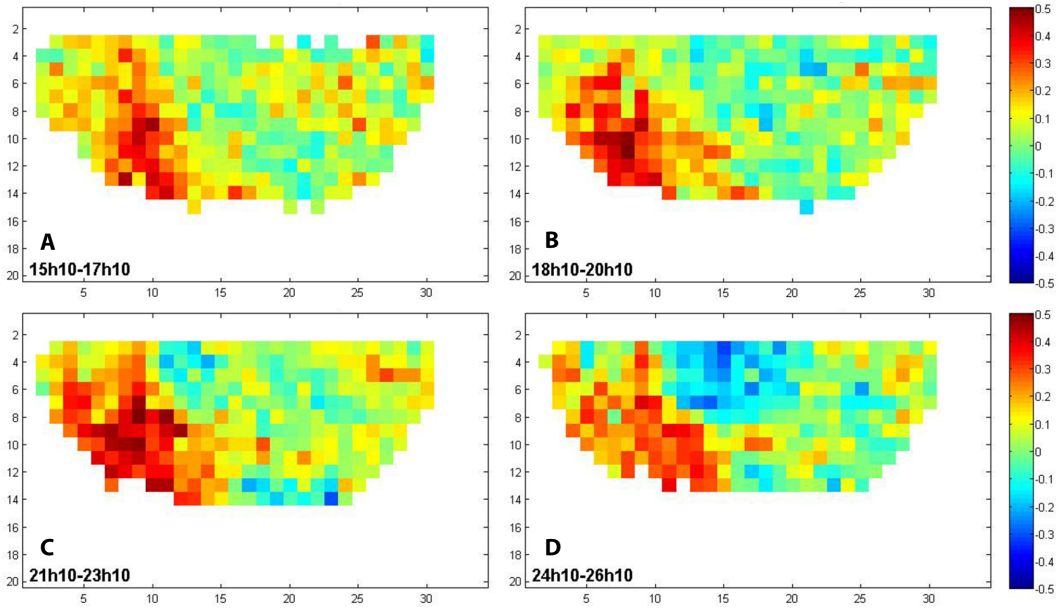

Figure 4.6: **Spatial map of auto-correlation at 5 minutes time-lag**, showing strong positive correlation at the distal-posterior scutellum area. Strong negative correlation develops at the middle of the notum towards the end of the metamorphosis. Time window for averaging are given in hours after pupa formation (hAPF).

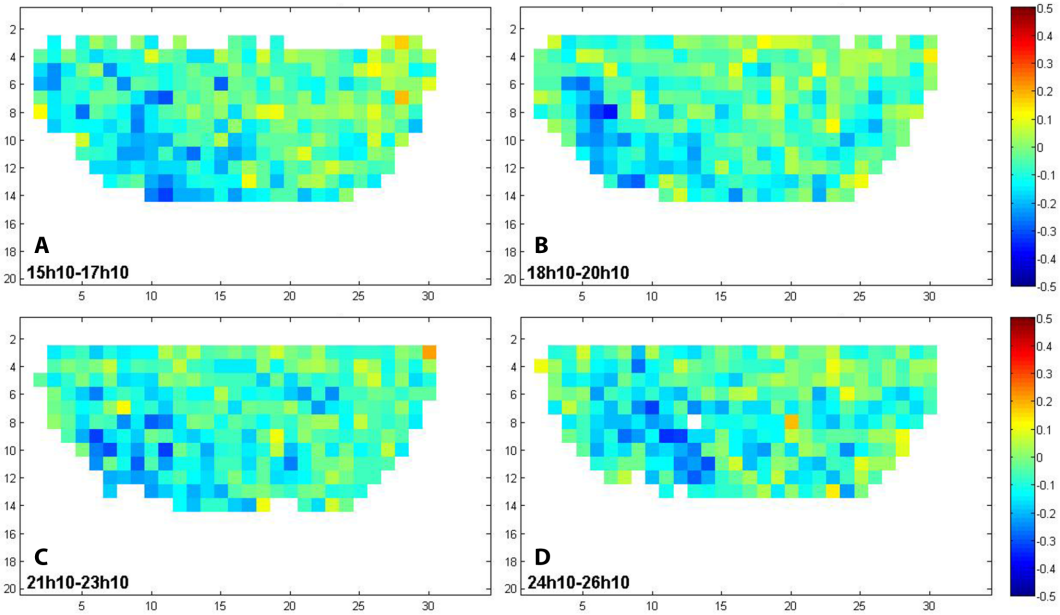

Figure 4.7: **Spatial map of auto-correlation at 20 minutes time-lag** showing negative correlation at the distal-posterior scutellum area.

noise. However, lack of more full-notum movies has prevented us from elucidating its biological significance.

Backing the above result using hemi-notum movies proved to be more complicated than it was initially expected. Lack of the other half of the notum means that separating meaningful morphogenesis movements from noise is no longer trivial. Approaches in estimating the meaningful morphogenesis flow were presented, though lacking the clarity of simple comparison of the full-notum. We believe that analysis of full-notum movies still offers the best way to confirm the presence of correlated noise, as well as to elucidate the mechanisms responsible for it. However, the laborious nature of performing segmentation and cell tracking on the movies has limited our ability in obtaining more full-notum data.

Finally, we are grateful to Yohanns Bellaïche for providing the data and helpful discussions. This project would not have been possible without his collaboration. We also thank Jesus Lopez-Gay and Floris Bosveld for performing the experiments and processing the movies, Boris Guirao and Stéphane Rigaud for providing segmentation and tracking MATLAB routines, and to the entire Bellaïche group for their hospitality during our wonderful stay in Paris.

APPENDIX A

MATLAB Codes

This appendix contains MATLAB codes discussed in Chapter 3. All codes were tested in Version R2014a. When appropriate, values of free parameters used in the analyses are listed in brackets at the beginning of each code.

A.1 Analysis of *tbx2b* Mutant Column Fragments

A.1.1 FindEdges.m

```
function N = FindEdges(M, strelsize, edgethr, graythr)

%%%%%%%%%%%%%%%%%%%%%%%%%%%%%%%%%%%%%%%%%%%%%%%%%%%%%%%%%%%%%%%%%%%%%%%%%%%%%%%
% Function to perform edge detection-based cell segmentation.
% Tested to work well on clean, high contrast images, such as: ZO-1 with
% antigen retreival.
%
% M         : grayscale input image (e.g. ZO-1 max-projection)
% strelsize : structuring element size for imclose smoothing/gap filling
%             Larger values better fill gaps, but will produce rounder cell
%             profiles
%             (recommended value: varies between 1-5 depending on image)
% edgethr   : threshold for Canny edge detection (0-1).
%           : (default: 0 = automatic threshold)
% graytresh : threshold for BW conversion.
%             Set to 0 to set automatic threshold using Otsu's method.
%             (default = 0)
%
%     Jeremy Hadidjojo (hjeremy@umich.edu), 2013
%
%%%%%%%%%%%%%%%%%%%%%%%%%%%%%%%%%%%%%%%%%%%%%%%%%%%%%%%%%%%%%%%%%%%%%%%%%%%%%%%

M = imadjust(M);    % maximize contrast
M = wiener2(M);     % noise reduction with adaptive Wiener filter
if edgethr == 0;
    E = edge(M, 'canny');        % find edges with Canny method
else
    E = edge(M, 'canny', edgethr);
```

```
end


if graythr == 0;
    M1 = im2bw(M, graythresh(M));        % threshold
    graythresh(M)
else
    M1 = im2bw(M, graythr);
end
E1 = E | M1;        % add thresholded image to E to fill in holes
E2 = imclose(E1, strel('disk', strelsize));   % morphological closing

N = ~E2;
N = imclearborder(N);
imagesc(N);
```

codes/FindEdges.m

A.1.2 ProjectRodImages.m

```
function R = ProjectRodImages(N,S)

%%%%%%%%%%%%%%%%%%%%%%%%%%%%%%%%%%%%%%%%%%%%%%%%%%%%%%%%%%%%%%%%%%%%%%%%%%%%
% Find z-slice image sharpest for a particular cell and extract rod channel
% (green) for that cell. Cell outline is Red, and rod stain is Green.
% N = segmented BW image (for example, from FindEdges.m)
% S = cell of z-stacks (from ReadImageSequence.m)
%
% Free parameter:
%   strelsize: size of structuring element for dilation
%   (default: 5 pixels, but may be adjusted depending on image resolution)
%
% Created by: Jeremy Hadidjojo (hjeremy@umich.edu)
% Created on: 05/21/13
%
% Last modified on:
%
%%%%%%%%%%%%%%%%%%%%%%%%%%%%%%%%%%%%%%%%%%%%%%%%%%%%%%%%%%%%%%%%%%%%%%%%%%%%

strelsize = 5;
Strelement = strel('disk', strelsize);

R1 = uint8(zeros(size(N)));
R = uint8(zeros(size(S{1})));
CC = bwconncomp(N);     % find connected component
L = labelmatrix(CC);
Ncomp = CC.NumObjects
Nslice = length(S);

% extract Red and Green channels;
Red = cell(Nslice,1);
Green = cell(Nslice,1);
for i = 1:Nslice
    Red{i} = S{i}(:,:,1);
    Green{i} = S{i}(:,:,2);
end

for i = 1:Ncomp
    if mod(i,100)==0
        sprintf('Processing cells %d/%d', i, Ncomp)     % progress indicator
    end
    Comp = (L == i);        % get i-th component
    CompPacked = bwpack(Comp);          % pack BW image to improve performance of
    imdilate below
    CompDilate = imdilate(CompPacked, Strelement, 'ispacked');
    CompDilate = bwunpack(CompDilate, size(Comp,1));    % unpack
    Outline = CompDilate - Comp;        % get outline surrounding Comp
    OutlineInd = find(Outline);

    % find z-slice with sharpest outline
    Val = zeros(1,Nslice);
    for j = 1:Nslice
        Val(j) = sum( Red{j}(OutlineInd) );
```

```
    end

    [~,ind] = max(Val);     % z-slice index with highest ZO intensity around Outline
    CompIndex = find(Comp);
    R1(CompIndex) = Green{ind}(CompIndex);
end

R(:,:,1) = im2uint8(bwperim(N));      % red channel = segmented perimeter
R(:,:,2) = R1;              % green channel = rod staining
```

codes/ProjectRodImages.m

A.1.3 SeparateRodsCones.m

```
function [Rods,Cones, Im] = SeparateRodsCones(N,R,th)

%%%%%%%%%%%%%%%%%%%%%%%%%%%%%%%%%%%%%%%%%%%%%%%%%%%%%%%%%%%%%%%%%%%%%%%%%%%%
% Separate rods and cones from the segmentation N based on the intensity of
% rod staining R
%
%       ** Requires statistic toolbox for K-means clustering **
%
% N = segmented BW image (e.g. from FindEdges.m)
% R = projected rod staining intensity (from ProjectRodImages.m)
%
% Free parameters:
%   Amin and Amax (set in line 29 below), minimum and maximum area of
%   normal cells. Cells with area outside this range are excluded.
%
% Created by: Jeremy Hadidjojo (hjeremy@umich.edu)
% Created on: 05/23/13
% Last modified on:
%
%%%%%%%%%%%%%%%%%%%%%%%%%%%%%%%%%%%%%%%%%%%%%%%%%%%%%%%%%%%%%%%%%%%%%%%%%%%%

R = R(:,:,2);
CC = bwconncomp(N);
L = labelmatrix(CC);
Stats = regionprops(N, R, 'MeanIntensity', 'Area', 'PixelIdxList');
A = [Stats.Area];

% Filter cell with absurd area
Amin = 25;
Amax = 200;
idx = find( (A < Amin) | (A > Amax) );
for i = 1:length(idx)
    px = Stats(idx(i)).PixelIdxList;
    N(px) = 0;
end

CC = bwconncomp(N);
L = labelmatrix(CC);
Stats = regionprops(N, R, 'MeanIntensity', 'Area', 'PixelIdxList');
A = [Stats.Area];
I = [Stats.MeanIntensity];

if th == 0 % do k-means
    idx = kmeans(I',2);   % k-means clustering on intensity
    ConesInd = find(idx==1);
    RodsInd = find(idx==2);
    MaxI = max(I(ConesInd));
    sprintf('Max cone intensity: %f', MaxI)
else
    ConesInd = find(I<=th);
    RodsInd = find(I>th);
end
```

```
hist(I(ConesInd))
hold on
hist (I(RodsInd))
hold off

Cones = ismember(L, ConesInd);
Rods = ismember(L, RodsInd);
Im = zeros(size(R));
Im(Cones) = R(Cones);
Im(Rods) = R(Rods);
```

codes/SeparateRodsCones.m

A.1.4 FindNeighborsDilate.m

```
function [A,LabMat] = FindNeighborsDilate(BW, strelsize)

%%%%%%%%%%%%%%%%%%%%%%%%%%%%%%%%%%%%%%%%%%%%%%%%%%%%%%%%%%%%%%%%%%%%%%%%%%%%
% Find neighbors based on morphological dilation. Dilate a cell and see
% which other cell it overlaps with.
%
% BW = binary image input
% strelsize = size of structuring element
% A = output adjacency matrix (i.e.: A(i,j) = 1 if i & j are neighbors, 0
% otherwise)
%
% Created by: Jeremy Hadidjojo (hjeremy@umich.edu)
% Created on: 06/30/13
% Last modified on:
%
% List of modifications:
%
%%%%%%%%%%%%%%%%%%%%%%%%%%%%%%%%%%%%%%%%%%%%%%%%%%%%%%%%%%%%%%%%%%%%%%%%%%%%


CC = bwconncomp(BW);
L = labelmatrix(CC);
Ncomp = CC.NumObjects
Strelement = strel('disk', strelsize);

A = zeros(Ncomp,Ncomp);

for i = 1:Ncomp
    Mask = L==i;
    Mask = bwunpack(imdilate( bwpack(Mask), Strelement, 'ispacked' ), size(Mask,1));
    LMasked = L(find(Mask));
    [~,~,val] = find(LMasked);
    val = unique(val);

    for j = 1:length(val)
        A(i,val(j)) = 1;
        A(val(j),i) = 1;
    end
end

A = A - eye(size(A));
LabMat = L;
```

codes/FindNeighborsDilate.m

A.1.5 RefineNeighbor.m

```
function [A1,I] = RefineNeighbor(A,LabMat,StrelSize)

%%%%%%%%%%%%%%%%%%%%%%%%%%%%%%%%%%%%%%%%%%%%%%%%%%%%%%%%%%%%%%%%%%%%%%%%%%%%
% Refine neighbor/adjacency A found by FindNeighborsDilate.m based on the
% follwing extra condition:
%   When cells i & j are subjected to morphological closing with
%   structuring element of size StrelSize, the region R filled between the
%   cells i & j must have area greater than Amin.
%
% M = grayscale ZO image
% A = adjacency matrix to be refined (from FindNeighborsDilate.m)
% LabMat = label matrix of the segmented image (from FindNeighborsDilate.m)
% StrelSize = size of structuring element to determine overlap region
%             (default = 10)
%
% Other free parameters (see also: paper and thesis text):
%   dmin (default 10)
%   AspectRatioMin (default: 2 for loose, 2.5 for stringent)
%
%
% Created by: Jeremy Hadidjojo
% Created on: 07/01/13
% Last modified on:
%
% List of modifications:
%
%%%%%%%%%%%%%%%%%%%%%%%%%%%%%%%%%%%%%%%%%%%%%%%%%%%%%%%%%%%%%%%%%%%%%%%%%%%%

% Minimum separation
dmin = 10;
AspectRatioMin = 2;

A = triu(A);
[i,j] = find(A);
Strelement = strel('disk', StrelSize);

length(i)

I1 = zeros(size(LabMat));
I2 = I1;
Amin = 20;

for k = 1:length(i)
    L = ismember(LabMat, [i(k), j(k)]);

    % morphological closing
    R = logical(imclose(L,Strelement) - L );
    Stats = regionprops(R, 'Area', 'MajorAxisLength', 'MinorAxisLength', 'PixelIdxList'
    , 'Orientation');

    if isempty(Stats)
        A(i(k),j(k)) = 0;
        A(j(k),i(k)) = 0;
```

```
        continue
    end

    % Area
    [Area,ind] = max([Stats.Area]);     % pick only the largest connected component (
    index ind)
    if Area < Amin
        A(i(k),j(k)) = 0;
        A(j(k),i(k)) = 0;
        continue
    end
    pxlist = Stats(ind).PixelIdxList;

    % Angle
    % angle of centroid-to-centroid
    Stats0 = regionprops(logical(L), 'Centroid');
    centr = cat(1, Stats0.Centroid);
    dx = centr(1,1) - centr(2,1);
    dy = centr(1,2) - centr(2,2);
    theta0 = atand(-dy/dx);      % (-) sign due to how matlab handle images

    % angle of filled region
    theta = Stats(ind).Orientation;
    dtheta = abs(theta - theta0);

    if (dtheta <= 45) || (dtheta >= 135)
        d = Stats(ind).MajorAxisLength;
        l = Stats(ind).MinorAxisLength;
    else
        l = Stats(ind).MajorAxisLength;
        d = Stats(ind).MinorAxisLength;
    end
    R = l-d;

    lmin = d * AspectRatioMin;

    if (d > dmin && l > lmin)
        I1(pxlist) = 1;
    else
        I2(pxlist) = 1;
        A(i(k),j(k)) = 0;
        A(j(k),i(k)) = 0;
    end

end

A1 = logical(A + A');

I = cat(3,logical(LabMat),I1,I2);
```

codes/RefineNeighbor.m

A.2 Selective Projection of z-stack images

A.2.1 Estimate_OLM_From_ZO.m

```
function [mi02_projection, ZO_projection, ZOmax, zpos_double] = Estimate_OLM_From_ZO(S,
    Smi02)

%%%%%%%%%%%%%%%%%%%%%%%%%%%%%%%%%%%%%%%%%%%%%%%%%%%%%%%%%%%%%%%%%%%%%%%%%%%%%%%%
% Function to estimate OLM and do selective projection.
%
% Picks out z-slice corresponding to strongest ZO signal, construct the
% surface of the ZO (i.e. OLM), then selectively-project another
% fluorescence marker onto this level.
%
% S = cell containing z-stack of RGB images. Use 'ReadImageSequence.m' to
% generate S.
% Smi02 = (OPTIONAL) grayscale image stack containing fluorescence marker
% to be projected onto ZO. If using this input, then S must also be
% grayscale image stack (not RGB cell) containing ZO marker. (i.e. if the
% image has dimension row x col and there are n stacks, then S and Smi02
% are (row x col x n) matrix of uint8)
%
%   Default parameter values: see parameter table below.
%
%   Created by: Jeremy Hadidjojo (hjeremy@umich,edu), May 2015
%   Last modified:  02/23/16
%
%   Version history:
%       04/29/15  function created
%       05/01/15  added texture filtering and background compensation
%                   created parameter table for easy parameter change
%       12/01/15  added description header
%
%       02/23/16
%       - added rejection of peaks broader than MaxStdev - useful for mi02
%         and other non-localized marker
%       - fixed bad parameter reference for nFitPoints (now -> p{19,2})
%
%%%%%%%%%%%%%%%%%%%%%%%%%%%%%%%%%%%%%%%%%%%%%%%%%%%%%%%%%%%%%%%%%%%%%%%%%%%%%%%%


%% Parameter Table

% To simplify various tunable parameters, let's make a table of all the
% parameters

%%%%%%%%%%%%%%%%%%%%%%%%%%%%%%%%%%%%%%%%%%%%%%%%%%%%%%%%%%%%%%%%%%%%%%%%%%%%%%%%
% Input parsing %
p{1,1}='ZO channel';                    p{1,2}=1;       % ZO RGB channel from image (
    not used if input is 2 stacks with ZO and mi02 separated)
p{2,1}='mi02 channel';                  p{2,2}=2;       % mi02 RGB channel from image (
    not used if input is 2 stacks with ZO and mi02 separated)
                                                        % (Red = 1, Green = 2, Blue =
    3)
```

```
% Preprocessing %
p{3,1}='wiener2';                       p{3,2}=1;       % Whether to do wiener filter denoising before max projection
p{4,1}='wiener2 size';                  p{4,2}=5;       % Size of wiener2 filter
                                                        % NOTE: This is NOT noise reduction for the output ZO/mi02 projection (see below for these)
                                                        % hence aggressive setting is recommended to minimize picking wrong Z-slice due to noise/speckles!

p{10,1}='Mask out background';          p{10,2}=1;      % Whether to try to mask out background using entropy filter (Separate_ROI_from_background.m)
p{11,1}='Mask threshold';               p{11,2}=0.5;    % Threshold for entropy filter

p{5,1}='ZOmax threshold';               p{5,2}=0.7;     % Threshold for ZO max projection to pick out areas with significant ZO signal
                                                        % (0 = use Otsu's method to determine threshold automatically (NOT recommended!) )

p{6,1}='Background compensation';       p{6,2}=1;       % Whether to do background compensation/subtraction
p{7,1}='Background comp size';          p{7,2}=50;      % Size for calculating background compensation (imclose)

p{8,1}='CLAHE';                         p{8,2}=1;       % Whether to do adaptive histogram equalization (CLAHE)
p{9,1}='CLAHE size';                    p{9,2}=25;      % CLAHE window size


% Projection %
p{19,1}='nFitPoints';                   p{19,2}=1;      % No of frames +/- from peak considered in calculation of mean and variance
                                                        % (0 = only peak frame is used)

p{18,1}='MaxStdev';                     p{18,2}=Inf;      % Maximum standard deviation of intensity peak before it is rejected (useful for mi02 and other non-ZO marker)
                                                        % Value should roughly be the thickness of marker in frame number (Inf = never reject)

p{12,1}='Remove Speckles';              p{12,2}=1;      % Whether to remove points with large z value deviation from the neighborhood
p{13,1}='Z threshold';                  p{13,2}=4;      % z deviation threshold for removal
p{14,1}='Remove speckles strel size';   p{14,2}=25;     % strel size for imopen smoothing (~ max size of speckles that can be removed)


% Postprocessing %
p{15,1}='Output backgrd compensation';  p{15,2}=1;      % Whether to do background compensation/equalization on output image
p{16,1}='Background comp size';         p{16,2}=50;     % Size for calculating background compensation (imclose)

p{17,1}='Output imadjust';              p{17,2}=0;      % Whether to adjust intensity of output image
```

```
84
86 fsize = 10;              % filter size (must be odd integer)
   fvar = 2;               % filter variance
88 nProjectAvg = 1;    % no of slices to be averaged above and below mean

90 %% extract ZO channel from stack S
   tic
92
   [row,col,~] = size(S{1});
94 nStack = length(S);
   ZO = zeros(row, col, nStack);
96 mi02 = zeros(row, col, nStack);

98 if nargin == 1
       % If input is just one stack, extract ZO and mi02 from different color
100    % channels
       for i = 1:nStack
102        ZO(:,:,i) = S{i}(:,:,p{1,2});
           mi02(:,:,i) = S{i}(:,:,p{2,2});
104    end
   else
106    % else if given as 2 separate stacks, simply convert them to cell array
       ZO = cell2mat( permute(S,[2 3 1]) );
108    if ~isempty(Smi02)
           mi02 = cell2mat( permute(Smi02,[2 3 1]) );
110    else
           mi02 = ZO;
112    end
   end
114
   %% Image Preprocessing
116
   % Apply wiener2 eliminate noise before max projection
118 if p{3,2} == 1
       disp('Pre-process: wiener filter...')
120    ZOblur = zeros(size(ZO));
       for i = 1:nStack
122        ZOblur(:,:,i) = wiener2(ZO(:,:,i), [p{4,2} p{4,2}]);
       end
124 else    ZOblur = ZO;
   end
126 % Maximum projection
   ZOmax = double(max(ZOblur,[],3));
128 ZOmax = ZOmax - min(min(ZOmax));
   ZOmax = ZOmax ./ max(max(ZOmax));
130 %ZOmax = imadjust(ZOmax);

132 % Entropy filter to mask out background
   if p{10,2} == 1
134    disp('Pre-process: entropy filter to mask background...')
       [bgmMask, texture] = Separate_ROI_from_background(ZOmax, 0, p{11,2});
136    ZOmax(~bgmMask) = 0;
       ZOmax = imadjust(ZOmax);
138 else
```

```
    bgmMask = ones(size(ZOmax));
    texture = NaN(size(ZOmax));
end

% Background compensation
bgm = imclose(ZOmax, strel('disk', p{7,2}));
scale = max(max(bgm)) ./ bgm;
scale(isinf(scale)) = 1;    % background was set to Inf
scale(~bgmMask) = 0;
if p{6,2} == 1
    disp('Pre-process: background compensation...');
    ZOmax = ZOmax .* scale;
end
ZOmax(~bgmMask) = 0;

% CLAHE
if p{8,2} == 1
    disp('Pre-process: CLAHE...');
    nTiles = floor( size(ZOmax) ./ p{9,2} );
    ZOmax = adapthisteq(ZOmax, 'NumTiles', nTiles);
end
ZOmax(~bgmMask) = 0;

%% Get pixels with fairly bright ZO signal

% Easy way is to threshold the ZO maximum projection with fairly
% conservative threshold.
ZOthreshold = p{5,2};
if ZOthreshold == 0
    ZOthreshold = graythresh(ZOmax);
end
ZOthresh = im2bw(ZOmax, ZOthreshold);
[row_px, col_px] = find(ZOthresh);     % find nonzero pixels
npixel = length(row_px);     % no of nonzero pixels

% for each nonzero pixel, collect the ZO intensity vs. z-position to a
% vector ZOintensities.
ZoIntensities = zeros(npixel, nStack);
for i = 1:npixel
    ZoIntensities(i,:) = reshape( ZOblur(row_px(i),col_px(i),:), 1, nStack );
end

%% Calculate mean and variance (fit to Gaussian)

% Find peaks/maxima for each pixel
[~, maxPos] = max(ZoIntensities, [], 2);

% Mean & variance of Gaussian
average = zeros(npixel,1);
variance = zeros(npixel,1);

nFitPoints = p{19,2};
disp('Finding peaks in intensity...')
for i = 1:npixel
    % Get starting and ending indices of z-slices included in fitting
```

```
    startPos = maxPos(i) - nFitPoints;
    endPos = maxPos(i) + nFitPoints;

    % Include cases where not all maxPos +/- nFitPoints slices are
    % available in the image stack
    if startPos < 1
        startPos = 1;
    end
    if endPos > nStack
        endPos = nStack;
    end

    r = startPos:endPos;

    IntTemp = ZoIntensities(i, r);
    IntTemp = IntTemp ./ sum(IntTemp);    % normalize
    product1 = r.*IntTemp;
    averageTemp = sum(product1);
    average(i) = averageTemp;
    variance(i) = sum(r.*product1) - average(i)^2;

    % If variance is greater than MaxStdev^2, reject data and set both average
    % and variance to zero
    if variance(i) > p{18,2}^2
        average(i) = 0;
        variance(i) = 0;
    end
end

%% Put mean and variance into a matrix of the size of the image

zpos_mean = zeros(row,col);
zpos_var = zeros(row,col);
for i = 1:npixel
    zpos_mean(row_px(i),col_px(i)) = average(i);
    zpos_var(row_px(i),col_px(i)) = variance(i);
end

%% Remove Speckles
% Speckles can be identified by looking at curvature smoothness, i.e. when
% the Z-position of a pixel is very different from the surrounding values
% then it is likely to be a speckle/dust.
% A fast way to get the z-value of the neighborhood is to do morphological
% opening. (Ideally we'd like to do meadian, but it is hard/slow to do with
% losts of missing data like in our case).
if p{12,2} == 1
    disp('Removing speckles...')

    m1up = zpos_mean;                                    % 2 versions: one removes
    speckles above, and the other one below
    m1dn = zpos_mean;
    mask1 = m1dn==0;

    m1dn(mask1) = max(max(m1dn));                       % down: replace zeros with max
    before applying imopen
```

```
248     m1up = imclose(m1up, strel('disk', p{14,2}));       % up: replace values with max
        of the neighborhood
        m1dn = imopen(m1dn, strel('disk', p{14,2}));        % down: replace values with min
         of the neighborhood
250
        m2dn = abs(zpos_mean - m1dn);                      % deviation from neighborhood
252     m2up = abs(zpos_mean - m1up);
        m2dn(mask1) = 0;
254     m2up(mask1) = 0;

256     maskSpeckles = (m2dn > p{13,2}) | (m2up > p{13,2});    % find deviation greater
        than p{13,2}

258     zpos_mean(maskSpeckles) = 0;                    % set those to zero

260 end

262 %% Fill gap and smoothen using Gaussian filter

264 % convert NaN's back to zero, so when multiplied with the filter it won't
    % make any contribution
266 disp('Constructing smooth z surface...')
    mask = isnan(zpos_mean);
268 zpos_mean(mask) = 0;
    zpos_var(mask) = 0;
270
    zpos_nnz = double(zpos_mean > 0);       % to calculate weight, ignorning missing data
272
    % Fill gap using big gaussian filter
274 fgauss = fspecial('gaussian', [100 100], 10);
    fval = imfilter(zpos_mean, fgauss, 'replicate');
276 fnonzero = imfilter(zpos_nnz, fgauss, 'replicate');
    fval = fval./fnonzero;
278
    mask = zpos_mean == 0;
280 zpos_mean(mask) = fval(mask);

282 % Smoothen usiing gaussian filter (specified in parameter setting)
    if mod(fsize,2) == 0
284     fsize = fsize + 1;
    end
286 fgauss = fspecial('gaussian', [fsize fsize], fvar);
    zpos_mean = imfilter(zpos_mean, fgauss, 'replicate');
288
    zpos_mean(~bgmMask) = 0;
290 zpos_double = zpos_mean;
    zpos_mean = uint8(zpos_mean);
292
    %% Project mi02 and ZO signal
294
    % Get mi02 signal from z-slice obtained from the mean (zpos_mean)
296 % !!! Future: do weighted average of a few slices based on zpos_var !!!

298 disp('Projecting images based on z surface...')
```

```
if nProjectAvg > nFitPoints
    error('nProjectAvg cannot be bigger than nFitPoints')
end
mi02_projection = zeros(row,col);
ZO_projection = zeros(row,col);
x = [-nProjectAvg:nProjectAvg];

% Calculate weight from gaussian with variance equals to mean variance
meanVar = mean(zpos_var(zpos_var>0));
if (meanVar == 0) || isnan(meanVar)
    meanVar = 1;
end
weight = exp(-1*x.^2/(2*meanVar));

for i = 1:nStack
    mi02Temp = zeros(row,col);
    ZOTemp = zeros(row,col);
    mask = zpos_mean == i;      % pixels that have mean at position i
    weightCum = 0;              % cumulative sum of weight, for normalization

    for j = 1:length(x)
        k = i - x(j);       % k is the current z-slice position

        % If slice is outside stack, continue/break
        if (k < 1) || (k > nStack)
            continue
        end

        mi02Slice = double(mi02(:,:,k));
        ZOSlice = double(ZO(:,:,k));
        mi02Temp(mask) = mi02Temp(mask) + mi02Slice(mask) .* weight(j);
        ZOTemp(mask) = ZOTemp(mask) + ZOSlice(mask) .* weight(j);
        weightCum = weightCum + weight(j);      % cumulative sum of weight
    end

    % normalize and store
    weightCum(weightCum==0) = 1;
    mi02_projection(mask) = mi02Temp(mask) ./ weightCum;
    ZO_projection(mask) = ZOTemp(mask) ./ weightCum;
end

temp1 = min(ZO_projection(bgmMask));
temp2 = min(mi02_projection(bgmMask));
ZO_projection(~bgmMask) = temp1;
mi02_projection(~bgmMask) = temp2;

ZO_projection = ZO_projection - min(min(ZO_projection));
ZO_projection = ZO_projection ./ max(max(ZO_projection));
mi02_projection = mi02_projection - min(min(mi02_projection));
mi02_projection = mi02_projection ./ max(max(mi02_projection));

%% Post-processing before output

% Background subtraction
if p{15,2} == 1
```

```
    disp('Post-process: background subtraction...')
    bgm = imclose(ZO_projection, strel('disk', p{16,2}));
    scale = max(max(bgm)) ./ bgm;
    %fs = fspecial('average', 2*p{7,2});
    %scale = imfilter(scale, fs, 'replicate');     % smoothen
    scale(isinf(scale)) = 1;
    scale(~bgmMask) = 0;

    mi02_projection = mi02_projection .* scale;
    ZO_projection = ZO_projection .* scale;

    % Clip values higher than 1
    mi02_projection(mi02_projection>1) = 1;
    ZO_projection(ZO_projection>1) = 1;
end

% Convert to uint8/uint16 before output
ZOmax = max(double(ZO),[],3);
ZOmax = ZOmax./max(max(ZOmax));

ZO_projection = ZO_projection./max(max(ZO_projection));
mi02_projection = mi02_projection./max(max(mi02_projection));

img = S{1};
img_info = whos('img');
imclass = img_info.class;

if strcmp(imclass, 'uint8')
    mi02_projection = im2uint8(mi02_projection);
    ZO_projection = im2uint8(ZO_projection);
    ZOmax = im2uint8(ZOmax);
elseif strcmp(imclass, 'uint16')
    mi02_projection = im2uint16(mi02_projection);
    ZO_projection = im2uint16(ZO_projection);
    ZOmax = im2uint16(ZOmax);
end

% Adjust intensity
if p{17,2} == 1
    mi02_projection = imadjust(mi02_projection);
    ZO_projection = imadjust(ZO_projection);
    ZOmax = imadjust(ZOmax);
end

disp('DONE!')
toc
```

codes/Estimate_OLM_From_ZO.m

A.2.2 Separate_ROI_from_background.m

```
function [MaskOut, texture] = Separate_ROI_from_background(ImageIn, showHistogram,
    thresh)

%%%%%%%%%%%%%%%%%%%%%%%%%%%%%%%%%%%%%%%%%%%%%%%%%%%%%%%%%%%%%%%%%%%%%%%%%%%%%%%
% Function to identify and extract region of interest in an image (i.e.
% region with cells) from the background (i.e. region without cells) using
% entropy filtering.
% Regions with high entropy (high dynamic range of pixel intensity) usually
% contain signals, whereas region with low entropy (uniform intensity +
% noise) are usually background.
%
% ImageIn = grayscale input image
% showHistogram = whether to show histogram of entropy
% thresh = entropy threshold between signal and background
%
% MaskOut = binary mask, 1 = region of interest (with cells) and 0 =
% background
% texture = entropy of ImageIn
%
% Free parameters:
%   thresh (set in Estimate_OLM_From_ZO.m)
%
% Procedures:   1. Noise reduction
%               2. Background subtraction (to correct for uneven
%               illumination)
%               3. CLAHE
%               4. Texture analysis (e.g. entropy filter)
%               5. Thresholding to obtain binary mask
%               6. Postprocessing
%
%
% Created by Jeremy Hadidjojo (hjeremy@umich.edu), 04/29/15
%
%%%%%%%%%%%%%%%%%%%%%%%%%%%%%%%%%%%%%%%%%%%%%%%%%%%%%%%%%%%%%%%%%%%%%%%%%%%%%%%


%% Parameters

% structuring element sizes
strelSize1 = 25;        % for imopen to get background intensity
strelSize2 = 75;        % for imopen in post-processing to remove small isolated
    patches in MaskOut
strelSize3 = 25;        % for imclose in post-processing to remove small gaps in
    MaskOut
strelSize4 = 10;        % for imerode to erode/tighten up the mask
strelSize5 = 0;        % for imdilate to enlarge the mask

ClaheTiles = 32;        % Number of tiles for CLAHE
entropyFilterSize = 21; % size of square neighborhood for entropy filter (must be odd)


%% 1. Noise reduction

```

```
M = im2uint8(imadjust(ImageIn));
M = wiener2(double(M));

%% 2. Backgroud subtraction

bgm = imopen(M, strel('disk', strelSize1));
M = M - bgm;

% normalize to [0,1]
M = M - min(min(M));
M = M ./ max(max(M));

%% 3. CLAHE

M = adapthisteq(M, 'NumTiles', [ClaheTiles ClaheTiles]);
% normalize to [0,1]
M = M - min(min(M));
M = M ./ max(max(M));

%% 4. Texture filter
% Currently entropy filter is used. It works fine but a little bit slower.
% Alternatively it can be replaced with e.g. stdfilt or other texture
% filtering.

t = entropyfilt(M, ones(entropyFilterSize));
% normalize to [0,1]
t = t - min(min(t));
t = t ./ max(max(t));

%% 5. Tresholding
% Currently threshold is obtained by Otsu's method. This works fine for the
% images that I have analized, but if it doesn't one can always pick the
% threshold in a different way (e.g. local minima in histogram curve,
% k-means, manual threshold, etc.)

% Set zeros to NaN, so it will not bias thresholding value when an image
% has significant of 'black' region.
t(t==0) = NaN;

if nargin < 3 || thresh == 0
    thresh = graythresh(t);
end
t1 = im2bw(t, thresh);

if showHistogram
    figure
    hold on
    hist(t(:), 100);
    y0 = ylim;
    plot([thresh thresh], y0, 'r')
    hold off
end

%% 6. Post-processing
```

```
% fill holes
t1 = imfill(t1, 'holes');
% Clean up small isloated patches
t1 = imopen(t1, strel('disk', strelSize2));
% Remove small gaps
t1 = imclose(t1, strel('disk', strelSize3));
% Erosion to shrink the mask slightly
t1 = imerode(t1, strel('disk', strelSize4));
% Erosion to shrink the mask slightly
t1 = imdilate(t1, strel('disk', strelSize5));

MaskOut = t1;
if nargout == 2
    texture = t;
end
```

codes/Separate_ROI_from_background.m

A.3 Analysis of Laser Ablation Experiment on Zebrafish Retina

A.3.1 EstimatePlaneInclination.m

```
function [w, b, theta, rmse] = EstimatePlaneInclination(X_3d)

%%%%%%%%%%%%%%%%%%%%%%%%%%%%%%%%%%%%%%%%%%%%%%%%%%%%%%%%%%%%%%%%%%%%%%%%%%%%
% Find least square fit of plane to zpos at coordiates given in X.
% Assuming 2D plane equation of z = w'*x + b, where w and b are the
% gradient and offest vectors, respectively. Then from w calculate the
% direction and angle of tilt.
%
% X_3d: 3D coordinate of cells (see EstimateTransformation.m)
%
% No free parameter.
%
%   Jeremy Hadidjojo (hjeremy@umich.edu), 2016
%
% List of changes:
%       - initial version
%%%%%%%%%%%%%%%%%%%%%%%%%%%%%%%%%%%%%%%%%%%%%%%%%%%%%%%%%%%%%%%%%%%%%%%%%%%%

X = X_3d(:,1:2);
Z = X_3d(:,3);

%% Least Square Fitting

%%%
% Augmented coordinates are defined as follow:
%       xtil = [1, x, y]'
%       Xtil = [xtil_1, xtil_2, ..., xtil_n]
%       wtil = [b, w1, w2]'
%%%

n = size(X,1);
Xtil = cat(1, ones(1,n), X');
XXt = Xtil * Xtil';
wtil = XXt \ Xtil * Z;          % wtil = (Xtil*Xtil')^-1 * Xtil * Z

b = wtil(1);
w = wtil(2:3);

if nargout > 2
    theta = atand(norm(w));
end

%% Calculate root mean square error
Z_predict = w'*X' + b;
Z_error = Z_predict' - Z;
```

```
46 rmse = sqrt(sum(Z_error.^2));
```

codes/EstimatePlaneInclination.m

A.3.2 EstimateTransformation.m

```
function [b,M,D,theta1,theta2,anis,rmse_def] = EstimateTransformation(X,Y,zposX,zposY,
    zscale, writeToFile)

% Find 2D least square transformation between X and Y.
% Assuming transformation is homogeneous and can be written as Y = M*X + b,
% for some 2x2 matrix M and 1x2 vector b.

%%%%%%%%%%%%%%%%%%%%%%%%%%%%%%%%%%%%%%%%%%%%%%%%%%%%%%%%%%%%%%%%%%%%%%%%%%%%%%%
% X, Y          = n-by-2 data matrices
% Xtil, Ytil    = n-by-3 augmented data matrices, obtained by padding the
%                 first column of X/Y with ones.
% zposX         = 2D matrix of surface depth (obtained from output of
%                 Estimate_OLM_From_ZO.m)
% zscale        = ratio of the pixel size along z axis to x axis. Pixel
%                 size on x and y axis are assumed equal. To obtain this
%                 value, check metadata on raw '.lif' files and look for
%                 voxel size.
%                 (zscale = 1.8/0.095 for the images we analyzed)
% writeToFile   = (true/false) whether to write analysis result as
%                  'DeformationAnalysis.txt' in working directory.
%
% Free parameter:
%   zscale (default 1.8/0.095, but depends on microscope aquisition
%           parameter -- see metadata in '.lif' file)
%
%
% M and b are 2-by-2 and 1-by-2 transformation matrix and vectors,
% respectively, such that given X, the predicted Y is Ypredict = X*M + b.
% Mtil is augmented M, obtained by inserting b above M (ie Mtil = [b; M]).
% In terms of Mtil, we can write the above as Ypredict = Xtil*Mtil.
%
%
% Created by: Jeremy Hadidjojo (hjeremy@umich.edu), 10/16/15
%
% Last modified:
%       - JH 05/21/16: added output: root mean squared error
%       - JH 08/30/16: fit planes through points and correct for tilt by
%                      rotating to plane of focus
%
%%%%%%%%%%%%%%%%%%%%%%%%%%%%%%%%%%%%%%%%%%%%%%%%%%%%%%%%%%%%%%%%%%%%%%%%%%%%%%%


%% Estimate tilt plane and correct

% create 3D coordinates from X and Y by using height information from zposX
% and zposY
[row,col] = size(zposX);
X_2d = round(X);
Y_2d = round(Y);

indX = sub2ind([row,col], X_2d(:,1), X_2d(:,2));      % convert to linear indices
indY = sub2ind([row,col], Y_2d(:,1), Y_2d(:,2));
```

```
heightX = zposX(indX) * zscale;
heightY = zposY(indY) * zscale;

X_3d = cat(2, X, heightX);
Y_3d = cat(2, Y, heightY);

% Fit plane to data points
[wX, ~, thX, rmseX] = EstimatePlaneInclination(X_3d);
[wY, ~, thY, rmseY] = EstimatePlaneInclination(Y_3d);

% make wX and wY 3D vectors and normalized
wX(3) = sum(wX.^2);
wX = wX ./ norm(wX);
wY(3) = sum(wY.^2);
wY = wY ./ norm(wY);

% Axis of rotation kX and kY are just cross product between z_hat and w_hat
z_hat = [0, 0, 1]';
kX = cross(z_hat, wX);
kY = cross(z_hat, wY);

% normal vector of the planes
nX = cross(wX, kX);
nX = nX ./ norm(nX);
nY = cross(wY, kY);
nY = nY ./ norm(nY);

% angle of rotation
thetaX = acosd( dot(nX, z_hat) );
thetaY = acosd( dot(nY, z_hat) );

% Rotation matrices using Rodrigues formula
%       R = I + sin(theta)*K + (1-cos(theta))*K^2
%       where K is the matrix cross product of rotation axis k
K_X = [0, -kX(3), kX(2); ...
       kX(3), 0, -kX(1); ...
       -kX(2), kX(1), 0];

K_Y = [0, -kY(3), kY(2); ...
       kY(3), 0, -kY(1); ...
       -kY(2), kY(1), 0];

R_X = eye(3) + sind(thetaX)*K_X + (1-cosd(thetaX))*K_X*K_X;
R_Y = eye(3) + sind(thetaY)*K_Y + (1-cosd(thetaY))*K_Y*K_Y;

% Apply rotation to X_3d and Y_3d. After rotation the planes of X and Y
% should now be parallel to microscope's plane of focus.
X_3d_rot = R_X * X_3d';
Y_3d_rot = R_Y * Y_3d';
X_3d_rot = X_3d_rot';
Y_3d_rot = Y_3d_rot';

% Extract just the 2D component for deformation analysis
X = X_3d_rot(:,1:2);
Y = Y_3d_rot(:,1:2);
```

```
%% Least square fitting
% Solution to least square: Mtil = (Xtil'*Xtil)^(-1) * Xtil'*Ytil
% Remember once we have Mtil, prediction Ypredict given X can be easily
% computed: Ypredict = X*M + b = Xtil*Mtil.

n = size(X,1);
% Create augmented vector Xtil
Xtil = cat(2, ones(n,1), X);
N = Xtil' * Xtil;

% Least square regression of Mtil
Mtil = ( Y'*Xtil/N )';

M = Mtil(2:end,:);
b = Mtil(1,:);

%% Polar decomposition

% Polar decomposition: M = U*P
% where U is unitary, P is PSD hermitian
% i.e. decompose M into on-axis deformation P and rotation U
P = (M'*M)^(1/2);
U = M/P;

% Rotation angle from U, in degrees
theta1 = atan2d(U(2,1), U(1,1));

% Spectral decomposition of P
[V,D] = eig(P);

% Strain anisotropy: difference between strain along both axes
anis = 2*( (D(2,2)-D(1,1))/trace(D) );

% Angle of principal axes from x and y
theta2 = atand(V(2,1)/V(1,1));

%% Calculate root mean squared error

Yp = Xtil*Mtil;         % predicted Y for given X
ydif2 = (Y - Yp).^2;    % subtract from actual value of Y
rmse_def = sqrt( mean( sum(ydif2,2) ) );

% %% Calculate apparent compression due to change in plane tilt angles
%
% if nargin > 2
%     [wX, ~] = EstimatePlaneInclination(zposX, X, zscale);
%     [wY, ~] = EstimatePlaneInclination(zposY, Y, zscale);
%
%     axisX = atan2d(wX(2), wX(1));
%     th = atan2d(wX(1), wX(2));
%     axisY = atan2d(wY(2), wY(1));
%
%     thetaX = atand(norm(wX));
%     thetaY = atand(norm(wY));
```

```
%
%     compression = cosd(thetaY)/cosd(thetaX);
%
%     M = [compression, 0; 0, 1];
%     R = [cosd(th), -sind(th); sind(th), cosd(th)];
%     M1 = R*M*R'
%
%     fprintf('wX = (%.2f,%.2f); thetaX = %.2f deg; tilt axis = %.2f deg\n', wX(1), wX
    (2), thetaX, axisX)
%     fprintf('wY = (%.2f,%.2f); thetaY = %.2f deg; tilt axis = %.2f deg\n', wY(1), wY
    (2), thetaY, axisY)
%     fprintf('Compression due to tilt (assume both axes are the same): %f\n',
    compression)
%     fprintf('CompressionX : %f, compressionY : %f\n', M1(1,1), M1(2,2))
% end

%% Write to file
if writeToFile == 1
    filename = 'DeformAnalysis.txt';
    fid = fopen(filename, 'w');
    count = 0;
    while fid == -1
        count = count + 1;
        filename = ['DeformAnalysis', num2str(count), '.txt'];
        fid = fopen(filename, 'w');
    end

    rmse_plane = max(rmseX,rmseY);

    fprintf(fid, 'No of pts \t x-principal strain \t y-principal strain \t Principal
    axes angle \t Principal strain anisotropy \t RMSE deformation \n');
    fprintf(fid, '%d \t %f \t %f \t %f \t %f \t %f \t %f \n', n, D(1,1), D(2,2), theta2
    , anis, rmse_def, rmse_plane);

    fclose(fid);

end
```

codes/EstimateTransformation.m

APPENDIX B

Additional Methods for Chapter 4: Correlation Analysis of Morphogenetic Noise

This Appendix gives details on several unsuccessful attempts in analyzing the correlated noise of *Drosophila* notum. Though we ended up not using the methods below, we spent quite a bit of time on it and learned something useful, hence the rationale of documenting them. The following materials are supplemental to the main text found in Chapter 4 and are not essential in understanding the main story. Readers are suggested to first read that chapter, and go to the following sections only when prompted by the main text.

B.1 Particle Image Velocimetry (PIV) as alternative to cell segmentation and tracking

In Section 4.3, we found non-trivial correlation between the two halves of the full-notum movie. We would like to perform the analysis on more movies containing both sides of the notum. Segmenting such movies, however, requires very significant manual effort. Hence we were looking for ways to extract velocity fields without directly segmenting the cells. Particle image velocimetry (PIV) does exactly that.

PIV infers displacement of some features between two images taken at a short time apart. It is initially developed to infer flow fields of a fluid with high density of injected tracer particles [119,120]. Due to the high density, tracking individual particles is no longer possible. Flow fields are instead inferred by matching shifted patterns between two images.

Conventional PIV works by first chopping the initial image into small windows. For each of these windows, it then tries to find the best match on the second image by means of correlation. The displacement of this window is then simply the difference of the initial and the matched positions. By repeating this over all windows, one can obtain the displacement field between the two images. In practice, not all windows will produce reliable

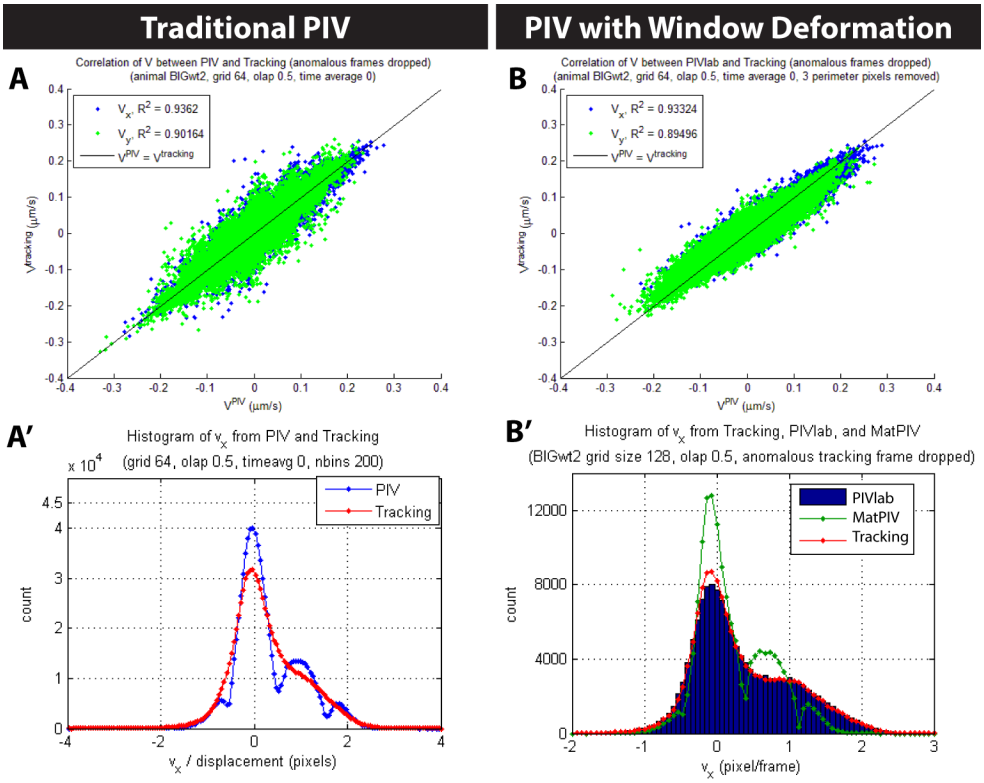

Figure B.1: **Comparison between traditional and window-deforming PIV.** Traditional PIV without window deformation (A-A') shows poor correlation with tracking (A) and strong 'peak-locking' (i.e. tendency to result in integer displacements, A'). Using more advanced window-deforming PIV improves correlation with cell tracking slightly (B) and eliminates peak-locking (B').

displacement. Various filterings are employed to identify possible matching errors, where values are then extrapolated from the surrounding, more reliable ones [119–122].

To infer velocity fields from the movies, we applied PIV on E-Cadherin:GFP fluorescence intensity images. We use a freely-available MATLAB-based software called MatPIV to perform the core PIV computations [123, 124]. The software was modified slightly to make it work with existing algorithms developed by Guirao *et. al.* and to ensure the PIV windows are identical to the averaging windows of cell tracking. At a glance, it works very well, producing velocity fields that are qualitatively very similar to cell tracking[1]. However, upon closer examination it is clear that the PIV velocities do not correlate very well with the average velocities from cell tracking (Figure B.1 A). Furthermore, the PIV velocities show clear 'peak-locking' (Figure B.1 A'). It refers to a behavior where classical PIV displacements are biased towards integer values due to discreteness of the pixels, and is

[1] In fact, cell tracking algorithm developed by Guirao *et. al.* uses PIV information as a guide for tracking the cells [118].

well-documented in the PIV community [121, 122].

To eliminate peak-locking, we used a more sophisticated PIV algorithm that allows deformation of the windows in addition of translations. This is done iteratively, where in the first iteration the windows are simply translated without deformation. In subsequent iterations, however, the windows are not only translated but also deformed based on the previous displacement field. This process is repeated until some convergence criteria is met. We used another freely-available, MATLAB-based package called PIVlab (again, modified to make it work with existing codes) to perform PIV with window deformation [125–127].

Figure B.1 B-B' shows the improvement obtained by using window-deformation PIV. Notably, the velocity histogram in panel B' shows no sign of peak-locking and it matches the histogram from cell tracking pretty well. However, panel B shows that the correlation between PIV and tracking velocities is still not good enough.

We think that this discrepancy is due to the fundamental difference between cell tracking and PIV. In cell tracking, velocities are given in terms of the position of cell centroids. In PIV, however, the velocity depends on image correlation of the size of the PIV window (typically between 32×32 and 128×128). In addition, PIV is also more sensitive to changes in cell membranes (since it is directly working on the E-Cadherin:GFP intensity). It is thus unclear to us how the PIV velocities are related to that of cell tracking, and what correlation of the former would mean physically. Hence we decided to abandon the PIV approach and stick to cell tracking whenever we can.

B.2 Subtracting morphogenesis flow using across-animal averages

In our study of hemi-notum movies (Section 4.4), we had difficulties separating noise from morphogenesis movements. As the pupa transforms into an adult fly, the dorsal notum epithelium undergoes stereotypical remodeling that is qualitatively the same across different animals. One example is the flow of cells towards the head that begins at around 24 hAPF and coincides with an invagination between the notum and the head that will eventually form the adult neck. Since these morphogenetic movements are necessarily correlated between left and right, we have to completely remove this flow before we can quantify noise correlation. Failing to remove this morphogenesis movement completely will clearly produce undesired correlations. For the full-notum, we can achieve this subtraction by taking velocity differences between the left and right halves. This is not possible with hemi-nota movies.

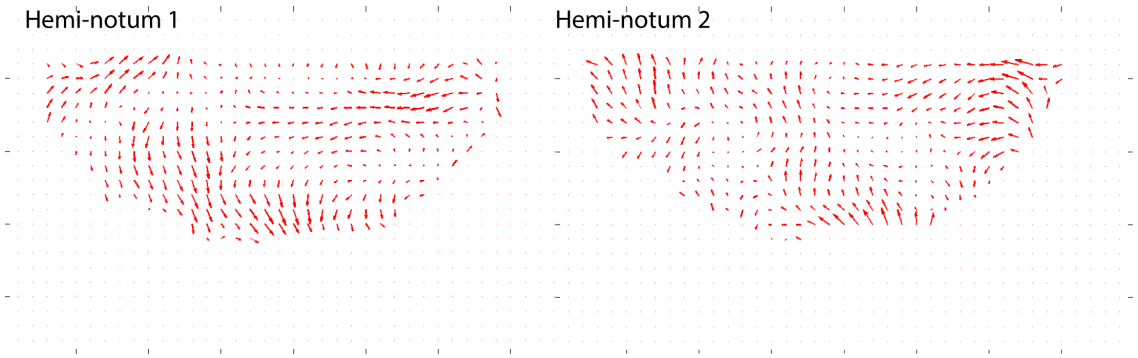

Figure B.2: **Correlated velocities remain after archetype subtraction.** Shown are two archetype-subtracted velocity fields from different hemi-nota movies. Both fields are calculated at 18 hAPF, and are representative of the other three hemi-nota. The remainder velocities are highly-correlated and do not resemble noise at all. Although all wildtype flies share the same stereotypical notum morphogenesis, different individuals also have unique slight variations that are not captured by the archetype model.

We came up with an idea to eliminate the morphogenetic movements using across-animal averages. This idea originated from our discussions with the people in the Bellaïce lab as they try to construct stereotypical picture of notum morphogenesis. Termed the 'archetype' model, it is obtained by averaging cell movements across different animals after proper space and time registration [118]. We obtained the archetype flow from their analysis published in [118]. We hoped that subtracting the archetype flow will eliminate the morphogenetic movements and leave us only with the noise we are interested in.

Figure B.2 shows the velocity field obtained by subtracting the archetype flow from two hemi-notum velocity fields. One can immediately see a problem there: the remainder velocity fields are highly-correlated and do not look like noise at all. This is precisely due to interanimal variations. Although all wildtype flies share common qualitative morphogenesis, no two individuals are exactly the same when it comes to precise quantitative measurement. The archetype flow captures the features common across different animals, but one should not expect this to precisely match the morphogenesis movement of a specific individual.

At the same time, this highlights the inherent difficulty in extracting the noise from just half of the notum. The problem is precisely that we do not have a good way to know and subtract the morphogenetic flow from the observed cell movements. As the reader will see when reading the rest of the story in Section 4.4, this is the problem we encounter over and over again. Thus, we believe that the best way to address the correlated noise we found in Section 4.3 is to analyze both left and right hemi-nota from the same animals.

APPENDIX C

2017 Nature Communications Manuscript: Anisotropic Glial Scaffolding Shapes a Multiplex Photoreceptor Mosaic in Zebrafish Retina

Mikiko Nagashima[1], Jeremy Hadidjojo[2], Linda K. Barthel[3], David K. Lubensky[2*], Pamela A. Raymond[1*]

[1]Department of Molecular, Cellular, and Developmental Biology, [2]Department of Physics, [3]Microscopy and Image Analysis Laboratory, University of Michigan, Ann Arbor, MI USA

[*]**Co-Corresponding authors:**

Pamela A. Raymond, Ph.D.
Department of Molecular, Cellular, and Developmental Biology
830 North University Avenue
Ann Arbor, MI 48109-1048
praymond@umich.edu

David K. Lubensky, Ph.D.
Department of Physics
450 Church Street
Ann Arbor, MI 48109-1040
dkluben@umich.edu

Keywords: Photoreceptors, Müller glia, Cell patterning, Epithelial tension, Retina

Abstract

Regularly spaced, homotypic neuronal mosaics are characteristic of the vertebrate retina, but the lack of correlation between different cell types suggests an absence of heterotypic interactions. The teleost cone photoreceptor mosaic is a unique exception: in zebrafish, Red, Green, Blue, and UV cones organize into a crystalline array with defined, neighbor relationships, but mechanisms patterning this multiplex mosaic are not understood. Live imaging of the growing retinal margin in transparent juvenile zebrafish with cell-specific, fluorescent reporters revealed parallel bands of N-cadherin-stabilized Müller glial apical processes and a precise spatial arrangement of Red and UV cones at the onset of differentiation, prior to expression of planar polarized adhesion and packing into single cell width columns. Laser ablation of Müller glia revealed that they support anisotropic mechanical tension in the retinal epithelium. We conclude that mechanical forces acting through glial scaffolding contribute to formation and maintenance of the multiplex photoreceptor mosaic.

Introduction

A defining characteristic of the nervous system is its modular architecture, with precise spatial segregation and regular arrangement of cellular components and circuits. The vertebrate retina is an exceptionally clear example of this organizational property (Cook and Chalupa, 2000; Eglen, 2006; Galli-Resta et al., 2008; Hoon et al., 2014). The retina is a specialized neural epithelium comprised of six major types of neurons stratified into distinct layers (Dowling, 2012). Within each cellular layer, most types of retinal neurons are arranged in evenly spaced arrays, called mosaics, which effectively 'tile' the retinal surface and allow for systematic and complete sampling of the visual space (Wässle and Riemann, 1978). Surprisingly, the mosaic distributions of different types of retinal neurons are independent and uncorrelated (Cameron and Carney, 2004; Kram et al., 2010; Rockhill et al., 2000). The cellular mechanisms that assemble these homotypic retinal cell mosaics include tangential cell dispersion in response to repulsive, local, cell-cell interactions among like-cell types (Galli-Resta et al., 1997; Reese and Galli-Resta, 2002), and in some cases, selective cell death (Galli-Resta et al., 2008). The result is creation of an 'exclusion zone' around individual neurons, which is sufficient to explain the regular mosaic spacing (Galli-Resta et al., 1999).

The only example of correlated heterotypic cell spacing in the neural retina is in teleost fish, where different cone spectral subtypes are arranged into precise crystalline lattice arrays (Engström, 1963; Lyall, 1957; Marc and Sperling, 1976). These multiplex cone mosaics, which exhibit a diversity of patterns across fish species, are a unique teleost feature not seen in cone photoreceptors in other vertebrate retinas, *e.g.* birds (Kram et al., 2010) or primates (Marc and Sperling, 1977; Wikler and Rakic, 1991). Clearly, the mechanisms that pattern homotypic mosaics are insufficient to explain teleost cone mosaic arrays, which have intriguing similarities to the *Drosophila* compound eye (Raymond and Barthel, 2004; Rister and Desplan, 2011). We have very limited knowledge of the organizational strategies that build the teleost cone mosaic and not even the most basic information about how cell fate determination, spatial arrangement, and cell packing are coordinated during formation of these heterotypic lattice arrays.

In zebrafish four spectrally and morphologically distinct cone photoreceptor subtypes (Red, Green, Blue, and Ultraviolet, UV) are organized at the apical retinal surface into a rectangular lattice consisting of a repeated motif of 12 cells in a precise ratio of 4 Red : 4 Green : 2 Blue: 2 UV (Salbreux et al., 2012). Rows of Blue and UV single cones alternate with rows of Red and Green double cone pairs that radiate outward from the optic disc, and in the orthogonal planar dimension, single-cell-wide columns of cones display an internal, reiterative, mirror image symmetry that includes all four subtypes (Fig. 1A-C). Rod photoreceptors also have specified positions in the lattice (Fadool, 2003) and are preferentially inserted between cone columns, a territory also occupied by thin processes extended from Müller glial cells whose bodies remain below the photoreceptor layer (Salbreux et al., 2012). This regular lattice array is a feature only of the adult zebrafish retina; cone photoreceptors in the embryonic and early larval retina are evenly spaced in homotypic mosaics, but lack the heterotypic lattice pattern (Allison et al., 2010). The majority of cells in the adult fish retina are generated by persistent neurogenesis from proliferating retinal progenitors located in a circumferential germinal zone at the retinal margin (Allison et al., 2010; Centanin et al., 2011; Raymond et al., 2006), which creates cohorts of cones that organize into single-cell-width columns parallel to the growing margin [Fig. 1C and (Allison et al., 2010; Raymond and Barthel, 2004; Salbreux et al., 2012)].

As in all epithelia, the apical surface of the vertebrate retina (known as the outer limiting membrane, OLM) is stabilized by zonula adherens junctions, which are unusual in the retina because they include both heterotypic intercellular adhesions between photoreceptors and Müller glia and homotypic adhesions between Müller glia (Williams and Arikawa, 1990). These specialized intercellular junctions contain the classical Ca^{++}-dependent homophilic cell adhesion molecule, N-Cadherin, which is expressed only in Müller glia (Liu et al., 2001a; Liu et al., 2002; Raymond et al., 2006), and the actin-binding, scaffolding protein, Zonula Occludens-1 (ZO1) (Gosens et al., 2008). Similar to other epithelia, retinal adherens junctions are linked to the actin cytoskeleton through cadherin-catenin complexes (Harris and Tepass, 2010; Williams and Arikawa, 1990), which in other epithelia regulate changes in cell shape and position via tension sensing mechanisms that can dynamically alter the actomyosin cytoskeleton (Twiss and de Rooij, 2013). The transmembrane Crumbs proteins localize just apical to the zonula adherens junctions of the OLM in a zone that extends apically from the zonula adherens into the photoreceptor myoids and inner segments (Gosens et al., 2008; Salbreux et al., 2012; Zou et al.,

2012). Although the Crumbs complex has a well-established role in apicobasal epithelial polarity, the recent demonstration that the extracellular domain of Crumbs proteins mediates homophilic intercellular adhesion directly between cone photoreceptors in zebrafish suggests an additional potential role in the formation and/or maintenance of the cone mosaic pattern (Letizia et al., 2013; Thompson et al., 2013; Zou et al., 2012). Importantly, the distribution of Crumbs2a and Crumbs2b shows planar cell polarity in several cone subtypes, concentrating at the interfaces of cones within columns, not between the columns (Raymond et al., 2014; Salbreux et al., 2012; Zou et al., 2012).

In earlier work (Raymond et al., 2014; Salbreux et al., 2012), we argued that the arrangement during mosaic formation of cone cells into straight, single-file columns must reflect an underlying anisotropy in mechanical stresses within the retinal sheet, with a large tensile stress parallel to the columns and much weaker forces in the orthogonal direction. (Interestingly, this implies that high mechanical tensions are carried by cell-cell junctions with low Crumbs concentrations, consistent with findings of a similar correlation between planar polarized localization of Crumbs complex proteins and junctional tensions in *Drosophila* (Hafezi et al., 2012; Kaplan et al., 2011; Kaplan and Tolwinski, 2010; Roper, 2012; Simone and DiNardo, 2010).) We were unable, however, to measure this stress anisotropy directly. Indeed, current methods for measuring mechanical forces in intact tissues remain limited (Campas, 2016; Sugimura et al., 2016). One of the more widely-used techniques is laser ablation, wherein the mechanical force supported by a given element before its ablation is estimated from the recoil of surrounding cells after the element is ablated (Colombelli and Solon, 2013; Rauzi and Lenne, 2011; Shivakumar and Lenne, 2016). Although this approach does not give absolute force measurements, it has been successfully used to determine the degree of stress anisotropy in epithelial sheets *in vivo* (Behrndt et al., 2012; Bonnet et al., 2012; Lynch et al., 2013). Here, we adapt this method to probe the role of glial cells in establishing the ordered, columnar cone cell packing in zebrafish retina.

More specifically, in this study we explore the temporal sequence of photoreceptor mosaic formation with non-invasive live imaging and targeted cell ablation in living juvenile zebrafish retina, providing the first *in vivo* view of how the multiplex photoreceptor mosaic is created. Our results show that cone photoreceptor cell fate specification and correct spatial positioning

occur prior both to cell packing into linear columns and to planar polarized distribution of Crumbs, but roughly coincident with the first appearance of parallel lines of Müller glial cell processes that presage the formation of cone columns. Laser-mediated ablation of Müller glia near the retinal margin in living fish provided evidence of the predicted anisotropic tension in the retinal epithelium (Salbreux et al., 2012). We propose that the network of Müller glial apical processes linked by N-cadherin junctional contacts sustains the anisotropic mechanical forces that contribute to the alignment of cone photoreceptors. These studies reveal an unexpected role for Müller glia in organizing differentiating cones into linear columns in the teleost fish retina.

Results

Remodeling of apical profiles at the retinal margin reflects dynamic and gradual maturation of the cone mosaic

As we previously reported (Salbreux et al., 2012) the apical epithelial profiles of photoreceptors (rods and cones) and Müller glial processes at the level of the OLM can be visualized by immunostaining for the zonula adherens scaffolding protein, Zonula Occludens 1 (ZO1) in retinal flat-mounts (Fig. 1A). The identity of these apical profiles was verified in transgenic zebrafish lines with fluorescent reporters driven by promoters specific for Müller glia (*gfap*), rods (*rhodopsin*), cones (*cone alpha transducin*), UV cones (*sws1 opsin*), Blue cones (*sws2 opsin*), and Red cones (*trβ2*) (Raymond et al., 2014; Salbreux et al., 2012; Suzuki et al., 2013). The ZO1 profiles of each cell type have distinctive shapes (Fig. 1A,B), with some variations related to topographical position (data not shown). UV and Blue cones have rounded or elliptical profiles (Fig. 1B, magenta and blue, respectively). Paired Red and Green double cones form a theta-shape with a flattened interface (Fig. 1B, red and green). Rods are smaller and round (Fig. 1B,C, black). Lamellar processes of Müller glia completely enwrap each rod and cone within the retina and at the level of the OLM (Bringmann et al., 2006; Ramón y Cajal, 1972). Between cone columns, the apical profiles of Müller glia expand into polygonal shapes that occupy spaces between the rods (Fig. 1B, and (Salbreux et al., 2012)). Figure 1C is a cartoon illustrating the alignment of the photoreceptor mosaic lattice on the hemispheric retinal surface: orthogonal to the margin, rows of Blue and UV cones alternate with rows of Red and Green cones, and parallel to the margin, cones are organized into single-cell-wide columns with a 12-cell repeating order:

Red-Green-UV-Green-Red-Blue-Red-Green-UV-Green-Red-Blue. The cone columns are separated by parallel bands of rods and Müller glia. Neurogenesis continues in the proliferative germinal zone at the retinal margin (grey circles) adding annuli of new cells to the growing retina (Allison et al., 2010; Raymond and Barthel, 2004), so that successive cohorts of newly differentiated cones are incorporated appositionally into the pre-existing mosaic. Within the differentiated retina, rods (but not cones or Müller glia) are continuously produced by proliferating, dedicated rod progenitors (Raymond, 1985; Stenkamp, 2011), and accumulate in the inter-column bands. This precise spatiotemporal pattern allows us to examine in a single preparation successive stages in building this multiplex photoreceptor mosaic.

To systematically describe how the photoreceptor mosaic is established in the post-embryonic retina from proliferative retinal progenitors in the germinal zone at the retinal margin, we imaged retinal flat-mounts with ZO1 immunocytochemistry in rapidly growing juvenile zebrafish. We found that apical epithelial profiles at the OLM show gradual and dynamic changes from proliferative, to differentiating, to differentiated zones (Fig. 1D, Fig.1 supplemental figure and supplemental video). In order to minimize surgical damage to the retinal tissue, especially near the retinal margin, this preparation retains the retinal pigment epithelium (RPE), an epithelial layer that is physically separated from the neural retina (Dowling, 2012), but closely apposed to the proliferative epithelium in the germinal zone (Fig. 1 supplemental figure 1B). Therefore, the *z*-stack maximum projection shown in Figure 1D (and supplemental figure 1A) represents two, superimposed epithelia, but the profiles of RPE cells are easily distinguished by their distinctive large hexagonal shapes (Fig. 1D"', dashed polygon). Retinal progenitors in the proliferative germinal zone are identified with a mitotic cell marker, pH3 (Fig. 1D"' and supplemental figure 1B', 1B"), and their apical profiles are heterogeneous in size with a variety of polygonal shapes and flattened boundaries between neighbors (Fig. 1D, 1D"'). These dividing cells represent both multipotent and committed retinal progenitors that together generate all types of retinal neurons and Müller glia (Centanin et al., 2011; Raymond et al., 2006). At the central border of the pH3-labeled zone, cells with profiles at the apical surface become restricted to photoreceptors and Müller glia, as committed inner retinal neurons detach and migrate basally (Agathocleous and Harris, 2009; Suzuki et al., 2013). The transition between proliferating and differentiating zones is represented in this preparation by the reduced sizes and rounded shapes of some profiles (Fig. 1D, 1D", dots, presumptive photoreceptors) and the irregular, sharply

polygonal shapes of the Müller glia (Fig. 1D, 1D", asterisks). However, the ordered photoreceptor mosaic pattern is not yet apparent in this differentiating zone. In particular, these presumptive cones have not yet begun to express mature photoreceptor reporters, such as *Tg*(*sws1:*EGFP) or *Tg*(*sws2:*mCherry), in which a fluorescent reporter is driven by the UV or blue opsin promoter, respectively (Raymond et al., 2014). In the adjacent, more central zone, the crystalline array of the photoreceptor mosaic pattern emerges (Fig. 1D, 1D').

Cone cell fate commitment and precise spatial arrangement precedes column organization

To understand how cell fate determination, spatial arrangement, and cell packing are coordinated as new cells are incorporated into the mosaic at the growing retinal margin, we used transgenic reporter lines to visualize specific cell types. A previous study with live imaging and lineage tracing in embryonic zebrafish showed that the *thyroid receptor beta 2* (*trβ2*) promoter drives expression of a fluorescent reporter selectively in a subset of retinal progenitors that give rise exclusively to selected types of inner retinal neurons and to Red cones, but not to other cone types, and that the transgene expression is retained in differentiated Red cones (Suzuki et al., 2013). We first asked whether this transgenic reporter is expressed similarly in the germinal zone in juvenile *Tg(trβ2*:tdTomato*)* zebrafish. In radial retinal sections of *Tg(trβ2*:tdTomato*)* zebrafish only a subset of proliferative retinal progenitors in the germinal zone are *trβ2*:tdTomato+ (Fig. 2A – 2C), including mitotic figures (Fig. 2B, B'), confirming that some retinal progenitors express *trβ2*:tdTomato in the post-embryonic retina. More peripherally in the germinal zone, *trβ2*:tdTomato+ retinal progenitors are basally located, in regions containing differentiating inner retinal neurons (Fig. 2C, C' arrows). This is consistent with the previous report that the lineage of *trβ2*:tdTomato+ progenitors in the embryonic retina includes horizontal cells and ganglion cells, although these inner retinal neurons do not retain expression of the transgene after they differentiate (Suzuki et al., 2013). The *trβ2*:tdTomato+ cells with cuboidal nuclei at the apical surface in the differentiating zone (Fig. 2A, A' bracket) are committed to the Red cone identity.

To provide a dynamic view of the spatial arrangement of *trβ2*: tdTomato+ presumptive Red cones, we developed a live imaging technique to examine the retinal margin in young juvenile fish with multi-photon confocal microscopy. The retina cannot be visualized in living, wild-type (pigmented) zebrafish after the first ~2 weeks of development (Jusuf et al., 2013; Wan et al.,

2016) except through the pupil, and in that case, only the fundus can be seen, not the retinal periphery (Duval et al., 2013). To visualize cells at the retinal margin, we crossed transgenic reporter lines into a pigment-free double mutant genetic background, *albino (slc45a2)*$^{b4/b4}$*; roy*$^{a9/a9}$ (named '*ruby*') in which both melanin and iridophore pigments are largely abolished and adult fish are almost transparent (Ren et al., 2002). To label all photoreceptors, we used a second transgene, *crx:*mCFP, in which membrane-targeted CFP is expressed in both presumptive photoreceptor progenitors and mature cone and rod photoreceptors under the control of the *crx* promoter (Liu et al., 2001b; Suzuki et al., 2013). We then imaged the retinal margin in living fish through all the outer layers (sclera, choroid, RPE) from the dorsal side of the eye. These *in vivo* images confirm that in the proliferative germinal zone, *trβ2*:tdTomato+ progenitors are not regularly spaced (Fig. 2D and Fig. 2 supplemental video, asterisks). A regular spatial arrangement first appears in the pre-column zone when the photoreceptor cells start to differentiate, and their axons create the outer plexiform layer (OPL), which is defined by a dense band of *crx*:mCFP labeling basal to the cone nuclei (Fig. 2D' arrow). These immature cones have not yet developed an apical inner and outer segment, structures that are prominently labeled by mCFP in more central, differentiated cones (Fig. 2D' and Fig. 2 supplemental video).

In the cohort of presumptive cones that constitute the first column to emerge at the margin (Fig. 2D" and Fig. 2 supplemental video), successive *trβ2*:tdTomato+ Red cones are separated alternately by one (presumptive Blue cone) or three (presumptive Green-UV-Green cone) profiles (Fig. 2D" and supplemental video, white dots), a pattern that is consistent with the mature mosaic (Fig. 1B). In the three-cone interval between successive *trβ2*:tdTomato+ Red cones, the central profile is typically larger (Fig. 2D" and supplemental video), which we previously described as characteristic of immature UV cones (Raymond et al., 2014; Salbreux et al., 2012). The spatial arrangements of *trβ2*:tdTomato+ Red cones and *crx:*mCFP*+* cone profiles in the initial cone column are also correctly aligned with the adjacent column (Fig. 2D"' and supplemental video), so that differentiating *trβ2*:tdTomato+ Red cones are already incorporated into the hexagonal pattern of Red cones in the mosaic (Fig. 1B, 2D"'). These results indicate that post-mitotic, immature Red and UV cone photoreceptors are already correctly positioned when, or soon after, they acquire their subtype identities.

The hexagonal pattern of *trβ2*:tdTomato+ Red cones can also be visualized in flat-mount retinal preparations labeled with ZO1 (Fig. 2E-E"). Note the single large profiles of presumptive UV cones located in the middle of each hexagon (Fig. 2E-E"). Flat-mount retinas from the UV cone transgenic reporter line, *Tg(sws1*:EGFP*)*, confirmed that these large rounded profiles are UV cones in the mature retina, and the regularity of the mosaic array allows these distinctive profiles to be identified in the peripheral retina prior to onset of expression of the UV opsin transgene (Fig. 2 supplemental figure). These results together confirm that cone cell fate determination and spatial arrangement of Red and UV cones occurs prior to packing into a regular lattice.

Planar-polarized Crumbs distribution appears just prior to columnar packing

In the mature mosaic array, Crumbs 2b (Crb2b) proteins show planar polarized localization to intra-column, but not inter-column, interfaces of the apical processes (myoid and inner segments) of Red, Green, and Blue cone photoreceptors (Salbreux et al., 2012; Zou et al., 2012). Crb2b is not expressed in UV cones, rods, or Müller glia, although Crumbs 2a is expressed in all these cell types (Zou et al., 2012). In planar views the distribution of Crb2b immunoreactivity creates 'ladders' consisting of four parallel segments that separate pentameric units of Green-Red-Blue-Red-Green cones (Salbreux et al., 2012; Zou et al., 2012). In the growing retinal margin, Crb2b ladders appear nearly simultaneously in immature cones immediately adjacent to the first contiguous column (Fig. 3A-3A", arrow). This restricted, planar polarized localization of Crb2b at cone-cone interfaces indicates that the immature Red, Green, and Blue cones have acquired their identity and directionality prior to columnar packing. (Although it is formally possible that at this stage the fate of presumptive Green and Blue cones has not been fully specified, there are no other grounds to suspect the binary Green/Blue fate choice late in differentation that would then be needed.) However, these polarized Crb2b adhesive interactions occur after the initial differentiation and spatial patterning of Red and UV cones, as shown by regularly-spaced, large UV profiles located peripheral to the Crb2b ladders (Fig. 3A-3A", white dots). These observations suggest that the initial cell fate determination and spatial patterning of cones in the pre-column zone involves a Crb2b-independent mechanism.

Immature rod photoreceptors are correctly positioned in the pre-column zone

Interestingly, an equivalent planar polarized localization of Crb2a forming 'ladders' is not seen in the differentiating, pre-column zone, even though planar polarized distribution of both Crb2b and Crb2a in the apical processes of Red, Green, and Blue cones is a prominent feature of the mature mosaic (Salbreux et al., 2012). Instead, the most prominent Crb2a immunostaining appears in clusters of four small rings positioned inside the *trβ2*:tdTomato+ hexagons and surrounding the central UV cone (Fig. 3B-3B", inset arrows). This location is consistent with the positions of the initial rods in the larval zebrafish retina, which are found at the corners of UV cones (Fadool, 2003). It is known that the Crumbs complex mediates rod photoreceptor apical morphogenesis in developing zebrafish retina (Hsu and Jensen, 2010), and in mature regions of the retina, strong Crb2a immunoreactivity at the level of OLM surrounds the profiles of rods labeled with the rhodopsin transgene, *Tg(rh1:* EGFP) (Fig. 3C-3C"). Although the transgene driven by the rhodopsin promoter is expressed later in differentiated rod photoreceptors, and does not label the clusters of four Crb2a+ rings in the differentiating pre-column zone at the margin, together these data strongly suggest that immature rod photoreceptors are also precisely positioned prior to packing into a regular lattice.

To further evaluate whether rods exist in the differentiating pre-column zone, we analyzed the ratio of *trβ2*:tdTomato+ Red cones to *trβ2*:tdTomato-negative (other cone types and rod) photoreceptor cells visualized by their apical profiles in ZO1-labeled retinal flat-mounts. Irregular polygonal profiles of Müller glia were excluded from the cell counts. We predicted a 1:2 ratio of *trβ2*:tdTomato+ Red cones to *trβ2*:tdTomato-negative (Green + Blue + UV) cones, if only cones, but not rods, were present (Fig. 4A, B). This prediction is based on the following assumptions: (1) In the hexagonal pattern composed of six Red cones, each Red cone is shared by three hexagons, for a total of two Red cones per hexagon; (2) Each hexagon includes one UV and two Green cones; (3) Two Blue cones are shared by two hexagons for a total of one Blue cone per hexagon. However, if four rods are present at the corners of each UV cone, then we predict the ratio of *trβ2*:tdTomato+ to *trβ2*:tdTomato- profiles to be 1:4 (Fig. 4A, B).

The counting was carried out by automated method (Materials and Methods). Cell profiles at the level of the OLM, as determined by ZO1 immunoreactivity, were segmented and classified based on the presence of *trβ2*:tdTomato fluorescent reporter (Fig. 4 supplemental figure 1). The measured ratio of *trβ2*:tdTomato+ to *trβ2*:tdTomato- profiles was 1: 4.87, n=2 retinas, 780

total cells counted (Fig. 4C); samples from three additional retinas were also counted by visual inspection, and the ratios were within the range of the two automated samples. These results support the inference that rods are present in the pre-column zone. The strongly labeled, Crb2a+ rings in the predicted positions for rods in the *trβ2*:tdTomato+ Red cone hexagons implies spatial coordination of these initial rods, even though a crystalline lattice array of photoreceptors is not yet present.

As mentioned above, unlike cones, rod photoreceptors are continuously produced by dedicated precursors derived from Müller glia and seeded into the mature retina during retinal growth (Raymond, 1985; Stenkamp, 2011), where they accumulate preferentially between cone columns (Salbreux et al., 2012). It is unclear, however, whether the initial rods located at each corner of the UV cones at the growing margin derive from retinal progenitors in the germinal zone or from mitotic divisions of early Müller glia. In examining retinal margins in the Müller glia reporter line, *Tg*(*gfap:*EGFP), we found multiple examples of GFP+ mitotic figures in the peripheral pre-column zone (Fig. 4 supplemental video and supplemental figure 2), which is consistent with (but not proof that) rods are produced from Müller glia-derived rod precursors at the growing margin as they are in central retina.

Spatial analysis of Müller glial processes reveals organization into parallel bands prior to formation of cone columns

The apical processes of Müller glia expand at the level of the OLM and form both homotypic adherens junctions and heterotypic adherens junctions with photoreceptors (Salbreux et al., 2012; Williams and Arikawa, 1990). In retinal flat-mount preparations with ZO1 immunostaining, the cytoplasmic GFP Müller glial reporter surrounds the profiles of rods and cones, forming relatively thin intra-column lamella, and thicker inter-column expansions (Fig. 5 supplemental figure). To examine the temporal coordination between morphological maturation of Müller glial apical processes and emergence of the hexagonal pattern of *trβ2:*tdTomato+ Red cones, we imaged living, juvenile, double transgenic fish, *Tg*(*gfap:* EGFP*; trβ2:* tdTomato), in the pigment-free *ruby* genetic background. Immature Müller glia begin to express GFP weakly in the peripheral proliferative germinal zone (Fig. 5A-D and supplemental videos 1 and 2). Intensity of the GFP fluorescent reporter increased as Müller glia differentiated and expanded their apical processes laterally to surround photoreceptor profiles at the level of the OLM (Fig. 5A-A", B-B",

magenta dots, and supplemental video 2). The repeating pattern of one and then three presumptive cones between successive Red cones, seen with the *crx:*mCFP reporter above (Fig. 2D), can also be visualized in the profiles of Müller glial processes that surround presumptive cones (Fig. 5A", C", D'', white filled and open dots). These observations suggest that differentiating Müller glial apical processes provide a scaffold to organize photoreceptors at the level of OLM in the differentiating pre-column zone.

In the mature photoreceptor mosaic, Müller glial apical processes are preferentially distributed into parallel, inter-column bands (Fig. 5 supplemental figure). We next examined whether a similar distribution exists in the pre-column zone, thereby providing a potential glial scaffold for organizing cones into columns. We used ZO1 immunoreactivity (Fig. 5E) to selectively capture the GFP-labeled Müller glial profiles at the level of the OLM (Fig. 5E'), and applied a ridge analysis algorithm, available as an Image J plugin (Fig. 5E") (Jacob and Unser, 2004) that uses steerable filters to detect the presence and orientation of Müller glial bands. Variations in thickness of the Müller glial bands were revealed by tuning the width of the filter. We found that not only are the Müller glial bands that occupy the spaces between adjacent columns consistently thicker, but they also have a consistent direction parallel to the mature columns, even in the pre-column region where the differentiating photoreceptor cells are not yet packed into columns (Fig. 5E''-E'''). These results suggest that a Müller glial scaffold organizes the spatial arrangement of cones into parallel columns.

Photoreceptor differentiation includes loss of N-cadherin expression, whereas Müller glia show enhanced N-cadherin adhesive interactions in the mature mosaic

The suggestion that Müller glia organize the spatial arrangement of cones in the pre-column zone would require heterotypic intercellular interactions between Müller glia and differentiating cone photoreceptors. Previously we reported that N-Cadherin transcripts (*cdh2*) and protein are expressed by retinal progenitors in the germinal zone and by differentiated Müller glia, but not by mature photoreceptors (Liu et al., 2001a; Liu et al., 2002; Nagashima et al., 2013; Raymond et al., 2006). However, these studies did not consider immature photoreceptors recently produced at the retinal margin. The retinal progenitors (neuroepithelial cells) in the germinal zone form zonula adherens junctions through homophilic intercellular N-cadherin-

mediated adhesion (Williams and Arikawa, 1990). We hypothesize that immediately after withdrawing from the cell cycle, post-mitotic, immature cone photoreceptors transiently retain N-cadherin expression, so that during their initial phase of differentiation, they participate in N-cadherin-mediated intercellular junctions with Müller glia.

To examine the expression and distribution of N-Cadherin during maturation of the photoreceptor mosaic, we used *in situ* hybridization with *cdh2* probes on retinal cross-sections from juvenile fish. We detected *cdh2* transcripts in the germinal zone and in adjacent immature cone photoreceptors (Fig. 6A, A', A'', arrow). The *cdh2* signals became undetectable in differentiating photoreceptors more centrally in the laminated retina (Fig. 6A, A'''), where *cdh2* expression was restricted to Müller glia, identified by the GFP reporter in *Tg*(*gfap:*EGFP*)* fish (Fig. 6A, A', A'', arrowheads). Consistent with *cdh2* transcript expression, N-Cadherin immunoreactivity was also detected at the level of the OLM in differentiating cones in the pre-column zone, but the signal intensity decreased in the mature differentiated mosaic (Fig. 6B-B"). Strong punctate staining of ZO1 co-localized with N-cadherin was apparent in the inter-column bands in the mature mosaic (Fig. 6B-B"), consistent with expression of N-Cadherin in homophilic adherens junctions between Müller glia.

In the pre-column zone, we noticed that a subset of ZO1-labeled apical profiles were negative for N-Cadherin (Fig. C-C'', white asterisks). These small, round N-Cadherin-negative ZO1 profiles are likely to be immature rod photoreceptors, since they were located at each corner of the large UV profiles (Fadool, 2003). The lack of N-Cadherin expression in differentiating rods is consistent with their production from committed rod progenitors that lack apical processes and divide in the outer nuclear layer (Raymond, 1985; Stenkamp, 2011).

Intracellularly, N-Cadherin links to actomyosin via catenin complexes to regulate cytoskeletal contractility that controls cell shape and position; this contractile activity is mediated by phosphorylation of Myosin light chain II (Lecuit et al., 2010; Takeichi, 2014). We therefore examined immunolocalization of activated phospho-MyosinII (pMyoII) in differentiating cones and Müller glia. Because the anti N-cadherin and pMyoII were both rabbit antibodies, for this experiment we used mouse anti-Pan-Cadherin, the localization of which is identical to N-

Cadherin. In the pre-column zone, pMyoII co-labeled with Cadherin in the rounded profiles of immature cone photoreceptors (Fig. 6D, D', D'', E, E', E''). In the mature mosaic, pMyoII was predominately co-localized with Cadherin puncta in Müller glial processes between cone columns (Fig. 6D, D', D'', F, F', F''). These results suggest that immature cones and Müller glia in the pre-column zone remodel their apical profiles through Cadherin-catenin-mediated actomyosin contractility, and that in the mature mosaic, Müller glia generate contractile forces in parallel bands between cone columns.

Anisotropic tension in Müller glia organizes the photoreceptor lattice

Previous work suggested that highly anisotropic mechanical stresses within the retinal epithelium mediate cone mosaic formation and maintenance (Salbreux et al., 2012). These studies further pointed to planar polarized adhesive interactions mediated by Crumbs2a and Crumbs2b between adjacent cones along a column as one possible source of this anisotropy (Salbreux et al., 2012; Zou et al., 2012). The distribution of activated phospho-Myosin II in puncta representing N-Cadherin-mediated adherens junctions in inter-column bands of Müller glial suggests that actomyosin-mediated contractile forces might also be anisotropic.

To test this hypothesis, we applied multi-photon laser ablation to destroy Müller glia in living juvenile transgenic zebrafish carrying the *gfap:*EGFP reporter in the pigment-free mutant background. We targeted one or more individual Müller glial radial process near the cell body in the INL, which destroyed the entire cell and selectively abolished the apical Müller glial processes at the OLM (Fig. 7 supplemental figure) without damaging photoreceptors, as visualized by *trβ2*:tdTomato+ Red cones (Fig. 7A'). The ablation created a hole in the sheet of Müller glial processes at the level of the OLM (Fig. 7A, 7A' and Fig. 7 supplemental figure). We then examined relaxation of the epithelium after ablation by tracking the position of photoreceptors immediately surrounding the hole over a period of several minutes (Fig. 7A-A"'). As a control, we repeated the same procedure, but with the laser turned off at the ablation stage. We examined 8 ablated and 6 control retinas and measured the tissue deformation (strain) perpendicular (*x*-strain) and parallel (*y*-strain) to the retinal margin. These are plotted in Figures 7B and C, respectively. Control (unablated) retinas showed no significant changes in photoreceptor positions after repeated imaging (strain values ~ 1.0). After Müller glial ablation, we found no significant difference in *x*-strain perpendicular to the margin around the ablation

(Welch's unequal-variance, p-value = 0.1128). Parallel to the margin, however, measures of *y*-strain indicated significant elongation even at the earliest time-point (~5 minutes after ablation), and the amount of elongation increased with time (p-value = 0.0008). These observations imply that Müller glial processes support a substantial tensile mechanical stress along the cone columns. Combined with the observation that Müller glia cells form thick, phospho-Myosin-rich bands between cone columns parallel to the margin, these results suggest that Müller glia generate anisotropic mechanical tension across the retinal epithelium that could mediate the formation and maintenance of the photoreceptor lattice.

-

Discussion

Several distinctive features of the photoreceptor mosaic array in the zebrafish retina make this a particularly compelling model for studying the formation of orderly spatial arrangements and cell packing in vertebrate epithelia. Firstly, exquisitely precise rules operating at the level of individual photoreceptor cells determine the relative positions and identities of cone spectral subtypes and rod photoreceptors in the crystalline lattice array (Engström, 1963; Fadool, 2003; Salbreux et al., 2012). Although mosaics with evenly spaced distributions of specific cone subtypes are found in other vertebrate retinas (Kram et al., 2010; Marc and Sperling, 1977; Wikler and Rakic, 1991), and highly ordered arrays of sensory neuron hair cells are a prominent feature of the auditory epithelium in the mammalian cochlea (Kelley, 2007), neither these nor any other example of epithelial cell patterning in vertebrates involves a multiplex, heterotypic spatial order that specifies the identity of individual cells and their neighbors.

Secondly, although there is a characteristic average spacing between cones of the same subtype at the onset of differentiation in embryonic zebrafish (Raymond et al., 1995; Takechi et al., 2003), the highly-ordered, multiplex, lattice of photoreceptor rows and columns is not present in the embryonic and early larval retina, but instead emerges during larval development in association with changes in ocular mechanics, as the anterior chamber of the eye completes its differentiation (Allison et al., 2010; Soules and Link, 2005). We previously argued that, in adult zebrafish mutants with increased intraocular pressure, the resultant alteration in the retina's mechanical environment disrupts the regular photoreceptor array (Jusuf et al., 2013; Salbreux et al., 2012).

Finally, continuous growth of the post-embryonic teleost fish eye involves proliferation of retinal progenitors sequestered in a germinal zone at the anterior retinal margin, where discrete annuli of new cells are added to the existing retina (Agathocleous and Harris, 2009; Perron and Harris, 2000; Raymond et al., 2006). This appositional growth mode allows all stages in establishing the photoreceptor mosaic – from proliferation of progenitors to organization of the mature pattern – to be examined in a single preparation. Although the comparative optical transparency of zebrafish embryos allows live imaging and time-lapse studies of early retinal development (Godinho et al., 2005; Jusuf et al., 2013; Suzuki et al., 2013), accumulation of melanin pigment in the retinal pigmented epithelium and invasion of the outer layers of the eye by neural crest-derived melanophores and iridophores precludes live imaging after early larval stages. Here, using pigmentation mutants that lack melanin and guanine (iridophore) pigments (Ren et al., 2002), we report the first live imaging study of neurogenesis at the retinal margin in living juvenile zebrafish.

At the growing retinal margin at least two separate events must occur as newly generated cells join the multiplex photoreceptor mosaic: Cells must acquire a specific identity and they must rearrange into a rectangular crystalline lattice. Which comes first – cell fate or cell packing? How are these events coordinated? Knowing the sequence of cellular changes will provide clues to mechanisms that establish the multiplex lattice pattern. Our major findings are summarized in the schematic model in Figure 8. The apical profiles of neuroepithelial cells in the germinal zone are irregular polygons (Fig. 8, right), typical of proliferating epithelia (Farhadifar et al., 2007; Gibson et al., 2006), with adherens junctions stabilized by N-cadherin and ZO-1 (Cavey and Lecuit, 2009; Harris and Tepass, 2010; Takeichi, 2014). As presumptive photoreceptors withdraw from the cell cycle and begin to differentiate (Fig. 8, center), their apical profiles become rounder and smaller, and they label strongly for activated, phospho-Myosin II, consistent with apical constriction mediated by actomyosin contractility (Lecuit and Lenne, 2007; Lecuit et al., 2010). Parallel ridges of Müller glial processes aligned with the retinal margin also become visible as at this stage; although these processes completely surround the photoreceptors at the level of the OLM, they form thicker, straighter, more prominent lines between the presumptive cone columns than within the columns. In this pre-column zone, we propose that the different photoreceptor subtypes already show the basic features of their final

spatial pattern: They are distributed in a repetitive pattern with heterotypic correlations, and in particular, cones of a given subtype have the correct number of nearest neighbors of the correct (different) subtypes. On the other hand, the size of the cone profiles at the level of the OLM and the spacing between adjacent cones is still quite variable, and the organization of the cones into straight columns parallel to the margin is not yet apparent. The presumptive cone cells thus cannot yet be said to have fully organized themselves into their final, highly regular, crystalline packing. This ordered packing, characterized by straight columns, narrow distributions of cone sizes and spacings, and planar-polarized localization of Crumbs complex proteins, is attained only in the mature retina (Fig. 8, left).

A number of specific markers together with distinctive morphological characteristics support the inference that correct spatial patterning of cone subtypes and rods is roughly coincident with the onset of photoreceptor differentiation and precedes their packing into a precise lattice array. The most compelling evidence comes from analysis of the *trβ2*:tdTomato transgene, which labels fate-committed, proliferative Red cone progenitors and mature Red cones (Suzuki et al., 2013). In the mature mosaic, Red cones are spaced in a hexagonal pattern, and as they begin to differentiate in the pre-column zone, as evidenced by axonal outgrowth to create the outer plexiform (synaptic) layer of the retina, they are appropriately positioned with reference to the hexagonal pattern of Red cones in the adjacent mosaic. Time-lapse, lineage tracing of *trβ2*: tdTomato+ progenitors in embryonic zebrafish retina showed that the terminal mitotic division of these progenitors produces two Red cones (Suzuki et al., 2013), suggesting that the post-mitotic, presumptive Red cone daughter cells must move apart tangentially as they differentiate. Tangential migration is an important mechanism to establish homotypic mosaics of other retinal cells (Cook and Chalupa, 2000; Galli-Resta et al., 1997; Reese and Galli-Resta, 2002), and tangential movement of horizontal cells has been observed with time-lapse imaging in embryonic zebrafish retina (Godinho et al., 2005). Local, homotypic repulsive interactions of developing dendrites contributes to evenly spaced mosaics of non-photoreceptor retinal neurons (Reese and Galli-Resta, 2002), and although photoreceptors do not have dendrites, they do possess 'telodendria', fine fibers radiating from the axon terminal (Kolb and Jones, 1985) that mediate gap junction connections between cones (O'Brien et al., 2004). A time-lapse imaging study of Tg(*trb2*: tdTomato; *crx*: mCFP) zebrafish embryonic retinas suggested that

differentiating Red cones have telodendria (Suzuki et al., 2013), which could provide repulsive signals driving tangential migration.

Although a specific marker is not available for differentiating UV cones (the UV opsin transgene *sws1:*EGFP is not expressed until later stages in cone differentiation), distinctively large, round cone profiles are present in the center of the Red cone hexagon in the pre-column zone, at locations predicted by the row pattern of UV cones in the adjacent mosaic. The precocious appearance of properly spaced, presumptive UV cones in the differentiating pre-column zone is intriguing, since *tbx2b* mutant zebrafish, in which UV cones largely fail to differentiate, have severe defects in the multiplex photoreceptor mosaic pattern, even though other cone subtypes are produced in the correct ratio (Raymond et al., 2014).

Additional evidence supporting the inference that cell fate of cone and rod photoreceptors is established in the correct ratio prior to column packing is that the ratio of *trb2*: tdTomato+ differentiating Red cones to other presumptive cone and rod photoreceptors in the differentiating pre-column zone is close to the predicted ratio of 1:4 in the mature, multiplex mosaic. Furthermore, the first contiguous single-cell wide column of cones to emerge from the pre-column zone contains the correct ratio of cone subtypes, in that *trb2*: tdTomato+ Red cones are separated, alternately, by one and then three cones. That these cones already have established their correct identity is supported by the 'ladder-like' planar polarized pattern of Crb2b immunoreactivity, which localizes to the cell-cell interfaces between pentameric cone units (Green-Red-Blue-Red-Green) within a column in the mature mosaic (Salbreux et al., 2012; Zou et al., 2012). These pentameric Crb2b 'ladders', each separated by an intervening (Crb2b-negative) presumptive UV cone, are already apparent immediately peripheral to the first contiguous column of cones. The mechanisms through which presumptive cones select their spectral cell identity in zebrafish are not understood, although the process likely involves stepwise cell fate decisions driven by binary transcriptional switches regulating specific opsins and other features that distinguish cone subtypes in both vertebrate and invertebrate species, including mammals and fruit flies (Boije et al., 2015; Rister and Desplan, 2011; Swaroop et al., 2010).

Based on the results presented here, we propose a novel function for retinal Müller glia as organizers of the multiplex photoreceptor mosaic. This idea is supported by observations from three distinct stages in photoreceptor differentiation, corresponding respectively to the pre-column zone, the transition from the pre-column zone to the mature mosaic, and the mature mosaic.

The first line of evidence concerns the organization of glial cells in the pre-column zone. In the mature mosaic, apical processes of Müller glia establish a periodic scaffold parallel to the retinal margin, consisting of apical expansions that surround rod photoreceptors and that are preferentially localized between cone columns (Salbreux et al., 2012). In the pre-column zone, the apical expansions of differentiating Müller glia surround differentiating cone and rod photoreceptors but are less regularly shaped. Unexpectedly, we nonetheless found that the developing apical processes of immature Müller glia throughout the pre-column zone are preferentially distributed in periodic, linear bands parallel to the retinal margin that prefigure the cone columns. This is the earliest manifestation of a linear alignment of cones, suggesting that Müller glia play a causal role in aligning presumptive cones into the lattice pattern.

Within the pre-column zone, presumptive rod and cone photoreceptors show high levels pMyoII, indicative of strong cortical constriction. N-cadherin and ZO-1 localize to adherens junctions between Müller glia and presumptive cones, as well as to Müller glia-Müller glia junctions. These localization patterns suggest that forces generated by the actomyosin cortical network in photoreceptors and tension sensors in cadherin-mediated cell-cell adhesions likely mediate a gradual evolution in cell shape and position across the pre-column zone (Lecuit et al., 2010; Takeichi, 2014; Twiss and de Rooij, 2013). At the transition from the pre-column zone to the mature mosaic, however, there is an abrupt reorganization of both adhesion molecules and pMyoII. In the photoreceptors, N-cadherin expression is lost and levels of cortical pMyoII decrease, even as planar-polarized Crb-mediated adhesion appears between photoreceptors within columns. This change in the predominant photoreceptor adhesion molecules would favor a decrease in the length of cone cell-Müller cell junctions and a corresponding increase in the length of cone-cone junctions, consistent with the observed retraction of the Müller processes into straighter bands and expansion of contacts between cone photoreceptors within columns. At the same time, punctate adherens junctions colocalizing with high levels of pMyoII

appear between Müller glia cells, suggesting that the glial processes actively contract and straighten to corral the photoreceptors into the correct positions within the columns. Thus, our data point to a dynamic remodeling of adhesion molecules and cytoskeleton as a potential driving force for the cell shape and position changes that create the final, highly ordered photoreceptor packing at the transition from the pre-column zone to the mature multiplex mosaic. (A similar scenario has been proposed in some other, simpler epithelial systems (Bao and Cagan, 2005; Cavey and Lecuit, 2009; Hayashi and Carthew, 2004; Kafer et al., 2007; Lecuit et al., 2010; Twiss and de Rooij, 2013).)

In the mature mosaic, parallel bands of Müller glia stabilized by N-cadherin-mediated adherens junctions alternate with single-cell-wide columns of cones held by planar polarized Crb2b adhesive interactions. The concentration of activated pMyoII in punctate adherens junctions between Müller glia suggests that these glial bands remain under tension, forming a physical barrier between cone columns and contributing to mechanical stress anisotropies in the epithelial sheet, in analogy to the role of the contractile actomyosin cables that separate cells at compartment boundaries in the developing *Drosophila* wing (Monier et al., 2011) or that establish cell columns in the *Drosophila* embryonic ventral epidermis (Kaplan et al., 2011; Kaplan and Tolwinski, 2010; Simone and DiNardo, 2010). Thus, remarkably, a function that is performed by the cortical cytoskeleton inside the epithelial cells in these *Drosophila* systems would, in the vertebrate retina, instead be taken over by narrow apical processes extending up from glial cells in a different layer to interpose themselves between the photoreceptors at the level of the OLM. We directly demonstrated this mechanical function for the Müller glia through laser ablation: When an individual Müller glial cell is targeted at the level of the INL, its processes are lost from a compact region of the OLM, which then preferentially expands in the direction parallel to the retinal margin. This indicates that, before ablation, the glial processes had been exerting a tensile mechanical force parallel to the margin. [Notably, almost all previous applications of laser ablation to probe tissue mechanics have either directly targeted particular junctional structures or made large cuts across the epithelial surface, on the scale of many cell diameters; here, in contrast, we were able to take advantage of the retina's unique architecture to remove cells of one type and so to demonstrate a specific mechanical function for cellular processes whose width can be as small as tens of nanometers (Tarboush et al., 2012)]. Hence, within the mature retinal mosaic, Müller glial processes contribute to and

transduce a large anisotropy in tensile mechanical stresses, most likely through pMyoII-mediated active cytoskeletal contraction. This anisotropy, in turn, has been predicted to be essential for maintaining the highly ordered, columnar cone photoreceptor packing (Salbreux et al., 2012).

Müller glia have been implicated as important players in many different aspects of retinal biology, including neuronal development and differentiation, structural support of the complex, laminated cytoarchitecture, regulation of metabolic and homeostatic functions, and modulation of neuronal activity (Bringmann et al., 2006; Reichenbach and Bringmann, 2013; Willbold and Layer, 1998). Direct measurements of the viscoelastic properties of isolated Müller glial cells show they provide a soft, compliant mechanical substrate to accommodate activity-dependent local swelling in synapses and to facilitate neurite outgrowth within the synaptic layers of the retina (Lu et al., 2006; Lu et al., 2013; Reichenbach and Bringmann, 2013). In retinal explants, Müller glia respond to mechanical stretch of the retina orthogonal to the surface with increased calcium levels and changes in gene expression, suggesting that they act as tension sensors (Lindqvist et al., 2010). A recent study measured the biomechanical properties of embryonic zebrafish retinas and demonstrated that the radial processes of Müller glial cells are under tension and act like a springs to hold the retinal tissue together along the apical-basal dimension (MacDonald et al., 2015). Müller glia in post-embryonic teleost fish have additional roles in that they divide mitotically to generate neuronal progenitors, which migrate to the appropriate retinal layer along the radial glial fiber (Lenkowski and Raymond, 2014; Nagashima et al., 2013; Raymond and Rivlin, 1987; Stenkamp, 2011; Willbold and Layer, 1998), similar to the neuronal progenitors that derive from radial glia in the developing mammalian brain (Ever and Gaiano, 2005; Gotz and Barde, 2005). Recently, radial glia have also been implicated as key players in shaping tissue-level deformations such as gyrification (folding) of the mammalian cerebral cortex (Borrell and Gotz, 2014), and in the developing cerebellum, the related Bergmann glia establish anchoring centers that shape cerebellar foliation (Sudarov and Joyner, 2007). All of these examples primarily affect organization along the apical-basal dimension of the neural/retinal epithelium. In contrast, the present study proposes that Müller glia mediate spatial patterning of photoreceptors in the planar surface dimension though dynamic processes involving cell adhesion and cortex contractility.

Materials and Methods

Zebrafish

Wild-type TL zebrafish and transgenic lines *Tg(trb2:* tdTomato*)* and *Tg(crx:*mCFP*)* (Suzuki et al., 2013), *Tg(-3.7rho:*EGFP*)kj2 (Hamaoka et al., 2002); Tg(-5.5sws1*: EGFP*)kj9* (Takechi et al., 2003) ,*Tg(-3.2sws2*: mCherry*)mi2007* (Salbreux et al., 2012), and *Tg(gfap:*EGFP*)mi2002* (Bernardos and Raymond, 2006) were crossed into the '*ruby'* genetic background (Ren et al., 2002), with two independent, pigment mutations, *albino(slc45a2)*$^{b4/b4}$ *and roy*$^{a9/a9}$ (Zebrafish International Resource Center, Eugene, OR). We also generated triple pigment mutants, *albino(slc45a2)*$^{b4/b4}$*, roy*$^{a9/a9}$, *nacre(nac)*^{w2w2}*,* identical to the *crystal* fish described recently (Antinucci and Hindges, 2016), but we found that including the *nacre* mutation, which increases the number of iridophores (Lister et al., 1999), resulted in more chromatophores surrounding the eye; even though depleted of pigment the chromatophores retained endogenous fluorescence, which obscured retinal imaging. Fish were maintained at ~28C on a 14/10 hour light/ dark cycle with standard husbandry procedures (Westerfield, 1990). The Institutional Committee on the Care and Use of Animals at the University of Michigan approved all protocols.

Tissue preparation for retinal flat-mounts

Adult zebrafish were placed in the dark for 3 hours prior to dissection. After euthanizing by rapid chilling/hypothermia and cervical transection, the eye was enucleated and a small hole was made ventrally at the choroid fissure. With microscissors, the ventral hole was extended along the radial axis of the eyeball for orientation. The lens was removed, the eyecup was placed in phosphate buffered saline (PBS), and the neural retina was gently removed from the pigmented retinal epithelium with forceps, except at the peripheral retinal margin, where the overlying pigmented retinal epithelium was retained to preserve the retinal germinal zone. Short relaxation cuts were made along the perimeter, and the retina was fixed in 4% paraformaldehyde with 5% sucrose in 0.1M phosphate buffer (PB), pH 7.4, at 4C overnight. For

retinal cross sections, the cornea was punctured and the eyeball was fixed intact in 4% paraformaldehyde with 5% sucrose in PB, pH 7.4, at 4C overnight. After rinsing with 5% sucrose in PBS, the lens was carefully removed, and the tissue processed for cryosectioning as previously described (Barthel and Raymond, 1990).

Immunocytochemistry

Flat-mount retinal immunocytochemistry was performed as previously described (Raymond et al., 2014). For antigen retrieval, retinas were treated with 10 mM sodium citrate in 0.05% Tween 20 (pH 6.0) in boiling water for 5 minutes, and then removed from the heating plate and allowed to cool in the hot water for 5 minutes. After rinsing in PB with 0.5% Triton-X100, free-floating retinas were incubated in blocking buffer (10% normal goat serum, 1% Tween 20, 1% Triton X100, 1% DMSO in PBS, pH7.4, with 1% sodium azide) for 2 hours. Secondary antibodies were diluted in PB with 0.5% normal goat serum, 1% Tween 20, 1% Triton X100, 1% DMSO in PBS (pH7.4) with 1% sodium azide, and the incubations performed at room temperature overnight. Tissues were washed in the diluting buffer, and the retinas were mounted on microscope slides with Prolong Gold or Prolong Diamond (Invitrogen, Carlsbad, CA) with the photoreceptor side down.

Primary antibodies included mouse anti-Zonula Occludens-1, 1:200 (Invitrogen, Carlsbad, CA); rabbit anti-phospho histone 3, 1: 200 (Cell Signaling technology, Danvers, Massachusetts); rabbit anti-dsRed, 1: 200 (Clontech, Mountain View, CA); rabbit anti-GFP, 1:500 (Invitrogen, Carlsbad, CA); mouse anti-zs5 (Crb2a), 1:200 (Zebrafish International Resource Center, Eugene, OR); rabbit anti-Crb2b, 1:200 (gift from Xiangyun Wei, University of Pittsburgh); rabbit anti-N-Cadherin, 1:200 (Abcam, Cambridge, UK); mouse anti-pan-Cadherin, 1: 200 (Abcam, Cambridge, UK); rabbit anti-phospho-Myosin Light Chain 2 (Ser 19), 1:200 (Cell Signaling Technology, Danvers, MA). Secondary antibodies included anti-mouse DyLight 549, 1: 400 (Jackson ImmunoResearch, West Grove, PA or Thermo Fisher Waltham, MA); anti-rabbit DyLight 647, 1: 400 (Jackson ImmunoResearch, West Grove, PA or Thermo Fisher, Waltham, MA).

All flat-mount retinal preparations were imaged with a Zeiss AxioImage ZI Epifluorescent Microscope (Carl Zeiss Microimaging, Thornwood, NY) equipped with an ApoTome attachment

for optical sectioning using structured illumination, and processed with Adobe Photoshop CS6 Extended (Adobe Systems, San Jose, CA).

In situ hybridization

In situ hybridization was performed as previously described (Raymond et al., 2006). After rehydration and proteinase K treatment, retinal cross-sections were incubated with digoxigenin-labeled RNA probes for *cdh2* in Hauptmann's hybridization solution at 65C overnight. Sections were then washed, treated with alkaline phosphatase conjugated anti-digoxigenin antibody (Roche, Basel, Switzerland), and blocked with Maleate Blocking solution. The signal was detected with Fast Red (Roche, Basel, Switzerland).

Cell counts

Optical section *z*-stack images were obtained from the margins of flat-mounted retinas of transgenic *Tg(trβ2*:tdTomato*)* immunostained with antibody to ZO1. Cell profiles at the level of the OLM were obtained by selectively projecting the ZO1 channel using a MATLAB program developed in-house. The program reconstructs the OLM surface three-dimensionally by averaging the ZO1 signal with a Gaussian kernel in the *z*-direction and interpolating in the *x*- and *y*-directions. This reconstructed surface was then used to selectively capture the tdTomato signals at the level of the OLM.

The cell profiles from ZO1 were then segmented using watershed algorithms with manually-placed seeds. Irregularly-shaped Müller glial profiles were excluded by hand at this stage. Average tdTomato intensity at the level of the OLM for each segmented profile was then calculated and clustered into *trβ2*:tdTomato positive and negative groups using a *k*-means algorithm(MacKay, 2003).

Müller glia ridge analysis

Optical section *z*-stack images were obtained from the margins of flat-mounted retinas of transgenic *Tg(gfap:EGFP)* immunostained with antibody to ZO1. Profiles of GFP-labeled Müller glial cells were projected into the level of OLM (marked by ZO1) using the MATLAB program

described above under Cell Counts, selectively capturing GFP-labeled Müller glial profiles only at the level of the OLM.

Ridge detection using an anisotropic steerable filter was performed using a publicly available ImageJ plugin (Jacob and Unser, 2004). Briefly, for each pixel in the original image, the filter returns a value indicating how anisotropic (*i.e.*, ridge-like) the intensity field in the vicinity of the pixel is and an angle corresponding to the optimal ridge orientation. The "Refine features" function of the plugin then suppresses pixels with low ridge-like scores and isolated pixels with higher scores that do not form part of continuous ridge lines (Jacob and Unser, 2004). We found that a 4th order filter with width of 8 pixels (corresponding to the typical thickness of GFP signals between columns) best discriminates the thick, between-column expanded apical glial profiles from the thinner, within column lamellae, based on the least number of false positives. The former give mostly long, straight ridge lines parallel to the column, whereas the latter tend to appear as many short, curved ridge lines. To eliminate most of the latter and keep only the former, the ridge angles θ and intensities returned by the filter were imported into MATLAB, where they were compared to the direction θ_c of the columns, defined by applying a Fast Fourier Transform to the unfiltered image. (The direction with the largest Fourier amplitude is perpendicular to the columns.) Pixels with deviation $|\theta - \theta_c|$ more than 30^0 from the direction of the columns are deemed spurious and were eliminated. To further filter the result, ridges less than 20 pixels long were also removed. (If the same procedure is applied, but keeping pixels with angles near a value other than the correct column direction θ_c, few or no long ridges remain; thus, long, straight Müller glial ridges can be detected only parallel to the columns, as expected.)

Live imaging

Juvenile zebrafish (0.74-1.19 cm body length, exclusive of the tail) were anesthetized with 0.336 mg/ml Tricaine S/MS-222 (Western Chemical Inc., Ferndale, WA). When opercular movements ceased, the fish was placed in a 50mm glass bottom Petri dish with a No. 1.5 coverslip (MatTek Corporation, Ashland MA) and oriented dorsal side down, tipped laterally so that the dorsal aspect of one eye was directly apposed to the coverslip. Kimwipe tissues (Sigma-Aldrich, St. Louis, MO) moistened with anesthetic water were used to stabilize the fish during imaging. The

fish remained anesthetized in the imaging chamber for up to 1 hour. Continued viability was confirmed by the presence of a heart beat and blood flow to peripheral tissues.

Confocal *z*-stack images were captured with a Leica TCS SP8 LSCM (Leica Microsystems, Wetzlar, Germany) equipped with a tunable Chameleon 2-photon Ti:Sapphire laser (Coherent, Santa Clara, CA) and Leica 40X PL APO CS2 Water Immersion lens, 1.1 NA with 650 μm working distance. The Multiphoton (MP) laser was tuned to 800 nm and Leica HyD hybrid detectors tuned to 450-500 nm for Cyan; 500-550 nm for EGFP; 576-650 nm for tdTomato. The Argon laser (Excitation: 488 nm Emission: HyD 524-561 nm for EGFP; Excitation: 514 nm Emission: HyD 577-745 nm for tdTomato) was also used for capturing images of the germinal zone and far peripheral retinal margin, but laser penetration was insufficient for capturing signals from more central retina. For post-acquisition processing, *z*-stacks were loaded into the Leica Application Suite X (Leica Microsystems, Wetzlar, Germany), Image J (https://imagej.nih.gov/ij/), or Imaris 8.3.0 (Bitplane, Zurich, Switzerland) software for volume rendering and maximum intensity projection videos.

Müller glial ablation and analysis of epithelial tension

Juvenile zebrafish *Tg(gfap:*EGFP*)* were immobilized and imaged as described above. Pre-ablation and post-ablation MP images were acquired at 400 Hz acquisition speed with a resolution of 512 x 512 pixels in the *xy* dimension with a 1.8 μm interval between optical sections in the *z*-dimension. Targeted ablation of the radial process of an identified Müller glial cells was performed at the level of a single optical section 25-50 μm below the OLM. Up to 5 individual, isolated Müller glia were targeted in each retina with 700-900 nm diameter circles created by the 'Region of Interest' tool and centered on the radial fiber. Ablation was performed with the Chameleon 2-photon Ti:Sapphire laser tuned to 800 nm at maximum power output with acquisition speed of 10 Hz and zoom factor 12x.

Confocal *z*-stack images of the *gfap:*EGFP Müller glial reporter were selectively projected using the MATLAB routine described above under Cell Counts. The program reconstructs the OLM surface three-dimensionally by averaging the fluorescent signal with a Gaussian kernel in the *z*-direction and interpolating in the *x*- and *y*-directions, and selectively capturing the fluorescent

signal only at the OLM. The reconstructed surface was also used to estimate and correct for inclination of the OLM plane due to sample tilt. Radial fibers of Müller glial cells were masked manually when needed to achieve a cleaner projection. The centroid positions $\mathbf{r}_i = (x_i, y_i)^T$ of photoreceptor profiles surrounding the lesion area were then tracked in ImageJ and imported to MATLAB. Sample tilt was corrected by estimating the orientation of the OLM from the projection algorithm and rotating $\mathbf{r}_i$. Tissue deformation was estimated by finding the affine transformation $\hat{\mathbf{r}}_i^f = \mathbf{M}\mathbf{r}_i^0 + \mathbf{b}$ of the initial photoreceptor positions $\mathbf{r}_i^0$ that minimizes the mean-squared deviation $\sum_i \left\| \mathbf{r}_i^f - \mathbf{M}\mathbf{r}_i^0 - \mathbf{b} \right\|^2$ between the transformed positions $\hat{\mathbf{r}}_i^f$ and the actual positions $\mathbf{r}_i^f$ of the same photoreceptors at a given time after ablation. The residuals after this transformation at 0-15 minutes, 15-30 minutes, and >30 minutes after ablation are approximately 13%, 19%, and 23% of typical neighboring cell distance, respectively, indicating that the predominant deformation is indeed affine. For control experiments, the first two corresponding figures are 7% and 11% (there is no control with >30 minutes after ablation). Rotation of the images across samples was corrected by computing the polar decomposition $\mathbf{M} = \mathbf{U}\mathbf{P}$, where $\mathbf{U}$ is unitary and $\mathbf{P}$ is positive semi-definite. Strain magnitude and orientation were then calculated as the eigenvalues and eigenvectors of $\mathbf{P}$, with the eigenvector approximately along the cone columns identified with the *y*- strain and the eigenvector approximately perpendicular to the columns as the *x*-strain. (The directions of the principal strain axes typically deviate by 20 degrees or less from the orientation of the columns, and in only one case does the deviation exceed 35 degree, making the identification of one of the principal strain axes as the one along the column direction unambiguous. Much of the variability in principal strain directions that does exist appears to be attributable to irregularities in the shapes of lesioned regions.) For statistical analysis, strains at all different times after ablation were grouped together and compared against control. Welch's unequal-variance test suggested that there is statistically significant difference between ablation and control *y*-strain ($p=0.0008$), but not *x*-strain ($p=0.1128$). Confirming this, Hotelling's multivariate unequal-variance test using both *x*- and *y*-strain shows significant ($p=0.0002$) difference between ablation and control groups.

Acknowledgements

The authors thank Alcides Lorenzo Gonzalez and Diana Diaz Martin for assistance with fish husbandry, Rachael Wong, Shoji Kawamura, and Susan Brockerhoff for transgenic fish lines, Xiangyun Wei for antibodies, and other members of the Raymond and Lubensky laboratories for helpful discussions. This work was supported by NSF IOS-1353914 (D.K.L. and P.A.R.) and DMR-1056456 (D.K.L.).

Competing Interests

The authors declare no competing interests.

References

Agathocleous, M., and Harris, W.A. (2009). From progenitors to differentiated cells in the vertebrate retina. Ann Rev Cell Devel Biol *25*, 45-69. doi:10.1146/annurev.cellbio.042308.113259

Allison, W.T., Barthel, L.K., Skebo, K.M., Takechi, M., Kawamura, S., and Raymond, P.A. (2010). Ontogeny of cone photoreceptor mosaics in zebrafish. J Comp Neurol *518*, 4182-4195. doi:10.1002/cne.22447

Antinucci, P., and Hindges, R. (2016). A crystal-clear zebrafish for in vivo imaging. Sci Rep *6*, 29490. doi:10.1038/srep29490

Bao, S., and Cagan, R. (2005). Preferential adhesion mediated by Hibris and Roughest regulates morphogenesis and patterning in the Drosophila eye. Dev Cell *8*, 925-935. doi:10.1016/j.devcel.2005.03.011

Barthel, L.K., and Raymond, P.A. (1990). Improved method for obtaining 3-micron cryosections for immunocytochemistry. J Histochem Cytochem *38*, 1383-1388., http://www.ncbi.nlm.nih.gov/htbin-post/Entrez/query?db=m&form=6&dopt=r&uid=2201738

Behrndt, M., Salbreux, G., Campinho, P., Hauschild, R., Oswald, F., Roensch, J., Grill, S.W., and Heisenberg, C.P. (2012). Forces driving epithelial spreading in zebrafish gastrulation. Science *338*, 257-260. doi:10.1126/science.1224143

Bernardos, R.L., and Raymond, P.A. (2006). GFAP transgenic zebrafish. Gene Exp Patterns *6*, 1007-1013. doi:10.1016/j.modgep.2006.04.006

Boije, H., Rulands, S., Dudczig, S., Simons, B.D., and Harris, W.A. (2015). The independent probabilistic firing of transcription factors: A paradigm for clonal variability in the zebrafish retina. Dev Cell *34*, 532-543. doi:10.1016/j.devcel.2015.08.011

Bonnet, I., Marcq, P., Bosveld, F., Fetler, L., Bellaiche, Y., and Graner, F. (2012). Mechanical state, material properties and continuous description of an epithelial tissue. J R Soc Interface *9*, 2614-2623. doi:10.1098/rsif.2012.0263

Borrell, V., and Gotz, M. (2014). Role of radial glial cells in cerebral cortex folding. Curr Opin Neurobiol *27*, 39-46. doi:10.1016/j.conb.2014.02.007

Bringmann, A., Pannicke, T., Grosche, J., Francke, M., Wiedemann, P., Skatchkov, S.N., Osborne, N.N., and Reichenbach, A. (2006). Muller cells in the healthy and diseased retina. Prog Retin Eye Res *25*, 397-424. doi:10.1016/j.preteyeres.2006.05.003

Cameron, D.A., and Carney, L.H. (2004). Cellular patterns in the inner retina of adult zebrafish: quantitative analyses and a computational model of their formation. J Comp Neurol *471*, 11-25. doi:10.1002/cne.11040

Campas, O. (2016). A toolbox to explore the mechanics of living embryonic tissues. Semin Cell Dev Biol *55*, 119-130. doi:10.1016/j.semcdb.2016.03.011

Cavey, M., and Lecuit, T. (2009). Molecular bases of cell-cell junctions stability and dynamics. Cold Spring Harb Perspect Biol *1*, a002998. doi:10.1101/cshperspect.a002998

Centanin, L., Hoeckendorf, B., and Wittbrodt, J. (2011). Fate restriction and multipotency in retinal stem cells. Cell Stem Cell *9*, 553-562. doi:10.1016/j.stem.2011.11.004

Colombelli, J., and Solon, J. (2013). Force communication in multicellular tissues addressed by laser nanosurgery. Cell Tissue Res *352*, 133-147. https://dx.doi.org/10.1007/s00441-012-1445-1

Cook, J.E., and Chalupa, L.M. (2000). Retinal mosaics: new insights into an old concept. Trends Neurosci *23*, 26-34. doi:10.1016/S0166-2236(99)01487-3

Dowling, J.E. (2012). The retina : an approachable part of the brain, Rev. edn (Cambridge, Mass.: Belknap Press of Harvard University Press).

Duval, M.G., Chung, H., Lehmann, O.J., and Allison, W.T. (2013). Longitudinal fluorescent observation of retinal degeneration and regeneration in zebrafish using fundus lens imaging. Mol Vis *19*, 1082-1095. https://http://www.ncbi.nlm.nih.gov/pmc/articles/PMC3668685/

Eglen, S.J. (2006). Development of regular cellular spacing in the retina: theoretical models. Math Med Biol *23*, 79-99. doi:10.1093/imammb/dql003

Engström, K. (1963). Cone types and cone arrangements in teleost retinae. Acta Zool *44*, 179-243.

Ever, L., and Gaiano, N. (2005). Radial 'glial' progenitors: neurogenesis and signaling. Curr Opin Neurobiol *15*, 29-33. doi:10.1016/j.conb.2005.01.005

Fadool, J.M. (2003). Development of a rod photoreceptor mosaic revealed in transgenic zebrafish. Dev Biol *258*, 277-290. doi:10.1016/S0012-1606(03)00125-8

Farhadifar, R., Roper, J.C., Aigouy, B., Eaton, S., and Julicher, F. (2007). The influence of cell mechanics, cell-cell interactions, and proliferation on epithelial packing. Curr Biol *17*, 2095-2104. doi:10.1016/j.cub.2007.11.049

Galli-Resta, L., Leone, P., Bottari, D., Ensini, M., Rigosi, E., and Novelli, E. (2008). The genesis of retinal architecture: an emerging role for mechanical interactions? Prog Retin Eye Res *27*, 260-283. doi:10.1016/j.preteyeres.2008.02.001

Galli-Resta, L., Novelli, E., Kryger, Z., Jacobs, G.H., and Reese, B.E. (1999). Modelling the mosaic organization of rod and cone photoreceptors with a minimal-spacing rule. Eur J Neurosci *11*, 1461-1469. doi:10.1046/j.1460-9568.1999.00555.x

Galli-Resta, L., Resta, G., Tan, S.S., and Reese, B.E. (1997). Mosaics of islet-1-expressing amacrine cells assembled by short-range cellular interactions. J Neurosci *17*, 7831-7838. http://www.jneurosci.org/content/17/20/7831

Gibson, M.C., Patel, A.B., Nagpal, R., and Perrimon, N. (2006). The emergence of geometric order in proliferating metazoan epithelia. Nature *442*, 1038-1041. doi:10.1038/nature05014

Godinho, L., Mumm, J.S., Williams, P.R., Schroeter, E.H., Koerber, A., Park, S.W., Leach, S.D., and Wong, R.O. (2005). Targeting of amacrine cell neurites to appropriate synaptic laminae in the developing zebrafish retina. Development *132*, 5069-5079. doi:10.1242/dev.02075

Gosens, I., den Hollander, A.I., Cremers, F.P., and Roepman, R. (2008). Composition and function of the Crumbs protein complex in the mammalian retina. Exp Eye Res *86*, 713-726. doi:10.1016/j.exer.2008.02.005

Gotz, M., and Barde, Y.A. (2005). Radial glial cells defined and major intermediates between embryonic stem cells and CNS neurons. Neuron *46*, 369-372. doi:10.1016/j.neuron.2005.04.012

Hafezi, Y., Bosch, J.A., and Hariharan, I.K. (2012). Differences in levels of the transmembrane protein Crumbs can influence cell survival at clonal boundaries. Dev Biol *368*, 358-369. doi:10.1016/j.ydbio.2012.06.001

Hamaoka, T., Takechi, M., Chinen, A., Nishiwaki, Y., and Kawamura, S. (2002). Visualization of rod photoreceptor development using GFP-transgenic zebrafish. Genesis *34*, 215-220. doi:10.1002/gene.10155

Harris, T.J., and Tepass, U. (2010). Adherens junctions: from molecules to morphogenesis. Nat Rev Mol Cell Biol *11*, 502-514. doi:10.1038/nrm2927

Hayashi, T., and Carthew, R.W. (2004). Surface mechanics mediate pattern formation in the developing retina. Nature *431*, 647-652. doi:10.1038/nature02952

Hoon, M., Okawa, H., Della Santina, L., and Wong, R.O. (2014). Functional architecture of the retina: development and disease. Prog Retin Eye Res *42*, 44-84. doi:10.1016/j.preteyeres.2014.06.003

Hsu, Y.C., and Jensen, A.M. (2010). Multiple domains in the Crumbs Homolog 2a (Crb2a) protein are required for regulating rod photoreceptor size. BMC Cell Biol *11*, 60. doi:10.1186/1471-2121-11-60

Jacob, M., and Unser, M. (2004). Design of steerable filters for feature detection using Canny-like criteria. IEEE Transactions on Pattern Analysis and Machine Intelligence *26*, 1007-1019. doi:10.1109/TPAMI.2004.44

Jusuf, P., Harris, W.A., and Poggi, L. (2013). Imaging retinal progenitor lineages in developing zebrafish embryos. Cold Spring Harb Protoc *2013*. doi:10.1101/pdb.prot073544

Kafer, J., Hayashi, T., Maree, A.F., Carthew, R.W., and Graner, F. (2007). Cell adhesion and cortex contractility determine cell patterning in the Drosophila retina. Proc Natl Acad Sci U S A *104*, 18549-18554. doi:10.1073/pnas.0704235104

Kaplan, N.A., Colosimo, P.F., Liu, X., and Tolwinski, N.S. (2011). Complex interactions between GSK3 and aPKC in Drosophila embryonic epithelial morphogenesis. PloS one *6*, e18616. doi:10.1371/journal.pone.0018616

Kaplan, N.A., and Tolwinski, N.S. (2010). Spatially defined Dsh-Lgl interaction contributes to directional tissue morphogenesis. J Cell Sci *123*, 3157-3165. doi:10.1242/jcs.069898

Kelley, M.W. (2007). Cellular commitment and differentiation in the organ of Corti. Int J Dev Biol *51*, 571-583. doi:10.1387/ijdb.072388mk

Kolb, H., and Jones, J. (1985). Electron microscopy of Golgi-impregnated photoreceptors reveals connections between red and green cones in the turtle retina. J Neurophysiol *54*, 304-317. http://jn.physiology.org/content/54/2/304.long

Kram, Y.A., Mantey, S., and Corbo, J.C. (2010). Avian cone photoreceptors tile the retina as five independent, self-organizing mosaics. PloS one *5*, e8992. doi:10.1371/journal.pone.0008992

Lecuit, T., and Lenne, P.F. (2007). Cell surface mechanics and the control of cell shape, tissue patterns and morphogenesis. Nat Rev Mol Cell Biol *8*, 633-644. doi:10.1038/nrm2222

Lecuit, T., Lenne, P.F., and Munro, E. (2010). Force Generation, Transmission, and Integration During Cell and Tissue Morphogenesis. Annu Rev Cell Dev Biol. doi:10.1146/annurev-cellbio-100109-104027

Lenkowski, J.R., and Raymond, P.A. (2014). Muller glia: Stem cells for generation and regeneration of retinal neurons in teleost fish. Prog Retin Eye Res *40*, 94-123. doi:10.1016/j.preteyeres.2013.12.007

Letizia, A., Ricardo, S., Moussian, B., Martin, N., and Llimargas, M. (2013). A functional role of the extracellular domain of Crumbs in cell architecture and apicobasal polarity. J Cell Sci *126*, 2157-2163. doi:10.1242/jcs.122382

Lindqvist, N., Liu, Q., Zajadacz, J., Franze, K., and Reichenbach, A. (2010). Retinal glial (Muller) cells: sensing and responding to tissue stretch. Invest Ophthalmol Vis Sci *51*, 1683-1690. doi:10.1167/iovs.09-4159

Lister, J.A., Robertson, C.P., Lepage, T., Johnson, S.L., and Raible, D.W. (1999). nacre encodes a zebrafish microphthalmia-related protein that regulates neural-crest-derived pigment cell fate. Development *126*, 3757-3767. http://dev.biologists.org/content/126/17/3757.long

Liu, Q., Babb, S.G., Novince, Z.M., Doedens, A.L., Marrs, J., and Raymond, P.A. (2001a). Differential expression of cadherin-2 and cadherin-4 in the developing and adult zebrafish visual system. Vis Neurosci *18*, 923-933. http://doi.org/10.1017/S0952523801186098

Liu, Q., Londraville, R.L., Azodi, E., Babb, S.G., Chiappini-Williamson, C., Marrs, J.A., and Raymond, P.A. (2002). Up-regulation of cadherin-2 and cadherin-4 in regenerating visual structures of adult zebrafish. Exp Neurol *177*, 396-406. doi:10.1006/exnr.2002.8008

Liu, Y., Shen, Y., Rest, J.S., Raymond, P.A., and Zack, D.J. (2001b). Isolation and characterization of a zebrafish homologue of the cone rod homeobox gene. Invest Ophthalmol Vis Sci *42*, 481-487. http://iovs.arvojournals.org/article.aspx?articleid=2123082

Lu, Y.B., Franze, K., Seifert, G., Steinhauser, C., Kirchhoff, F., Wolburg, H., Guck, J., Janmey, P., Wei, E.Q., Kas, J.*, et al.* (2006). Viscoelastic properties of individual glial cells and neurons in the CNS. Proceedings of the National Academy of Sciences of the United States of America *103*, 17759-17764. doi:10.1073/pnas.0606150103

Lu, Y.B., Pannicke, T., Wei, E.Q., Bringmann, A., Wiedemann, P., Habermann, G., Buse, E., Kas, J.A., and Reichenbach, A. (2013). Biomechanical properties of retinal glial cells: comparative and developmental data. Exp Eye Res *113*, 60-65. doi:10.1016/j.exer.2013.05.012

Lyall, A.H. (1957). Cone arrangements in teleost retinae. Quart J Microsc Sci *98*, 189-201.

Lynch, H.E., Crews, S.M., Rosenthal, B., Kim, E., Gish, R., Echiverri, K., and Hutson, M.S. (2013). Cellular mechanics of germ band retraction in Drosophila. Dev Biol *384*, 205-213. doi:10.1016/j.ydbio.2013.10.005

MacDonald, R.B., Randlett, O., Oswald, J., Yoshimatsu, T., Franze, K., and Harris, W.A. (2015). Muller glia provide essential tensile strength to the developing retina. The Journal of cell biology *210*, 1075-1083. doi:10.1083/jcb.201503115

MacKay, D.J.C. (2003). Information theory, inference, and learning algorithms (Cambridge, U.K. ; New York: Cambridge University Press).

Marc, R.E., and Sperling, H.G. (1976). The chromatic organization of the goldfish cone mosaic. Vis Res *16*, 1211-1224. doi:10.1016/0042-6989(76)90044-4

Marc, R.E., and Sperling, H.G. (1977). Chromatic organization of primate cones. Science *196*, 454-456. doi:10.1126/science.403607

Monier, B., Pelissier-Monier, A., and Sanson, B. (2011). Establishment and maintenance of compartmental boundaries: role of contractile actomyosin barriers. Cell Mol Life Sci *68*, 1897-1910. doi:10.1007/s00018-011-0668-8

Nagashima, M., Barthel, L.K., and Raymond, P.A. (2013). A self-renewing division of zebrafish Muller glial cells generates neuronal progenitors that require N-cadherin to regenerate retinal neurons. Development *140*, 4510-4521. doi:10.1242/dev.090738

Nishiwaki, Y., Oishi, T., Tokunaga, F., and Morita, T. (1997). Three-dimensional reconstitution of cone arrangement on the spherical surface of the retina in the medaka eyes. Zool Sci *14*, 795-801. http://dx.doi.org http://dx.doi.org /10.2108/zsj.14.795

O'Brien, J., Nguyen, H.B., and Mills, S.L. (2004). Cone photoreceptors in bass retina use two connexins to mediate electrical coupling. J Neurosci *24*, 5632-5642. doi:10.1523/JNEUROSCI.1248-04.2004

Perron, M., and Harris, W.A. (2000). Retinal stem cells in vertebrates. Bioessays *22*, 685-688. doi:10.1002/1521-1878(200008)22:8%3C685::AID-BIES1%3E3.0.CO;2-C

Ramón y Cajal, S. (1972). The Structure of the Retina (Springfield, IL: Charles C. Thomas).

Rauzi, M., and Lenne, P.F. (2011). Cortical forces in cell shape changes and tissue morphogenesis. Curr Top Dev Biol *95*, 93-144. doi:10.1016/B978-0-12-385065-2.00004-9

Raymond, P.A. (1985). The unique origin of rod photoreceptors in the teleost retina. Trends in neuroscience *8*, 12-17.

Raymond, P.A., and Barthel, L.K. (2004). A moving wave patterns the cone photoreceptor mosaic array in the zebrafish retina. Int J Dev Biol *48*, 935-945. doi:10.1387/ijdb.041873pr

Raymond, P.A., Barthel, L.K., Bernardos, R.L., and Perkowski, J.J. (2006). Molecular characterization of retinal stem cells and their niches in adult zebrafish. BMC Dev Biol *6*, 36. doi:10.1186/1471-213X-6-36

Raymond, P.A., Barthel, L.K., and Curran, G.A. (1995). Developmental patterning of rod and cone photoreceptors in embryonic zebrafish. The Journal of comparative neurology *359*, 537-550. doi:10.1002/cne.903590403

Raymond, P.A., Colvin, S.M., Jabeen, Z., Nagashima, M., Barthel, L.K., Hadidjojo, J., Popova, L., Pejaver, V.R., and Lubensky, D.K. (2014). Patterning the cone mosaic array in zebrafish retina requires specification of ultraviolet-sensitive cones. PloS one *9*, e85325. doi:10.1371/journal.pone.0085325

Raymond, P.A., and Rivlin, P.K. (1987). Germinal cells in the goldfish retina that produce rod photoreceptors. Dev Biol *122*, 120-138. doi:10.1016/0012-1606(87)90338-1

Reese, B.E., and Galli-Resta, L. (2002). The role of tangential dispersion in retinal mosaic formation. Prog Retin Eye Res *21*, 153-168. doi:10.1016/S1350-9462(01)00024-6

Reichenbach, A., and Bringmann, A. (2013). New functions of Müller cells. Glia *61*, 651-678. doi:10.1002/glia.22477

Ren, J.Q., McCarthy, W.R., Zhang, H., Adolph, A.R., and Li, L. (2002). Behavioral visual responses of wild-type and hypopigmented zebrafish. Vision Res *42*, 293-299. doi:10.1016/S0042-6989(01)00284-X

Rister, J., and Desplan, C. (2011). The retinal mosaics of opsin expression in invertebrates and vertebrates. Dev Neurobiol *71*, 1212-1226. doi:10.1002/dneu.20905

Rockhill, R.L., Euler, T., and Masland, R.H. (2000). Spatial order within but not between types of retinal neurons. Proceedings of the National Academy of Sciences of the United States of America *97*, 2303-2307. doi:10.1073/pnas.030413497

Roper, K. (2012). Anisotropy of Crumbs and aPKC drives myosin cable assembly during tube formation. Dev Cell *23*, 939-953. doi:10.1016/j.devcel.2012.09.013

Salbreux, G., Barthel, L.K., Raymond, P.A., and Lubensky, D.K. (2012). Coupling mechanical deformations and planar cell polarity to create regular patterns in the zebrafish retina. PLoS Comput Biol *8*, e1002618. doi:10.1371/journal.pcbi.1002618

Shivakumar, P.C., and Lenne, P.F. (2016). Laser Ablation to Probe the Epithelial Mechanics in Drosophila. Methods Mol Biol *1478*, 241-251. doi:10.1007/978-1-4939-6371-3_14

Simone, R.P., and DiNardo, S. (2010). Actomyosin contractility and Discs large contribute to junctional conversion in guiding cell alignment within the Drosophila embryonic epithelium. Development *137*, 1385-1394. doi:10.1242/dev.048520

Soules, K.A., and Link, B.A. (2005). Morphogenesis of the anterior segment in the zebrafish eye. BMC Dev Biol *5*, 12. doi:10.1186/1471-213X-5-12

Stenkamp, D.L. (2011). The rod photoreceptor lineage of teleost fish. Prog Retinal Eye Res *30*, 395-404. doi:10.1016/j.preteyeres.2011.06.004

Sudarov, A., and Joyner, A.L. (2007). Cerebellum morphogenesis: the foliation pattern is orchestrated by multi-cellular anchoring centers. Neural Dev *2*, 26. doi:10.1186/1749-8104-2-26

Sugimura, K., Lenne, P.F., and Graner, F. (2016). Measuring forces and stresses in situ in living tissues. Development *143*, 186-196. doi:10.1242/dev.119776

Suzuki, S.C., Bleckert, A., Williams, P.R., Takechi, M., Kawamura, S., and Wong, R.O. (2013). Cone photoreceptor types in zebrafish are generated by symmetric terminal divisions of dedicated precursors. Proceedings of the National Academy of Sciences of the United States of America *110*, 15109-15114. doi:10.1073/pnas.1303551110

Swaroop, A., Kim, D., and Forrest, D. (2010). Transcriptional regulation of photoreceptor development and homeostasis in the mammalian retina. Nat Rev Neurosci *11*, 563-576. doi:10.1038/nrn2880

Takechi, M., Hamaoka, T., and Kawamura, S. (2003). Fluorescence visualization of ultraviolet-sensitive cone photoreceptor development in living zebrafish. FEBS Lett *553*, 90-94. doi:10.1016/S0014-5793(03)00977-3

Takeichi, M. (2014). Dynamic contacts: rearranging adherens junctions to drive epithelial remodelling. Nat Rev Mol Cell Biol *15*, 397-410. doi:10.1038/nrm3802

Tarboush, R., Chapman, G.B., and Connaughton, V.P. (2012). Ultrastructure of the distal retina of the adult zebrafish, Danio rerio. Tissue Cell *44*, 264-279. doi:10.1016/j.tice.2012.04.004

Thompson, B.J., Pichaud, F., and Roper, K. (2013). Sticking together the Crumbs - an unexpected function for an old friend. Nat Rev Mol Cell Biol *14*, 307-314. doi:10.1038/nrm3568

Twiss, F., and de Rooij, J. (2013). Cadherin mechanotransduction in tissue remodeling. Cell Mol Life Sci *70*, 4101-4116. doi:10.1007/s00018-013-1329-x

Wan, Y., Almeida, A.D., Rulands, S., Chalour, N., Muresan, L., Wu, Y., Simons, B.D., He, J., and Harris, W.A. (2016). The ciliary marginal zone of the zebrafish retina: clonal and time-lapse analysis of a continuously growing tissue. Development *143*, 1099-1107. doi:10.1242/dev.133314

Wässle, H., and Riemann, H. (1978). The mosaic of nerve cells in the mammalian retina. Proc Roy Soc Lond, Series B: Biol Sci *200*, 441-461,

Westerfield, M. (1990). The Zebrafish Book. A guide for the laboratory use of zebrafish (*Danio rerio*). (Eugene, OR: The University of Oregon Press).

Wikler, K.C., and Rakic, P. (1991). Relation of an array of early-differentiating cones to the photoreceptor mosaic in the primate retina. Nature *351*, 397-400. doi:10.1038/351397a0

Willbold, E., and Layer, P.G. (1998). Muller glia cells and their possible roles during retina differentiation in vivo and in vitro. Histol Histopathol *13*, 531-552, http://www.ncbi.nlm.nih.gov/pubmed/9589907

Williams, D.S., and Arikawa, K.P., T. (1990). Cytoskeletal components of the adherens junctions between the photoreceptors and the supportive Müller cells. J Comp Neurol *295*, 155-164. doi:10.1002/cne.902950113

Zou, J., Wang, X., and Wei, X. (2012). Crb apical polarity proteins maintain zebrafish retinal cone mosaics via intercellular binding of their extracellular domains. Dev Cell *22*, 1261-1274. doi:10.1016/j.devcel.2012.03.007

Figure legends

Figure 1. Emergence of the photoreceptor mosaic in rapidly growing juvenile zebrafish.
(A) Photoreceptor mosaic visualized by ZO1 immunocytochemistry on flat-mount retina. (B) Each cone profile is pseudo-colored to represent spectral identity (UV cones in magenta); rods are indicated with black. (C) Schematic showing emergence of the photoreceptor mosaic from the proliferative germinal zone (g.z.). The bracket (?) indicates the transition area of differentiating photoreceptor and Müller glial cells (the pre-column zone), which is the main focus of the present investigation. (D) Immunocytochemistry for ZO1 (green) in a flat-mount preparation of the retinal margin including the overlying retinal pigmented epithelium in a juvenile zebrafish *(z*-stack maximum projection). The retinal germinal zone is in the center, the ciliary and iris epithelium is on the right and mature retina is on the left. (See also Figure 1 supplemental video and Figure 1 supplemental figure.) (D') High magnification image of the mature photoreceptor mosaic. (D'') High magnification image of the differentiating, pre-column zone. Rounded profiles of immature photoreceptors are indicated by dots and irregular polygonal shapes of Müller glial apical profiles are indicated by asterisks. (D''') High magnification of the proliferative germinal zone with mitotic marker pH3 (magenta). Profile of a retinal pigment epithelial cell is indicated by the dashed line. Note that the apical cell profiles of the pH3+ nuclei cannot be identified in this maximum projection view due to parallax (see Figure 1 supplemental figure 1B'.) Scale bars: 10 μm (A, B, D, D'''); 5 μm (D', D'').

Figure 2. Spatial arrangement of cones is already patterned in the differentiating pre-column zone.
(A-C) Retinal cross-section in a transgenic fish, *Tg*(*trβ2*: tdTomato) (red). The nuclei are stained with Hoechst (gray). The retinal germinal zone is to the right (asterisks), central retina is to the left, and differentiated retina is laminated: ganglion cell layer (GCL), inner nuclear layer (INL), and outer nuclear layer (ONL). Differentiating Red cones with cuboidal nuclei in the ONL are *trβ2*: tdTomato+ (arrow). At the central edge of the germinal zone, some apically localized mitotic retinal progenitors (bracket) are positive for *trβ2*: tdTomato. In this region, inner retinal neurons have withdrawn from the cell cycle, and retinal lamination has commenced. (B, B') Mitotic *trβ2*: tdTomato+ progenitor. (C, C') Peripheral *trβ2*: tdTomato+ cells migrating basally to differentiate into inner retinal neurons (arrows). (D-D''') Live imaging of a double transgenic

juvenile fish, *trβ2*: tdTomato (red) and *crx:* mCFP (cyan). (See Figure 2 supplemental video for the complete *z*-stack series.) (D) Single *z*-level focal plane, with the *xy*-crosshair on a *trβ2*: tdTomato+ cell in the proliferative zone, where labeled cells do not exhibit a regular distribution. (See also Figure 2 supplemental video, white asterisks.) The *xz* and *yz* slice views are shown in the flanking panels. (D') Single *z*-level focal plane, with the *xy*-crosshair on a *trβ2*: tdTomato+ cell in the first cone column in the differentiating zone. Differentiating *trβ2*: tdTomato+ cells that have begun to form axonal processes (arrow) exhibit regular spatial patterning. (D") The first cone column is composed of *trβ2*: tdTomato+ Red cones alternately separated by one (presumptive UV) and three (presumptive Green-Blue-Green) cone profiles. (See also Figure 2 supplemental video.) (D"') The *trβ2*: tdTomato+ Red cones are immediately incorporated into the hexagonal pattern of Red cones in the mosaic. (E-E") Retinal flat-mount immunocytochemistry for ZO1 (green) in a *Tg*(*trβ2*: tdTomato) fish (red). (E) *z*-stack maximum projection of ZO1 channel. (E') A single *z*-level focal plane, with the tdTomato channel focused at the ZO1 level in the pre-column zone. Large presumptive UV cone profiles in the middle of each Red cone hexagon are indicated by white dots in the inset. (E") Merged image of ZO1 and *trβ2*: tdTomato+ channels. Scale bars: 20 μm (A'); 5 μm (B'); 10 μm (C', D'', D''', E'').

Figure 3. Spatial patterning of cones precedes planar polarized Crumbs localization.
(A-A") Retinal flat-mount immunocytochemistry for Crb2b (magenta) and ZO1 (green) at the retinal margin. (A) Single *z*-level focal plane image of Crb2b channel at the ZO1 level in the pre-column, differentiating zone. (Note that due to curvature of the retinal surface, the equivalent ZO1 level in central retina to the left is in a different focal plane.) Crb2b is planar polarized, localizing to the interfaces between Green-Red-Blue-Red-Green pentameric units of cones within a column. The distinctive Crb2b 'ladder' first appears in the pre-column zone (arrow) prior to the first continuous cone column. The large presumptive UV cone profiles (white dots) extend further out toward the margin. (A') *z*-stack maximum intensity projection of ZO1 channel. (A") Merged image of Crb2b and ZO1. (B-B") Crb2a immunocytochemistry (magenta) at the retinal margin with *Tg*(*trβ2*: tdTomato) (green). (B) The strongest Crb2a staining at the level of the OLM is between cone columns in small rings (inset). (B', B'') The Crb2a+ rings (arrows) are not co-labeled with *trβ2*: tdTomato, but are at each corner of the UV cones in the centers of the *trβ2*: tdTomato+ Red cone hexagons. (C-C") Crb2a immunohistochemistry (magenta) in the mature retinal mosaic in the transgenic rod line, *Tg*(*rh1*: EGFP) (green). Crb2a+

rings form chains aligned parallel to the margin between cone columns. (C', C") The Crb2a+ rings surround *rh1:* EGFP+ rod photoreceptors. Scale bars: 10 μm (A'', B'', C'').

Figure 4. Rod photoreceptors are incorporated into the cone mosaic as it emerges from the proliferating zone.

(A) Schematic of photoreceptor mosaic. Large circles of red, green, blue, and magenta (UV) represent types of cone photoreceptors. Small black circles represent rod photoreceptors. Hexagonal pattern of red cones is indicated by white dotted lines. (B) The expected ratio of trβ2+ (Red) to trβ2- (Green+Blue+UV) photoreceptor profiles as defined by ZO1 immunostaining (see Figure 1D) is 1:2, if rod photoreceptors are not present. The expected ratio of trβ2+ (Red) to trβ2- (Green+Blue+UV+rod) is 1:4, if rod photoreceptors are present. (C) Results from automated cell counting analysis of two retinas (n=780 total cells counted). (See also Figure 4 supplemental figure 1.)

Figure 5. Parallel bands of Müller glial scaffolding appear simultaneously with differentiating cones.

(A-D) Live imaging of the retinal margin in a double transgenic juvenile fish *Tg*(*trβ2*: tdTomato) (red) and *Tg*(*gfap:*EGFP) (green). (See Figure 5 supplemental videos 1 and 2 for the complete *z*-stack focal series.) (A-A") Maximum projection of *z*-stack series. Individual cone profiles are enwrapped by Müller glia. Immature Müller glia weakly express EGFP reporter in the proliferative zone (toward right). (B-D) Single *z*-levels focused on pre-column (B), and patterned (C, D) areas. (B-B") As Müller glia differentiate, the intensity of EGFP reporter increases, and apical processes enwrap the differentiating *trβ2*: tdTomato+ Red cones in the pre-column zone (magenta dots). (C-C" and D-D") The *trβ2*: tdTomato+ differentiating Red cones (filled white dots) form a hexagonal pattern (A-A''). Within a column, adjacent *trβ2*: tdTomato+ Red cones are separated by one (presumptive UV) and three (presumptive Green-Blue-Green) cones (open white dots). (E-E''') Ridge analysis applied to Müller glial profiles identified in a *Tg*(*gfap*: EGFP) (green) retinal flat-mount with immunocytochemistry for ZO1 (magenta). (Also see Figure 5 supplemental figure.) Discrete bands (ridges) of Muller glial apical processes aligned parallel to the margin extend into the zone of differentiating cone photoreceptors, prior to packing into single cell width columns. Arrows (E-E'') indicate the location of the first ordered column of cone photoreceptors that can be clearly discerned from cell outlines at the level of the OLM (E);

ridges of fluorescently marked Müller glia clearly extend multiple columns farther into the germinal zone (E'-E'''). Scale bar: 5 μm (D'').

Figure 6. N-cadherin is associated with actomyosin mechanical forces in differentiating cones in the pre-column zone and with Müller glia inter-column bands in the mature mosaic. (A-A"') *In situ* hybridization for *cdh2* (white or magenta) in a retinal cross-section from Müller glial reporter line, *Tg*(*gfap*:EGFP) (green). Proliferating progenitors in the germinal zone, immature photoreceptors (arrow), and mature Müller glia (arrowheads) express *cdh2* transcripts. Mature photoreceptors do not express *cdh2*. (B-B") Retinal flat-mount immunocytochemistry for ZO1 (magenta) and N-Cadherin (green) at the retinal margin. (C-C"') High magnification image of the boxed region in B-B". In the pre-column zone, N-Cadherin localizes to circular cone profiles and strong puncta (arrows) outside photoreceptor profiles. In the mature mosaic, immunoreactivity of N-Cadherin decreases around cone profiles and N-Cadherin signal accumulates between the cone columns in punta that co-localize with ZO1. N-Cadherin-negative profiles of presumptive rods (yellow dots) localize to the corners of large, presumptive UV profiles (white dots). (D-D") Retinal flat-mount immunocytochemistry for phospho-Myosin light chain II (magenta) and pan-Cadherin (green). (E-E") High magnification image of pre-column zone (yellow boxed region); pMyoII and pan-Cadherin co-localize to profiles of cone photoreceptors. (F-F") High magnification image of mature mosaic area (white boxed region); pMyoII and pan-Cadherin co-localize to puncta between the cone columns (arrows). ONL: outer nuclear layer; INL: inner nuclear layer. Scale bars: 10 μm (A''', B''', D'').

Figure 7. Müller glia mediate anisotropic mechanical forces in the retinal epithelium. (A-A") Live imaging time course series of targeted Müller glial ablations in a double transgenic *Tg*(*gfap*: EGFP) (green) and *Tg*(*trβ2*: tdTomato) (red) juvenile zebrafish. Photoreceptor profiles tracked for strain analysis are marked by dots. (A') Targeted ablation of Müller glia introduces a hole in the sheet of Müller glial processes at the apical surface of the retinal epithelium. (Also see Figure 7 supplemental figure.) Relaxation of the retinal epithelium surrounding the ablated region at 27 min (A") and 54 min (A"') after ablation; note the elongation of the dark, ablated region in the vertical direction over time. Times indicated represent the mid-point of the confocal imaging series. (B-C) Mechanical strain perpendicular to (*x*-strain, B) and parallel to (*y*-strain, C) the retinal margin after targeted ablation of Müller glia. Strains greater and smaller

than 1 represent stretching and compression, respectively. Each retina is represented by a different shaped symbol (n=6 controls; n=8 experimental). The horizontal axis gives the time interval between the ablation and the middle of the post-ablation imaging scan; two or three post-ablation scans were collected for each retina. (B) Perpendicular to the margin, control (no ablation) and experimental retinas show no significant differences (p=0.1128, Welch's unequal variance). (C) After selective ablation of Müller glia, the retinal epithelium relaxed significantly in the dimension parallel to the margin, *y*-strain > 1 (p=0.0008, Welch's unequal variance). Scale bar: 5 μm (A'''').

Figure 8. A model for how the multiplex photoreceptor mosaic is patterned by anisotropic tension, glial scaffolding, and planar polarized cell adhesion.

A) lateral view and B) planar view of sequential changes in apical cell profiles and expression and localization of cell-cell adhesion complexes (N-cadherin, Crumbs2b, and ZO-1) as photoreceptors and Müller glia progress from proliferative retinal progenitors in the germinal zone (right) to differentiating cells in the pre-column zone (center) to fully differentiated components of the mature cone mosaic (left). Colored cell profiles, cone photoreceptors (UV cones in magenta); dark yellow cells (center and left panels), Müller glia; light yellow cells (lower right panel), undifferentiated precursors. See Discussion for additional details.

Figure 1 supplemental figure. Maximum projection *z*-stack and lateral slice view of retinal margin illustrating shape and position of mitotic figures.

(A) Snap shot from a 3D-reconstruction of the retinal margin and retinal pigmented epithelium in a flat-mount preparation immunostained for ZO1 (green). Proliferative, differentiating (pre-column), and differentiated (mature mosaic) zones of the retina are labeled. (B-B") Lateral view of ZO1 (green) and pH3 (magenta) immunocytochemistry. (B) The retinal pigment epithelium (arrow) and neural retinal epithelium (arrowhead) are closely apposed, especially in the proliferative zone. (B') The pH3+ mitotic cells are tilted with respect to the plane of the retinal epithelium, and the resultant parallax precludes identifying the profiles of pH3+ mitotic cells in the ZO1 channel in a maximum *z*-stack projection (*e.g.,* Fig. 1D'). (B', B"') Proliferating endothelial cells in the circumferential blood vessel (yellow arrow) of the vitreal circulation, which lies below the retinal germinal zone

(B) (Raymond et al., 2006), are also labeled by pH3 (asterisks). Scale bar: 20 μm (A).

Figure 2 supplemental figure. Immature UV cones have large rounded apical profiles in the pre-column area.

(A, A') Retinal flat-mount immunocytochemistry for ZO1 (green) in the mature UV cone reporter line, *Tg*(*sws1*: EGFP) (magenta). The onset of the *sws1* opsin transgene is delayed until after formation of cone columns. (A') The precision of the mosaic pattern allows profiles that are *Tg*(*sws1*: EGFP)-negative to be identified as UV cones (magenta dots), and the position and shape of the large rounded profiles in the pre-column zone (white dots) suggests that these are presumptive UV cones. Note the appearance of a new row and column (yellow dot) in this region, a pattern defect called a 'Y-junction' (Nishiwaki et al., 1997), which is analogous to an edge dislocation in crystals grown on curved surfaces, and is required to accommodate the increased perimeter with continued retinal growth. Scale bar: 10 μm.

Figure 4 supplemental figure1. Segmentation and classification of photoreceptor profiles.

Selective projection of ZO1-labled cell profiles (A, A'') and *trβ2*:tdTomato+ Red cones (A', A'') in the pre-column zone of a retinal flat-mount. Panel A''' shows the tdTomato signal intensity at the level of the segmented cell profiles, which was used for the automated classification and counting procedure described in the Methods.

Figure 4 supplemental figure 2. Some Müller glial cells undergo mitosis in the pre-column zone.

(A) Maximum *z*-stack projection of live imaging from a double transgenic fish *Tg*(*gfap*: EGFP) (green) and *Tg*(*trb2*: tdTomato) (red). The *xy*-crosshairs (red-yellow) indicate the mitotic figure of a GFP+ Müller glial cell, and the *xz* and *yz* slice views are shown in the flanking panels. In this example, the mitotic figure of a GFP+ Müller glial cell is at the apical surface. (B) Another example of a mitotic GFP+ Müller glial cell, in which the nucleus is located in the inner nuclear layer. (See also Fig. 4 supplemental video for a 3D-reconstruction.) Scale bars: 10 μm (A, B).

Figure 5 supplemental figure. Müller glial apical processes are preferentially distributed into parallel, inter-column bands.

(A-A") Retinal flat-mount immunocytochemistry for ZO1 (magenta) in the Müller glial transgenic reporter line, *Tg*(*gfap*: EGFP). Müller glial processes (GFP+) completely surround the profiles of

individual rods and cones, forming relatively thin intra-column lamella, and thicker inter-column expansions. Refer to Fig. 1 for description of columns.

Figure 7 supplemental figure. 3D reconstruction demonstrates complete ablation of targeted Müller glia near the retinal margin.

Confocal *z*-stack series of *Tg*(*gfap*: EGFP)-labeled Müller glial processes from the level of the outer limiting membrane (OLM) to the cell body before (A) and 9 min after laser ablation (B). Multi-photon laser ablation targeted the radial process at a depth of 25-50 μm, between the OLM and the level of the cell body (~63 μm below the OLM in this example). Three targeted Müller glial cell bodies and processes are indicated by asterisks. (B) Multi-photon laser ablation targeting the radial glial process at a single *z*-level successfully destroyed the cell body and ascending processes of Müller glia (asterisks) and created a hole in the sheet of Müller glial processes at the level of OLM. The surrounding Müller glia remained intact (magenta dots), except for one cell close to the cluster of three targeted cells, which disappeared after the ablation (rectangle). The difference in the relative distance from OLM to the cell bodies of surviving Müller glia before and after ablation (-63 μm and -64.8 μm) is consistent with a previous report that radial processes of Müller glial in embryonic zebrafish retinas function like a spring, providing tension in the plane perpendicular to the apical surface (MacDonald et al., 2015). Scale bar: 5 μm (A, B).

Figure 1 supplemental video. 3D-reconstruction of the peripheral retina and overlying retinal pigmented epithelium demonstrates the close apposition of these two epithelia at the retinal germinal zone.

3D-reconstruction (maximum intensity *z*-projection) of the retinal margin in a flat-mount preparation of neural retina and overlying retinal pigmented epithelium, immunostained for ZO1 (green).

Figure 2 supplemental video. Live imaging of the photoreceptor mosaic emerging at the retinal margin in rapidly growing juvenile zebrafish.

Confocal *z*-stack series of live imaging at the dorsal retinal margin in a double transgenic fish *Tg*(*trβ2*:tdTomato) in red and *Tg*(*crx*:mCFP) in cyan. The *crx* promoter is expressed in all cone and rod photoreceptors. The *trb2*: tdTomato+ proliferative retinal progenitors are randomly

distributed in the most peripheral region of the germinal zone (asterisks). The first cone column (arrow) is composed of *trb2*: tdTomato+ Red cones alternately separated by profiles of one or three presumptive cones (white dots), as predicted by the organization of cone types in a column in the mature mosaic. Differentiated cones develop apical projections, including conical-shaped outer segments that are strongly labeled by the *crx*:mCFP reporter.

Figure 4 supplemental video. Müller glial cell mitotic figure within the inner nuclear layer in the pre-column zone.

3D-reconstruction (maximum intensity *z*-projection) of a mitotic Müller glia (arrowhead) labeled by the *Tg*(*gfap*:EGFP) reporter in a living fish. Mitosis in this example occurs in the inner nuclear layer where Müller glial nuclei are normally positioned. This is consistent with the generation of rod-committed precursors from asymmetric divisions of Müller glia in the zebrafish retina. (See also Figure 4 supplemental figure 2B.)

Figure 5 supplemental video 1. Müller glial apical processes provide scaffolding for differentiating photoreceptor cells.

3D-reconstruction (maximum intensity *z*-projection) of live imaging from a double transgenic fish, *gfap*:EGFP (green) and *trβ2*:tdTomato (red). Müller glial processes extend laterally at the level of OLM to surround profiles of individual Red cones and other photoreceptors. Processes of the early differentiating Müller glia near the germinal zone have not yet enwrapped cell bodies of photoreceptors below the OLM.

Figure 5 supplemental video 2. Red cones in the pre-column zone (magenta dots) and in the mature mosaic (white dots) are surrounded by Müller glial scaffolding.

A higher magnification video of a portion of the field shown in Figure 5 supplemental video 1. Weak GFP signals of immature Müller glia first appear in the proliferative zone (toward the right). The intensity of the GFP signal increases in differentiating Müller glia and their processes surround photoreceptors, including differentiating *trβ2*:tdTomato+ Red cones (magenta dots) at the level of the OLM. Emergence of the hexagonal distribution of *trβ2*:tdTomato+ Red cones (white dots) is accompanied by morphological maturation of Müller glia.

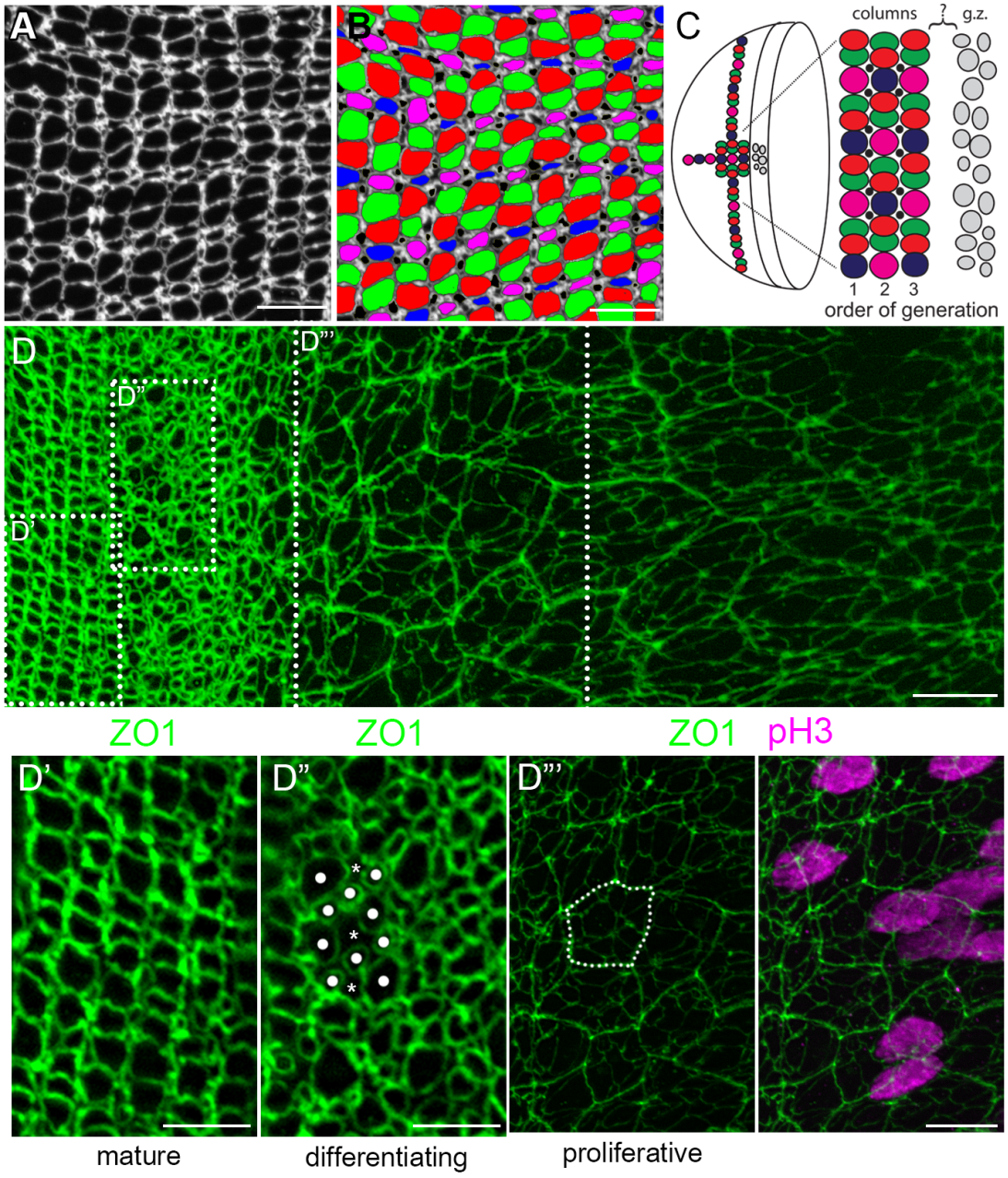

Figure 1

Figure C.1: **Emergence of the photoreceptor mosaic in rapidly growing juvenile zebrafish.** See manuscript caption page for details.

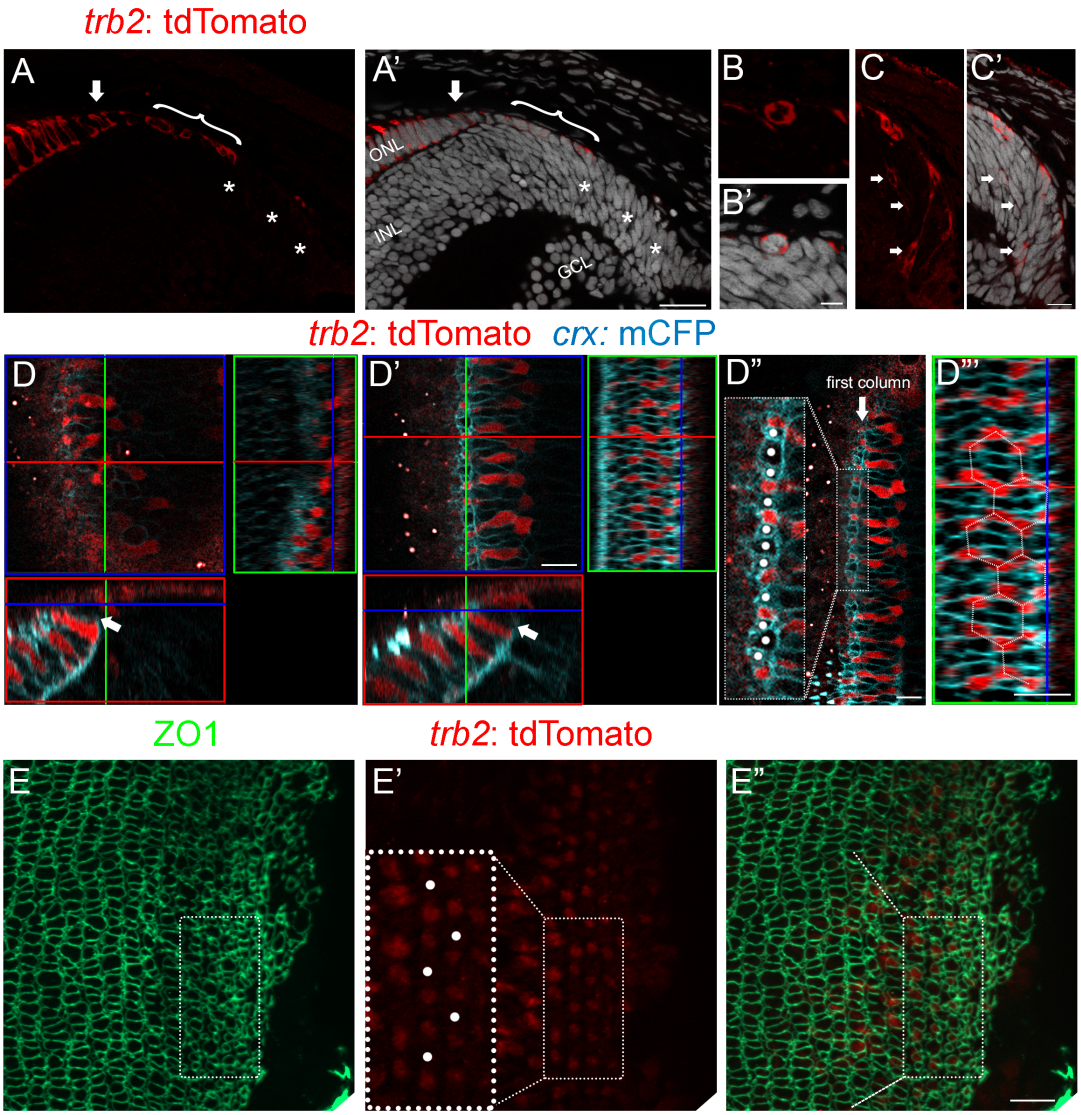

Figure 2

Figure C.2: **Spatial arrangement of cones is already patterned in the differentiating pre-column zone.** See manuscript caption page for details.

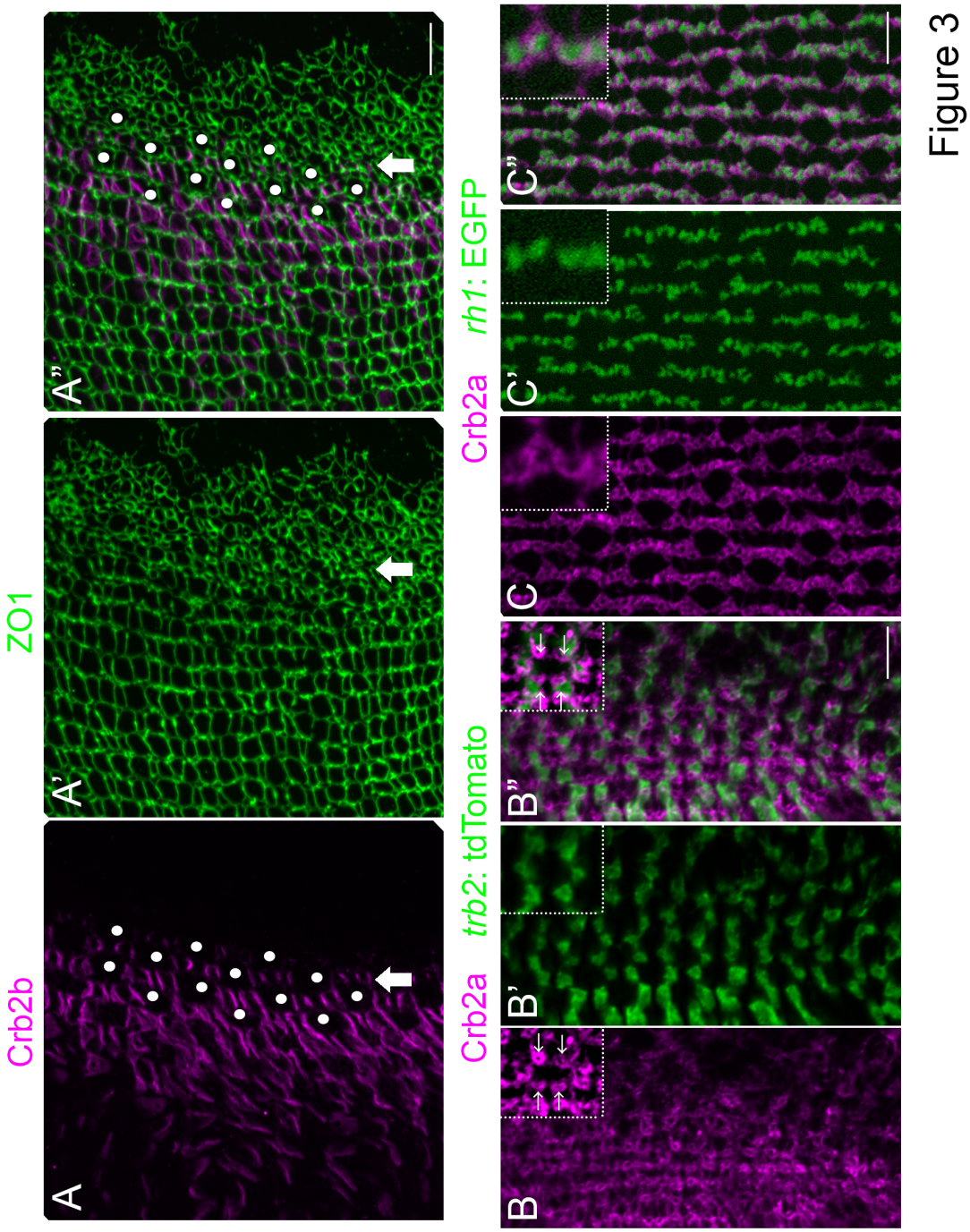

Figure C.3: **Spatial patterning of cones precedes planar polarized Crumbs localization.** See manuscript caption page for details.

A

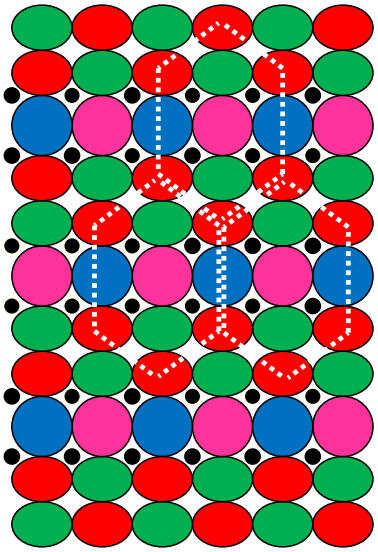

B

	trβ2+	trβ2-			
	Red	Green	Blue	UV	rod
# of cells in a hexagon	6	2	2	1	4
sharing hexagon	3	1	2	1	2
# per hexagon	2	2	1	1	4
trβ2+/- ratio	1	2			
	1	4			

C

	trβ2+	trβ2-	ratio trβ2+/trβ2-
Retina 1	72	302	4.19
Retina 2	62	344	5.55
Total	**134**	**646**	**4.87**

Figure 4

Figure C.4: **Rod photoreceptors are incorporated into the cone mosaic as it emerges from the proliferating zone.** See manuscript caption page for details.

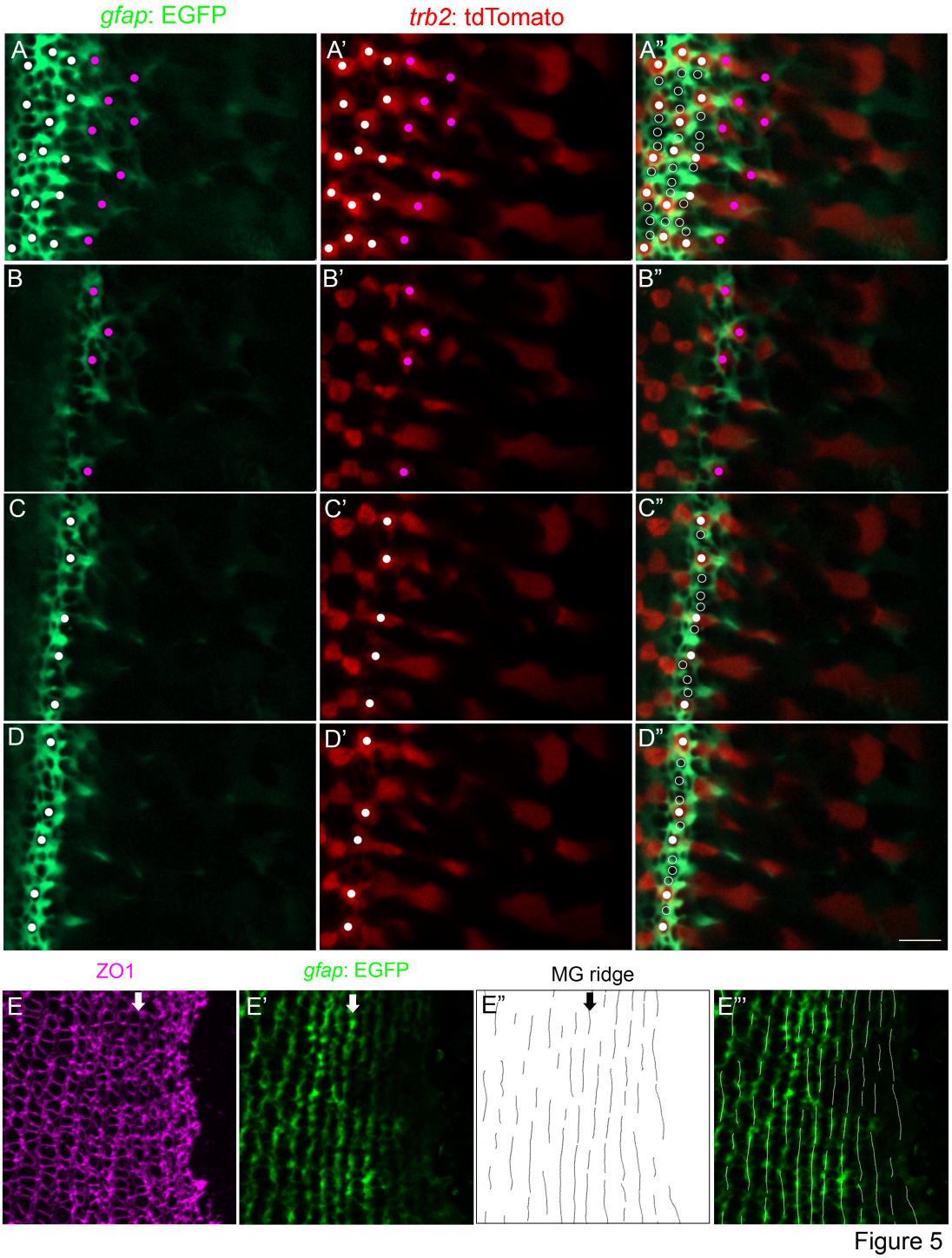

Figure C.5: **Parallel bands of Müller glial scaffolding appear simultaneously with differentiating cones.** See manuscript caption page for details.

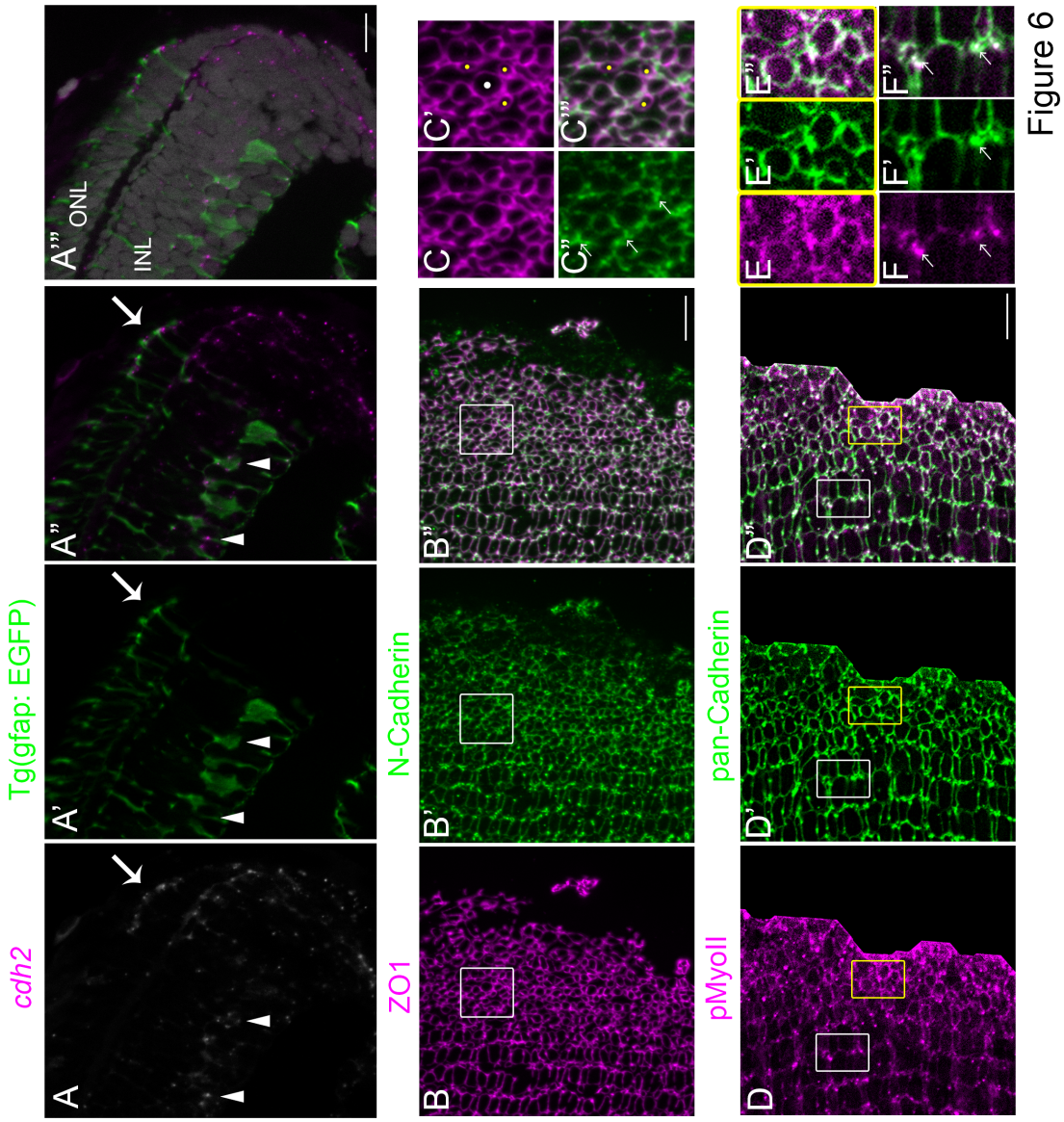

Figure C.6: **N-cadherin is associated with actomyosin mechanical forces in differentiating cones in the pre-column zone and with Müller glia inter-column bands in the mature mosaic.** See manuscript caption page for details.

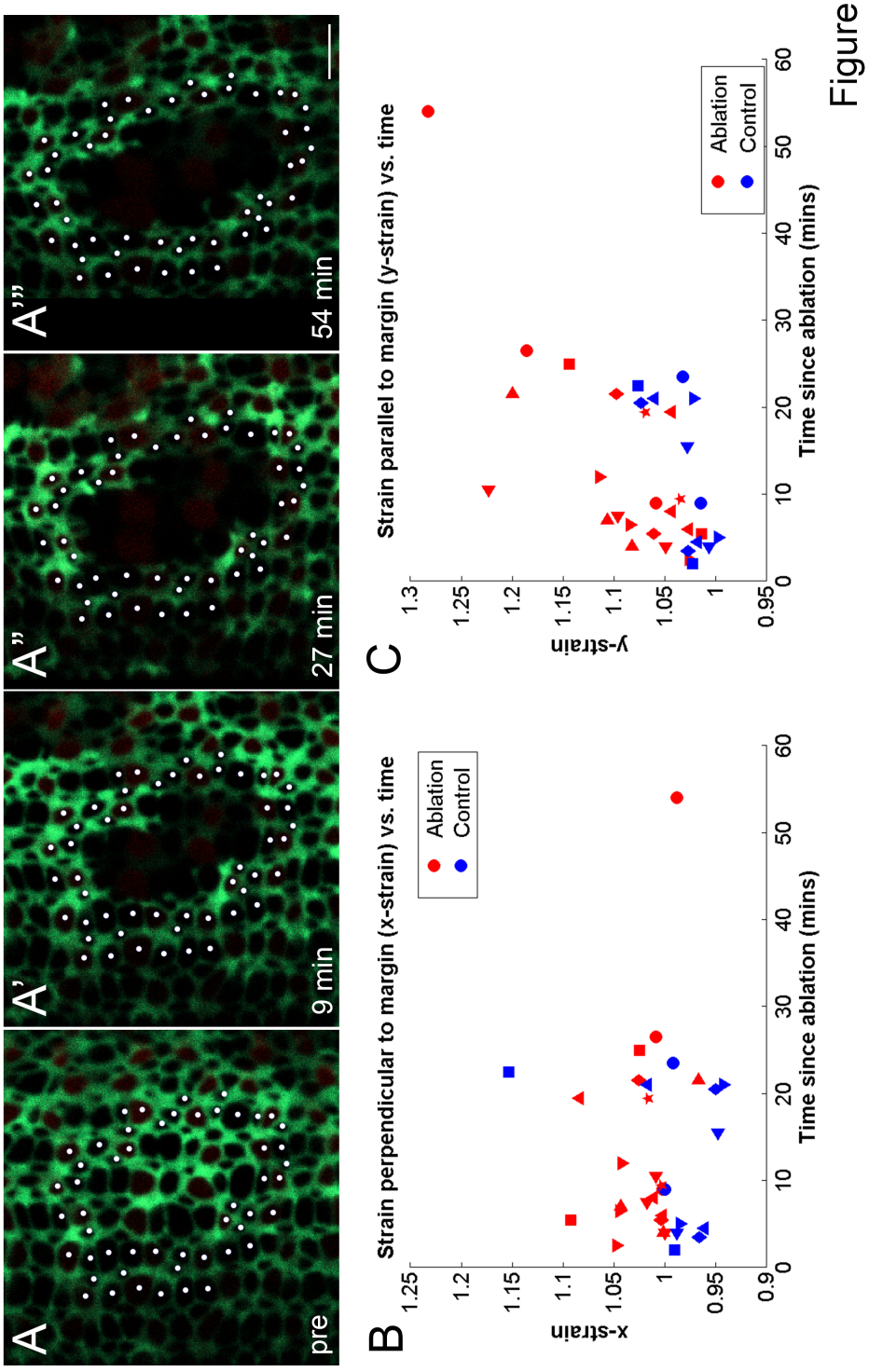

Figure C.7: **Müller glia mediate anisotropic mechanical forces in the retinal epithelium.** See manuscript caption page for details.

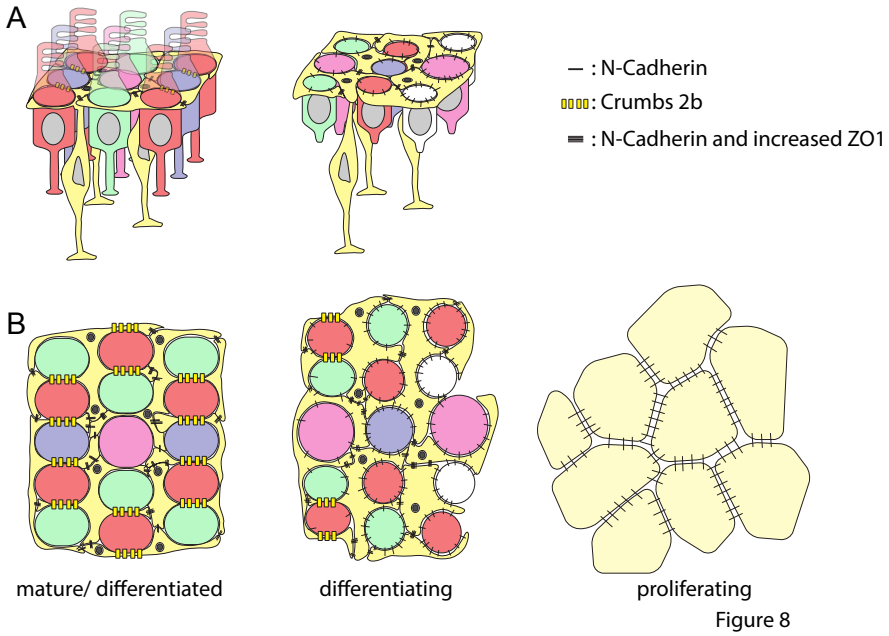

Figure C.8: **A model for how the multiplex photoreceptor mosaic is patterned by anisotropic tension, glial scaffolding, and planar polarized cell adhesion.** See manuscript caption page for details.

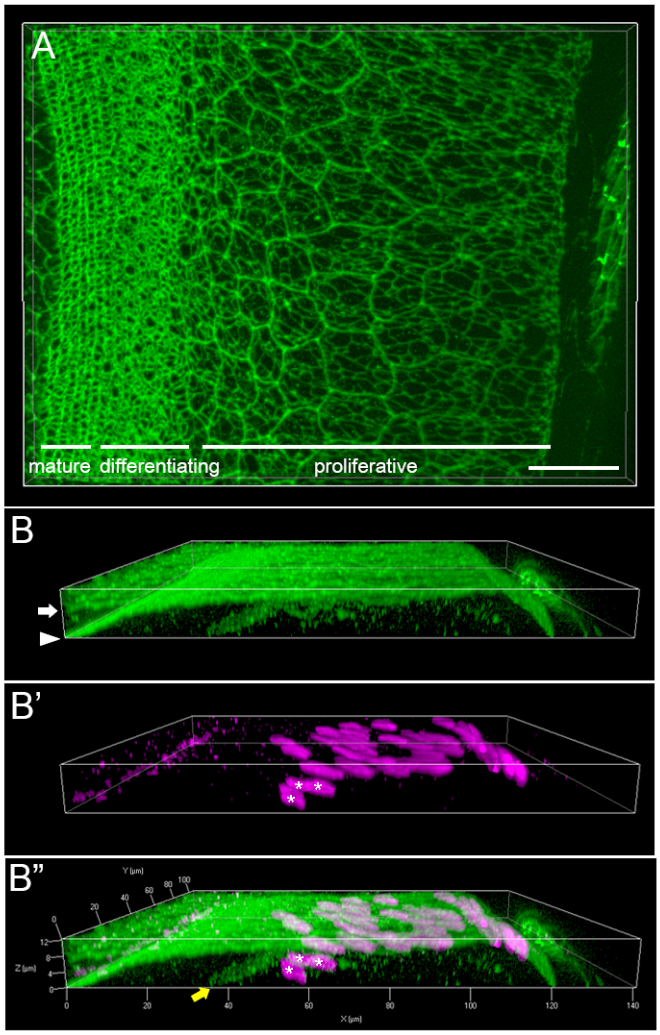

Figure C.9: **Figure 1 supplemental figure.** See manuscript caption page for details.

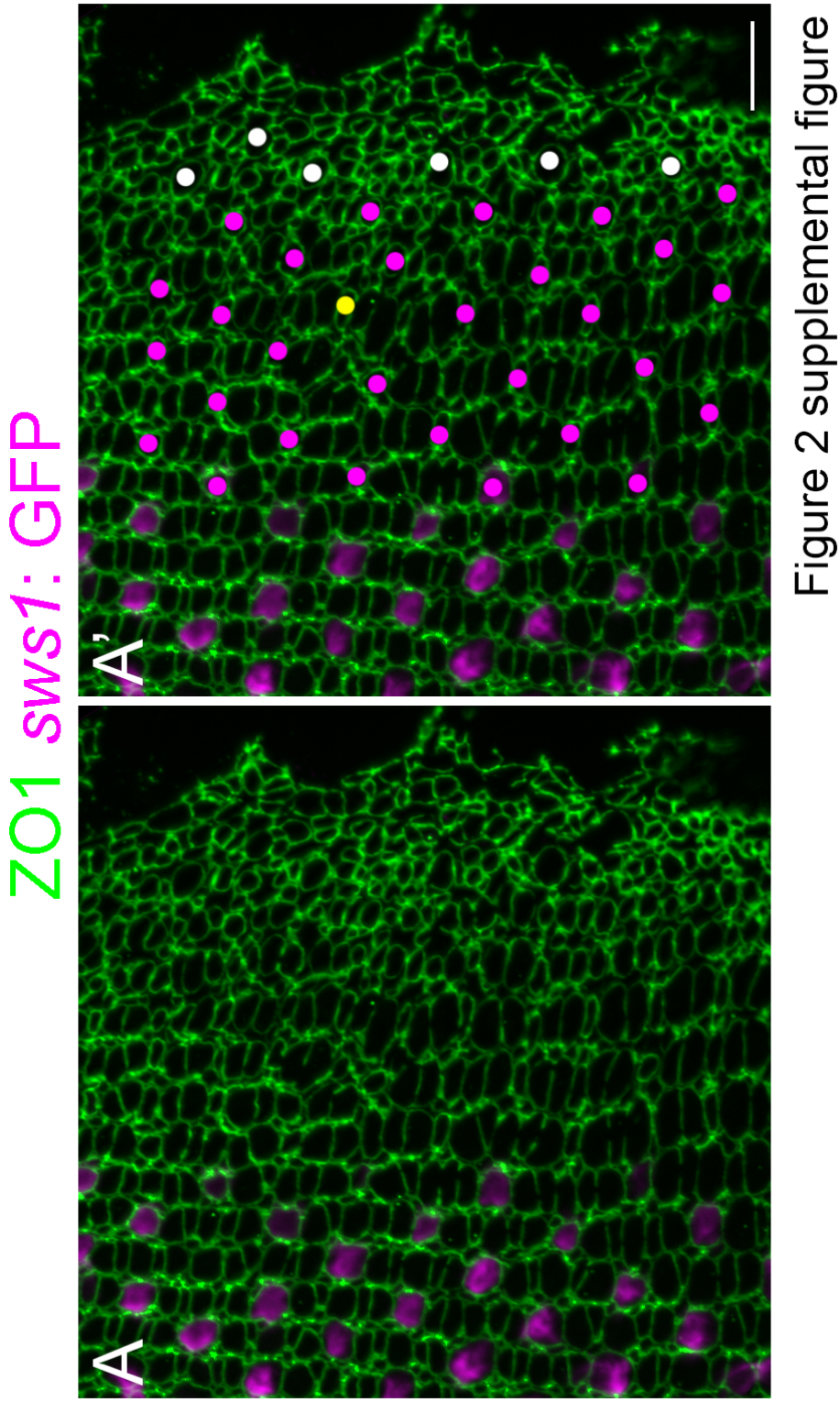

Figure C.10: **Figure 2 supplemental figure.** See manuscript caption page for details.

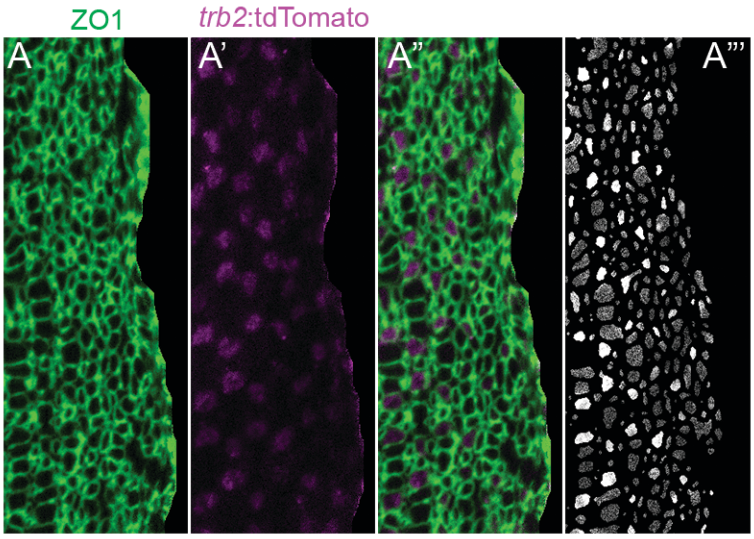

Figure C.11: **Figure 4 supplemental figure 1.** See manuscript caption page for details.

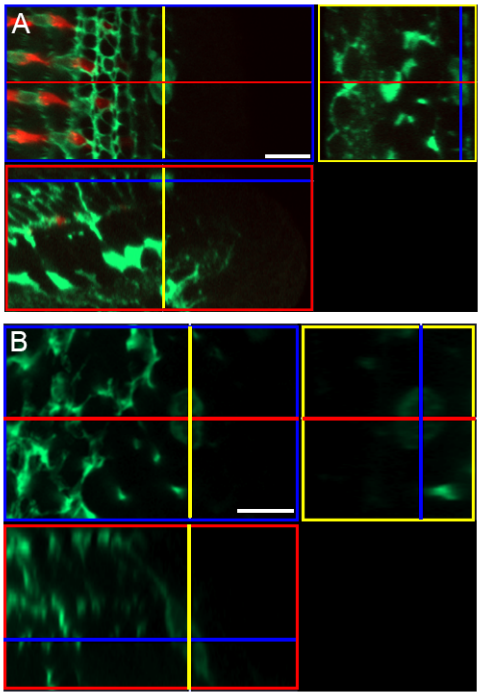

Figure 4 supplemental figure 2

Figure C.12: **Figure 4 supplemental figure 2.** See manuscript caption page for details.

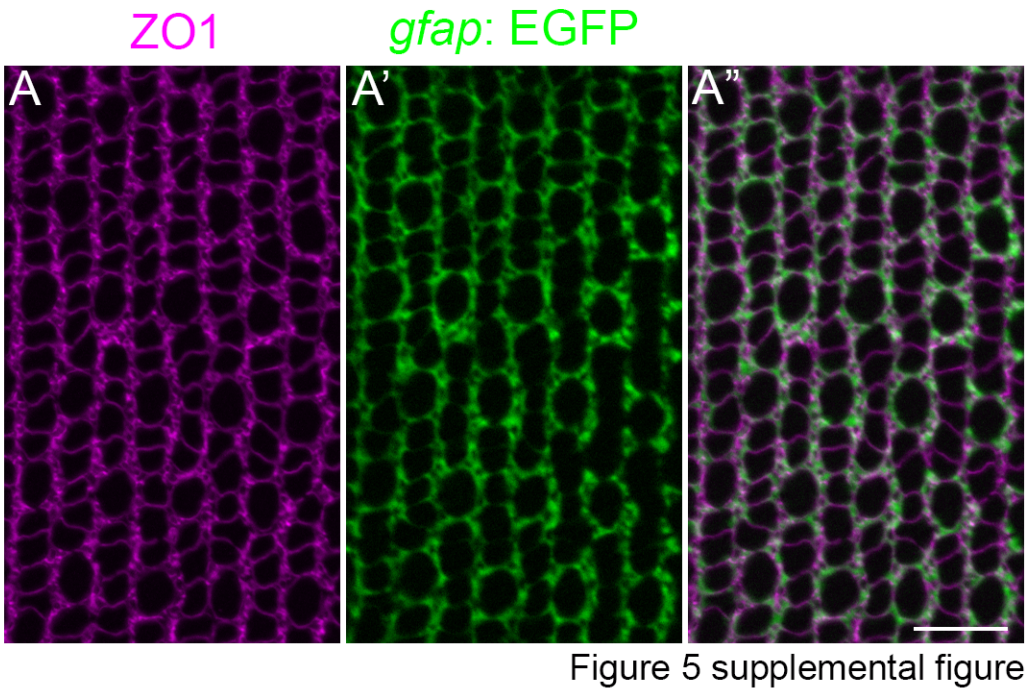

Figure C.13: **Figure 5 supplemental figure.** See manuscript caption page for details.

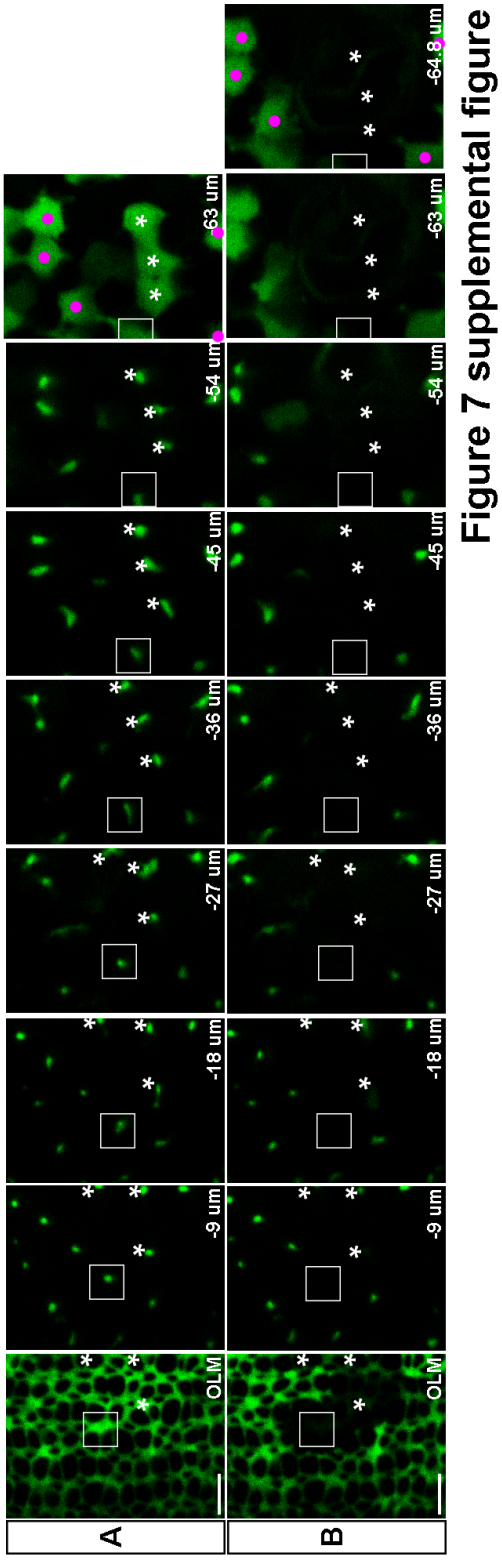

Figure C.14: **Figure 7 supplemental figure.** See manuscript caption page for details.

BIBLIOGRAPHY

[1] Lance A Davidson. Taming the tiger of tissue aggregation: how epithelia control structural assembly of underlying cells. *Developmental cell*, 14(2):152–154, 2008.

[2] Rodrigo Fernandez-Gonzalez, Sérgio de Matos Simoes, Jens-Christian Röper, Suzanne Eaton, and Jennifer A Zallen. Myosin ii dynamics are regulated by tension in intercalating cells. *Developmental cell*, 17(5):736–743, 2009.

[3] Thomas Lecuit and Pierre-Francois Lenne. Cell surface mechanics and the control of cell shape, tissue patterns and morphogenesis. *Nature Reviews Molecular Cell Biology*, 8(8):633–644, 2007.

[4] Thomas Lecuit, Pierre-François Lenne, and Edwin Munro. Force generation, transmission, and integration during cell and tissue morphogenesis. *Annual review of cell and developmental biology*, 27:157–184, 2011.

[5] Adam C. Martin and Eric F Wieschaus. Tensions divide. *Nature Cell Biology*, 12:5–7.

[6] Matthieu Cavey and Thomas Lecuit. Molecular bases of cell–cell junctions stability and dynamics. *Cold Spring Harbor perspectives in biology*, 1(5):a002998, 2009.

[7] P Friedl and JA Zallen. Dynamics of cell-cell and cell-matrix interactions in morphogenesis, regeneration and cancer. *Current opinion in cell biology*, 22(5):557, 2010.

[8] Jennifer M Halbleib and W James Nelson. Cadherins in development: cell adhesion, sorting, and tissue morphogenesis. *Genes & development*, 20(23):3199–3214, 2006.

[9] Ulrich Tepass and Kathryn P Harris. Adherens junctions in drosophila retinal morphogenesis. *Trends in cell biology*, 17(1):26–35, 2007.

[10] Vania MM Braga. Cell–cell adhesion and signalling. *Current opinion in cell biology*, 14(5):546–556, 2002.

[11] Xuejun Chen and Barry M Gumbiner. Crosstalk between different adhesion molecules. *Current opinion in cell biology*, 18(5):572–578, 2006.

[12] Reza Farhadifar, Jens-Christian Röper, Benoit Aigouy, Suzanne Eaton, and Frank Jülicher. The influence of cell mechanics, cell-cell interactions, and proliferation on epithelial packing. *Current Biology*, 17(24):2095–2104, 2007.

[13] Sascha Hilgenfeldt, Sinem Erisken, and Richard W Carthew. Physical modeling of cell geometric order in an epithelial tissue. *Proceedings of the National Academy of Sciences*, 105(3):907–911, 2008.

[14] Lars Hufnagel, Aurelio A Teleman, Hervé Rouault, Stephen M Cohen, and Boris I Shraiman. On the mechanism of wing size determination in fly development. *Proceedings of the National Academy of Sciences*, 104(10):3835–3840, 2007.

[15] Jos Käfer, Takashi Hayashi, Athanasius FM Marée, Richard W Carthew, and François Graner. Cell adhesion and cortex contractility determine cell patterning in the drosophilaretina. *Proceedings of the National Academy of Sciences*, 104(47):18549–18554, 2007.

[16] Katharina P Landsberg, Reza Farhadifar, Jonas Ranft, Daiki Umetsu, Thomas J Widmann, Thomas Bittig, Amani Said, Frank Jülicher, and Christian Dahmann. Increased cell bond tension governs cell sorting at the drosophila anteroposterior compartment boundary. *Current Biology*, 19(22):1950–1955, 2009.

[17] Sabine Schilling, Maria Willecke, Tinri Aegerter-Wilmsen, Olaf A Cirpka, Konrad Basler, and Christian von Mering. Cell-sorting at the a/p boundary in the drosophila wing primordium: a computational model to consolidate observed non-local effects of hh signaling. *PLoS Comput Biol*, 7(4):e1002025, 2011.

[18] Charlène Guillot and Thomas Lecuit. Mechanics of epithelial tissue homeostasis and morphogenesis. *Science*, 340(6137):1185–1189, 2013.

[19] Jean-Léon Maître and Carl-Philipp Heisenberg. Three functions of cadherins in cell adhesion. *Current Biology*, 23(14):R626–R633, 2013.

[20] Adam C Martin, Matthias Kaschube, and Eric F Wieschaus. Pulsed contractions of an actin–myosin network drive apical constriction. *Nature*, 457(7228):495–499, 2009.

[21] Matteo Rauzi, Pierre-François Lenne, and Thomas Lecuit. Planar polarized actomyosin contractile flows control epithelial junction remodelling. *Nature*, 468(7327):1110–1114, 2010.

[22] Xiaoyan Ma, Holley E Lynch, Peter C Scully, and M Shane Hutson. Probing embryonic tissue mechanics with laser hole drilling. *Physical biology*, 6(3):036004, 2009.

[23] Jerome Solon, Aynur Kaya-Copur, Julien Colombelli, and Damian Brunner. Pulsed forces timed by a ratchet-like mechanism drive directed tissue movement during dorsal closure. *Cell*, 137(7):1331–1342, 2009.

[24] Adam C Martin, Michael Gelbart, Rodrigo Fernandez-Gonzalez, Matthias Kaschube, and Eric F Wieschaus. Integration of contractile forces during tissue invagination. *The Journal of cell biology*, pages jcb–200910099, 2010.

[25] Benoît Aigouy, Reza Farhadifar, Douglas B Staple, Andreas Sagner, Jens-Christian Röper, Frank Jülicher, and Suzanne Eaton. Cell flow reorients the axis of planar polarity in the wing epithelium of drosophila. *Cell*, 142(5):773–786, 2010.

[26] Robert P Simone and Stephen DiNardo. Actomyosin contractility and discs large contribute to junctional conversion in guiding cell alignment within the drosophila embryonic epithelium. *Development*, 137(8):1385–1394, 2010.

[27] Georgios Trichas, Aaron M Smith, Natalia White, Vivienne Wilkins, Tomoko Watanabe, Abigail Moore, Bradley Joyce, Jacintha Sugnaseelan, Tristan A Rodriguez, David Kay, et al. Multi-cellular rosettes in the mouse visceral endoderm facilitate the ordered migration of anterior visceral endoderm cells. *PLoS Biol*, 10(2):e1001256, 2012.

[28] Takashi Hayashi and Richard W Carthew. Surface mechanics mediate pattern formation in the developing retina. *Nature*, 431(7009):647–652, 2004.

[29] Christian Dahmann, Andrew C Oates, and Michael Brand. Boundary formation and maintenance in tissue development. *Nature Reviews Genetics*, 12(1):43–55, 2011.

[30] Christian Dahmann and Konrad Basler. Compartment boundaries: at the edge of development. *Trends in Genetics*, 15(8):320–326, 1999.

[31] Barry M Gumbiner. Regulation of cadherin-mediated adhesion in morphogenesis. *Nature reviews Molecular cell biology*, 6(8):622–634, 2005.

[32] Ulrich Tepass, Dorothea Godt, and Rudolf Winklbauer. Cell sorting in animal development: signalling and adhesive mechanisms in the formation of tissue boundaries. *Current opinion in genetics & development*, 12(5):572–582, 2002.

[33] M Shane Hutson, Yoichiro Tokutake, Ming-Shien Chang, James W Bloor, Stephanos Venakides, Daniel P Kiehart, and Glenn S Edwards. Forces for morphogenesis investigated with laser microsurgery and quantitative modeling. *Science*, 300(5616):145–149, 2003.

[34] Yusuke Toyama, Xomalin G Peralta, Adrienne R Wells, Daniel P Kiehart, and Glenn S Edwards. Apoptotic force and tissue dynamics during drosophila embryogenesis. *Science*, 321(5896):1683–1686, 2008.

[35] Ryan S Gray, Isabelle Roszko, and Lilianna Solnica-Krezel. Planar cell polarity: coordinating morphogenetic cell behaviors with embryonic polarity. *Developmental cell*, 21(1):120–133, 2011.

[36] Matias Simons and Marek Mlodzik. Planar cell polarity signaling: from fly development to human disease. *Annual review of genetics*, 42:517–540, 2008.

[37] Lisa V Goodrich and David Strutt. Principles of planar polarity in animal development. *Development*, 138(10):1877–1892, 2011.

[38] Guillaume Salbreux, Linda K Barthel, Pamela A Raymond, and David K Lubensky. Coupling mechanical deformations and planar cell polarity to create regular patterns in the zebrafish retina. *PLoS Comput Biol*, 8(8):e1002618, 2012.

[39] Claire Bertet, Lawrence Sulak, and Thomas Lecuit. Myosin-dependent junction remodelling controls planar cell intercalation and axis elongation. *Nature*, 429(6992):667–671, 2004.

[40] Jianbo Wang, Natasha S Hamblet, Sharayne Mark, Mary E Dickinson, Brendan C Brinkman, Neil Segil, Scott E Fraser, Ping Chen, John B Wallingford, and Anthony Wynshaw-Boris. Dishevelled genes mediate a conserved mammalian pcp pathway to regulate convergent extension during neurulation. *Development*, 133(9):1767–1778, 2006.

[41] John B Wallingford, Scott E Fraser, and Richard M Harland. Convergent extension: the molecular control of polarized cell movement during embryonic development. *Developmental cell*, 2(6):695–706, 2002.

[42] Patricia Ybot-Gonzalez, Dawn Savery, Dianne Gerrelli, Massimo Signore, Claire E Mitchell, Clare H Faux, Nicholas DE Greene, and Andrew J Copp. Convergent extension, planar-cell-polarity signalling and initiation of mouse neural tube closure. *Development*, 134(4):789–799, 2007.

[43] John B Wallingford and Richard M Harland. Neural tube closure requires dishevelled-dependent convergent extension of the midline. *Development*, 129(24):5815–5825, 2002.

[44] Rachel S Darken, Adriane M Scola, Andrew S Rakeman, Gishnu Das, Marek Mlodzik, and Paul A Wilson. The planar polarity gene strabismus regulates convergent extension movements in xenopus. *The EMBO Journal*, 21(5):976–985, 2002.

[45] Jianbo Wang, Sharayne Mark, Xiaohui Zhang, Dong Qian, Seung-Jong Yoo, Kristen Radde-Gallwitz, Yanping Zhang, Xi Lin, Andres Collazo, Anthony Wynshaw-Boris, et al. Regulation of polarized extension and planar cell polarity in the cochlea by the vertebrate pcp pathway. *Nature genetics*, 37(9):980–985, 2005.

[46] Yanshu Wang and Jeremy Nathans. Tissue/planar cell polarity in vertebrates: new insights and new questions. *Development*, 134(4):647–658, 2007.

[47] Anne-Kathrin Classen, Kurt I Anderson, Eric Marois, and Suzanne Eaton. Hexagonal packing of drosophila wing epithelial cells by the planar cell polarity pathway. *Developmental cell*, 9(6):805–817, 2005.

[48] Matteo Rauzi, Pascale Verant, Thomas Lecuit, and Pierre-Francois Lenne. Nature and anisotropy of cortical forces orienting drosophila tissue morphogenesis. *Nature cell biology*, 10(12):1401–1410, 2008.

[49] Pablo Oteiza, Mathias Köppen, Michael Krieg, Eduardo Pulgar, Cecilia Farias, Cristina Melo, Stephan Preibisch, Daniel Müller, Masazumi Tada, Steffen Hartel, et al. Planar cell polarity signalling regulates cell adhesion properties in progenitors of the zebrafish laterality organ. *Development*, 137(20):3459–3468, 2010.

[50] Athea Vichas and Jennifer A Zallen. Translating cell polarity into tissue elongation. In *Seminars in cell & developmental biology*, volume 22, pages 858–864. Elsevier, 2011.

[51] S Fürthauer, M Strempel, SW Grill, and F Jülicher. Active chiral processes in thin films. *Physical review letters*, 110(4):048103, 2013.

[52] Sundar Ram Naganathan, Sebastian Fürthauer, Masatoshi Nishikawa, Frank Jülicher, and Stephan W Grill. Active torque generation by the actomyosin cell cortex drives left–right symmetry breaking. *Elife*, 3:e04165, 2014.

[53] Sundar Ram Naganathan, Teije C Middelkoop, Sebastian Fürthauer, and Stephan W Grill. Actomyosin-driven left-right asymmetry: from molecular torques to chiral self organization. *Current opinion in cell biology*, 38:24–30, 2016.

[54] Ting-Hsuan Chen, Jeffrey J Hsu, Xin Zhao, Chunyan Guo, Margaret Wong, Yi Huang, Zongwei Li, Alan Garfinkel, Chih-Ming Ho, Yin Tintut, et al. Left-right symmetry breaking in tissue morphogenesis via cytoskeletal mechanics. *Circulation Research*, 110(4):551, 2012.

[55] Michael Levin, Amar JS Klar, and Ann F Ramsdell. Introduction to provocative questions in left–right asymmetry. *Philosophical Transactions of the Royal Society B: Biological Sciences*, 371(1710), 2016.

[56] Yee Han Tee, Tom Shemesh, Visalatchi Thiagarajan, Rizal Fajar Hariadi, Karen L Anderson, Christopher Page, Niels Volkmann, Dorit Hanein, Sivaraj Sivaramakrishnan, Michael M Kozlov, et al. Cellular chirality arising from the self-organization of the actin cytoskeleton. *Nature cell biology*, 17(4):445–457, 2015.

[57] Katsuhiko Sato, Tetsuya Hiraiwa, Emi Maekawa, Ayako Isomura, Tatsuo Shibata, and Erina Kuranaga. Left-right asymmetric cell intercalation drives directional collective cell movement in epithelial morphogenesis. *Nature communications*, 6, 2015.

[58] Nicanor González-Morales, Charles Géminard, Gaëlle Lebreton, Delphine Cerezo, Jean-Baptiste Coutelis, and Stéphane Noselli. The atypical cadherin dachsous controls left-right asymmetry in drosophila. *Developmental cell*, 33(6):675–689, 2015.

[59] Kiichiro Taniguchi, Reo Maeda, Tadashi Ando, Takashi Okumura, Naotaka Nakazawa, Ryo Hatori, Mitsutoshi Nakamura, Shunya Hozumi, Hiroo Fujiwara, and Kenji Matsuno. Chirality in planar cell shape contributes to left-right asymmetric epithelial morphogenesis. *Science*, 333(6040):339–341, 2011.

[60] Ryo Hatori, Tadashi Ando, Takeshi Sasamura, Naotaka Nakazawa, Mitsutoshi Nakamura, Kiichiro Taniguchi, Shunya Hozumi, Junichi Kikuta, Masaru Ishii, and Kenji Matsuno. Left–right asymmetry is formed in individual cells by intrinsic cell chirality. *Mechanisms of development*, 133:146–162, 2014.

[61] Katsuhiko Sato, Tetsuya Hiraiwa, and Tatsuo Shibata. Cell chirality induces collective cell migration in epithelial sheets. *Physical review letters*, 115(18):188102, 2015.

[62] Mikiko Inaki, Jingyang Liu, and Kenji Matsuno. Cell chirality: its origin and roles in left–right asymmetric development. *Phil. Trans. R. Soc. B*, 371(1710):20150403, 2016.

[63] Bin Zhang and Peter G Wolynes. Shape transitions and chiral symmetry breaking in the energy landscape of the mitotic chromosome. *Physical Review Letters*, 116(24):248101, 2016.

[64] Pauline Spéder, Astrid Petzoldt, Magali Suzanne, and Stéphane Noselli. Strategies to establish left/right asymmetry in vertebrates and invertebrates. *Current opinion in genetics & development*, 17(4):351–358, 2007.

[65] Michael Levin. Left–right asymmetry in embryonic development: a comprehensive review. *Mechanisms of development*, 122(1):3–25, 2005.

[66] Christopher L Henley. Possible origins of macroscopic left-right asymmetry in organisms. *Journal of statistical physics*, 148(4):741–775, 2012.

[67] Charles Géminard, Nicanor González-Morales, Jean-Baptiste Coutelis, and Stéphane Noselli. The myosin id pathway and left–right asymmetry in drosophila. *genesis*, 52(6):471–480, 2014.

[68] Peter S Hegan, Eric Ostertag, Aron M Geurts, and Mark S Mooseker. Myosin id is required for planar cell polarity in ciliated tracheal and ependymal epithelial cells. *Cytoskeleton*, 72(10):503–516, 2015.

[69] Takashi Okumura, Takeshi Sasamura, Momoko Inatomi, Shunya Hozumi, Mitsutoshi Nakamura, Ryo Hatori, Kiichiro Taniguchi, Naotaka Nakazawa, Emiko Suzuki, Reo Maeda, et al. Class i myosins have overlapping and specialized functions in left-right asymmetric development in drosophila. *Genetics*, 199(4):1183–1199, 2015.

[70] Jonathan V Selinger and David R Nelson. Theory of hexatic-to-hexatic transitions. *Physical review letters*, 61(4):416, 1988.

[71] Jonathan V Selinger and David R Nelson. Theory of transitions among tilted hexatic phases in liquid crystals. *Physical Review A*, 39(6):3135, 1989.

[72] Guillaume Salbreux, Linda K Barthel, Pamela A Raymond, and David K Lubensky. Coupling mechanical deformations and planar cell polarity to create regular patterns in the zebrafish retina. *PLoS Comput Biol*, 8(8):e1002618, 2012.

[73] Pamela A Raymond, Steven M Colvin, Zahera Jabeen, Mikiko Nagashima, Linda K Barthel, Jeremy Hadidjojo, Lilia Popova, Vivek R Pejaver, and David K Lubensky. Patterning the cone mosaic array in zebrafish retina requires specification of ultraviolet-sensitive cones. *PloS one*, 9(1):e85325, 2014.

[74] Martin Golubitsky, Ian Stewart, et al. *Singularities and groups in bifurcation theory*, volume 2. Springer Science & Business Media, 1984.

[75] Pauline Spéder, Géza Ádám, and Stéphane Noselli. Type id unconventional myosin controls left–right asymmetry in drosophila. *Nature*, 440(7085):803–807, 2006.

[76] Robert P Simone and Stephen DiNardo. Actomyosin contractility and discs large contribute to junctional conversion in guiding cell alignment within the drosophila embryonic epithelium. *Development*, 137(8):1385–1394, 2010.

[77] Fa-Yueh Wu. The potts model. *Reviews of modern physics*, 54(1):235, 1982.

[78] MC Marchetti, JF Joanny, S Ramaswamy, TB Liverpool, J Prost, Madan Rao, and R Aditi Simha. Hydrodynamics of soft active matter. *Reviews of Modern Physics*, 85(3):1143, 2013.

[79] Jonathan V Selinger, Zhen-Gang Wang, Robijn F Bruinsma, and Charles M Knobler. Chiral symmetry breaking in langmuir monolayers and smectic films. *Physical review letters*, 70(8):1139, 1993.

[80] Pamela A. Raymond, Steven M. Colvin, Zahera Jabeen, Mikiko Nagashima, Linda K. Barthel, Jeremy Hadidjojo, Lilia Popova, Vivek R. Pejaver, and David K. Lubensky. Patterning the cone mosaic array in zebrafish retina requires specification of ultraviolet-sensitive cones. *PLOS ONE*, 9(1):1–17, 01 2014.

[81] Mikiko Nagashima, Jeremy Hadidjojo, Linda K. Barthel, David K. Lubensky, and Pamela A. Raymond. Anisotropic glial scaffolding shapes a multiplex photoreceptor mosaic in zebrafish retina. *submitted to Nature Communications, manuscript attached in Appendix B*, 2017.

[82] Zac Pujic and Jarema Malicki. Retinal pattern and the genetic basis of its formation in zebrafish. In *Seminars in cell & developmental biology*, volume 15, pages 105–114. Elsevier, 2004.

[83] Kjell Engström. Cone types and cone arrangements in teleost retinae. *Acta Zoologica*, 44(1-2):179–243, 1963.

[84] AH Lyall. Cone arrangements in teleost retinae. *Journal of Cell Science*, 3(42):189–201, 1957.

[85] W Ted Allison, Linda K Barthel, Kristina M Skebo, Masaki Takechi, Shoji Kawamura, and Pamela A Raymond. Ontogeny of cone photoreceptor mosaics in zebrafish. *Journal of Comparative Neurology*, 518(20):4182–4195, 2010.

[86] Karen D Larison and Ruth Bremiller. Early onset of phenotype and cell patterning in the embryonic zebrafish retina. *Development*, 109(3):567–576, 1990.

[87] Pamela A Raymond and Linda K Barthel. A moving wave patterns the cone photoreceptor mosaic array in the zebrafish retina. *International Journal of Developmental Biology*, 48(8-9):935–945, 2004.

[88] MJ Ochocinska and PF Hitchcock. Neurod regulates proliferation of photoreceptor progenitors in the retina of the zebrafish. *Mechanisms of development*, 126(3):128–141, 2009.

[89] Pamela A Raymond, Linda K Barthel, Rebecca L Bernardos, and John J Perkowski. Molecular characterization of retinal stem cells and their niches in adult zebrafish. *BMC developmental biology*, 6(1):36, 2006.

[90] PA Raymond and SS Easter. Postembryonic growth of the optic tectum in goldfish. i. location of germinal cells and numbers of neurons produced. *Journal of Neuroscience*, 3(5):1077–1091, 1983.

[91] Deborah L Stenkamp and David A Cameron. Cellular pattern formation in the retina: retinal regeneration as a model system. *Molecular vision*, 8:280–293, 2002.

[92] Akito Chinen, Takanori Hamaoka, Yukihiro Yamada, and Shoji Kawamura. Gene duplication and spectral diversification of cone visual pigments of zebrafish. *Genetics*, 163(2):663–675, 2003.

[93] Leon Nawrocki, Ruth Bremiller, Georg Streisinger, and Michael Kaplan. Larval and adult visual pigments of the zebrafish, brachydanio rerio. *Vision research*, 25(11):1569–1576, 1985.

[94] Deborah L Stenkamp. Neurogenesis in the fish retina. *International review of cytology*, 259:173–224, 2007.

[95] Pamela A Raymond. Cytodifferentiation of photoreceptors in larval goldfish: delayed maturation of rods. *Journal of Comparative Neurology*, 236(1):90–105, 1985.

[96] David S Williams, Kentaro Arikawa, and Taru Paallysaho. Cytoskeletal components of the adherens junctions between the photoreceptors and the supportive müller cells. *Journal of Comparative Neurology*, 295(1):155–164, 1990.

[97] Ilse Gosens, Anneke I den Hollander, Frans PM Cremers, and Ronald Roepman. Composition and function of the crumbs protein complex in the mammalian retina. *Experimental eye research*, 86(5):713–726, 2008.

[98] Karen Alvarez-Delfin, Ann C Morris, Corey D Snelson, Joshua T Gamse, Tripti Gupta, Florence L Marlow, Mary C Mullins, Harold A Burgess, Michael Granato, and James M Fadool. Tbx2b is required for ultraviolet photoreceptor cell specification during zebrafish retinal development. *Proceedings of the National Academy of Sciences*, 106(6):2023–2028, 2009.

[99] Rafael C Eddins Gonzalez, Steven L Woods, Richard E Richard Eugene Rafael C Gonzalez, Richard E Woods, and Steven L Eddins. *Digital image processing using MATLAB*. Number 04; TA1637, G6. 2004.

[100] Jerome Friedman, Trevor Hastie, and Robert Tibshirani. *The elements of statistical learning*, volume 1. Springer series in statistics Springer, Berlin, 2001.

[101] Jae S Lim. Two-dimensional signal and image processing. *Englewood Cliffs, NJ, Prentice Hall, 1990, 710 p.*, 1990.

[102] Pierre Soille. *Morphological image analysis: principles and applications*. Springer Science & Business Media, 2013.

[103] Karel Zuiderveld. Contrast limited adaptive histogram equalization. *Graphics gems*, pages 474–485, 1994.

[104] Mathews Jacob and Michael Unser. Design of steerable filters for feature detection using canny-like criteria. *IEEE transactions on pattern analysis and machine intelligence*, 26(8):1007–1019, 2004.

[105] Julia Shand, Michael A Archer, and Shaun P Collin. Ontogenetic changes in the retinal photoreceptor mosaic in a fish, the black bream, acanthopagrus butcheri. *The Journal of comparative neurology*, 412(2):203–217, 1999.

[106] Sachihiro C Suzuki, Adam Bleckert, Philip R Williams, Masaki Takechi, Shoji Kawamura, and Rachel OL Wong. Cone photoreceptor types in zebrafish are generated by symmetric terminal divisions of dedicated precursors. *Proceedings of the National Academy of Sciences*, 110(37):15109–15114, 2013.

[107] Bernard L Welch. The generalization ofstudent's' problem when several different population variances are involved. *Biometrika*, 34(1/2):28–35, 1947.

[108] William H Press, Brian P Flannery, Saul A Teukolsky, William T Vetterling, and Peter B Kramer. Numerical recipes: the art of scientific computing, 1987.

[109] Harold Hotelling. The generalization of student's ratio. In *Breakthroughs in Statistics*, pages 54–65. Springer, 1992.

[110] Sandro Cavicchi, Gianfranco Giorgi, Vanna Natali, and Daniela Guerra. Temperature-related divergence in experimental populations of drosophila melanogaster. iii. fourier and centroid analysis of wing shape and relationship between shape variation and fitness. *Journal of Evolutionary Biology*, 4(1):141–159, 1991.

[111] Christian Peter Klingenberg, Marta Barluenga, and Axel Meyer. Shape analysis of symmetric structures: quantifying variation among individuals and asymmetry. *Evolution*, 56(10):1909–1920, 2002.

[112] Christian Peter Klingenberg and Grant S McIntyre. Geometric morphometrics of developmental instability: analyzing patterns of fluctuating asymmetry with procrustes methods. *Evolution*, pages 1363–1375, 1998.

[113] Casper J Breuker, James S Patterson, and Christian Peter Klingenberg. A single basis for developmental buffering of drosophila wing shape. *PLoS one*, 1(1):e7, 2006.

[114] Vincent Debat and Frédérique Peronnet. Asymmetric flies: the control of developmental noise in drosophila. *Fly*, 7(2):70–77, 2013.

[115] Vincent Debat, Claire C Milton, Suzannah Rutherford, Christian Peter Klingenberg, and Ary A Hoffmann. Hsp90 and the quantitative variation of wing shape in drosophila melanogaster. *Evolution*, 60(12):2529–2538, 2006.

[116] Sandro Cavicchi, Daniela Guerra, Gianfranco Giorgi, and Cristina Pezzoli. Temperature-related divergence in experimental populations of drosophila melanogaster. i. genetic and developmental basis of wing size and shape variation. *Genetics*, 109(4):665–689, 1985.

[117] Floris Bosveld, Isabelle Bonnet, Boris Guirao, Sham Tlili, Zhimin Wang, Ambre Petitalot, Raphaël Marchand, Pierre-Luc Bardet, Philippe Marcq, François Graner, et al. Mechanical control of morphogenesis by fat/dachsous/four-jointed planar cell polarity pathway. *Science*, 336(6082):724–727, 2012.

[118] Boris Guirao, Stéphane U Rigaud, Floris Bosveld, Anaïs Bailles, Jesus Lopez-Gay, Shuji Ishihara, Kaoru Sugimura, François Graner, and Yohanns Bellaïche. Unified quantitative characterization of epithelial tissue development. *Elife*, 4:e08519, 2015.

[119] I Grant. Particle image velocimetry: a review. *Proceedings of the Institution of Mechanical Engineers, Part C: Journal of Mechanical Engineering Science*, 211(1):55–76, 1997.

[120] Jerry Westerweel. Fundamentals of digital particle image velocimetry. *Measurement science and technology*, 8(12):1379, 1997.

[121] Ronald J Adrian and Jerry Westerweel. *Particle image velocimetry*. Number 30. Cambridge University Press, 2011.

[122] Markus Raffel, Christian E Willert, Steven Wereley, and Jürgen Kompenhans. *Particle image velocimetry: a practical guide*. Springer, 2013.

[123] J Kristian Sveen and Edwin A Cowen. Quantitative imaging techniques and their application to wavy flows. *Advances in Coastal and Ocean Engineering*, 9:1, 2004.

[124] Johan Kristian Sveen. An introduction to matpiv v. 1.6. 1. *Preprint series. Mechanics and Applied Mathematics*, 2004.

[125] William Thielicke and Eize Stamhuis. Pivlab–towards user-friendly, affordable and accurate digital particle image velocimetry in matlab. *Journal of Open Research Software*, 2(1):e30, 2014.

[126] W Thielicke, EJ Stamhuis, W Thielicke, and EJ Stamhuis. Pivlab–time-resolved digital particle image velocimetry tool for matlab, version: 1.32, 2014. *DOI*, 10:m9, 2014.

[127] William Thielicke. *The flapping flight of birds: Analysis and application*. PhD thesis, 2014.